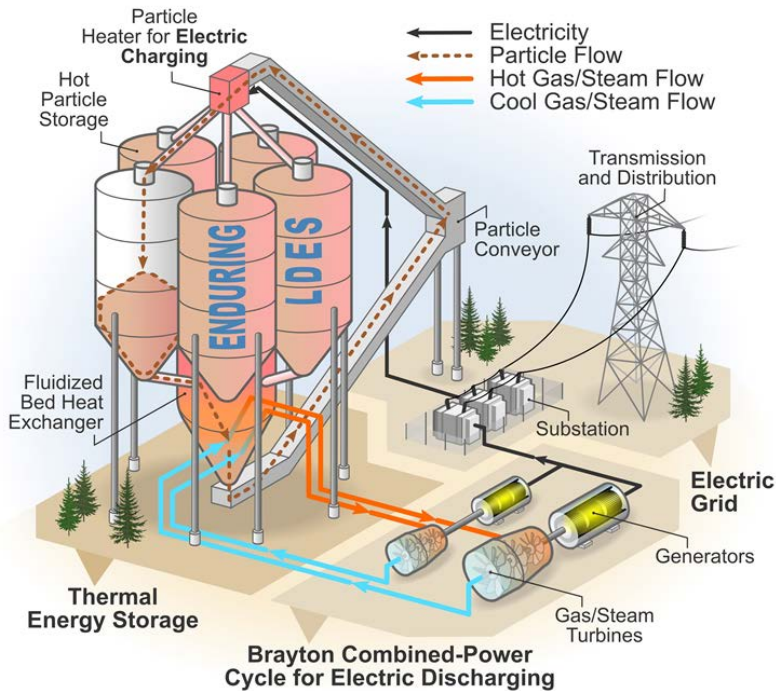




Economic Long-Duration Electricity Storage by Using Low-Cost Thermal Energy Storage and High-Efficiency Power Cycle (ENDURING)

Zhiwen Ma

National Renewable Energy Laboratory



**NREL is a national laboratory of the U.S. Department of Energy
Office of Energy Efficiency & Renewable Energy
Operated by the Alliance for Sustainable Energy, LLC**

**Technical Report
NREL/TP-5700-84728
September 2023**

This report is available at no cost from the National Renewable Energy Laboratory (NREL) at www.nrel.gov/publications.

Contract No. DE-AC36-08GO28308



Economic Long-Duration Electricity Storage by Using Low-Cost Thermal Energy Storage and High-Efficiency Power Cycle (ENDURING)

Zhiwen Ma

National Renewable Energy Laboratory

Suggested Citation

Ma, Zhiwen. 2023. *Economic Long-Duration Electricity Storage by Using Low-Cost Thermal Energy Storage and High-Efficiency Power Cycle (ENDURING)*. Golden, CO: National Renewable Energy Laboratory. NREL/TP-5700-84728.
<https://www.nrel.gov/docs/fy23osti/84728.pdf>.

**NREL is a national laboratory of the U.S. Department of Energy
Office of Energy Efficiency & Renewable Energy
Operated by the Alliance for Sustainable Energy, LLC**

This report is available at no cost from the National Renewable Energy Laboratory (NREL) at www.nrel.gov/publications.

Contract No. DE-AC36-08GO28308

Technical Report
NREL/TP-5700-84728
September 2023

National Renewable Energy Laboratory
15013 Denver West Parkway
Golden, CO 80401
303-275-3000 • www.nrel.gov

NOTICE

This work was authored in part by the National Renewable Energy Laboratory, operated by Alliance for Sustainable Energy, LLC, for the U.S. Department of Energy (DOE) under Contract No. DE-AC36-08GO28308. Funding was provided in part by the DOE Advanced Research Projects Agency–Energy (ARPA-E) Duration Addition to electricity Storage (DAYS) Program under Work Authorization Number 18/CJ000/07/05, which is gratefully acknowledged. The views expressed herein do not necessarily represent the views of the DOE or the U.S. Government.

This report is available at no cost from the National Renewable Energy Laboratory (NREL) at www.nrel.gov/publications.

U.S. Department of Energy (DOE) reports produced after 1991 and a growing number of pre-1991 documents are available free via www.OSTI.gov.

Cover Graphic by Partrick Davenport, NREL

NREL prints on paper that contains recycled content.

Preface

Award:	Project WAS#: 18/CJ000/07/05, [DE-AR0000992]
Sponsoring Agency	U.S. DOE, Advanced Research Projects Agency–Energy (ARPA-E)
Lead Recipient:	National Renewable Energy Laboratory (NREL)
Project Team Members	Colorado School of Mines (CSM) General Electric Global Research Center (GE GRC) Allied Mineral Products, Inc. Babcock & Wilcox Company Purdue University
Project Title:	Economic Long-Duration Electricity Storage by Using Low-Cost Thermal Energy Storage and High-Efficiency Power Cycle (ENDURING)
Program Director:	Dr. Halle Cheeseman
Principal Investigator:	Dr. Zhiwen Ma
Contract Administrator:	Ms. Erin Gilley
Date of Report:	12/31/2022
Reporting Period:	04/15/2019–09/30/2022

Acknowledgments

We thank ARPA-E Program Directors, Dr. Halle Cheeseman, Dr. Vivien Lecoustre, Dr. Scott Litzelman, and Mr. Max Tuttmann, for their direction and support.

Project task performers are acknowledged under relevant task or subtask headings. We thank the contributions from General Electric Global Research Center, Dr. James Tallman, Dr. Naveenan Thiagarajan, Dr. Doug Hofer, and Dr. Ching-Jen Tang for their performance analysis of air-Brayton combined cycles. Other development contributors include Mr. Patrick Davenport, Mr. Jeffrey Gifford, Dr. Korey Cook, and Dr. Janna Martinek (NREL); Prof. Aaron Morris and Dr. Jason Schirck (Purdue); Prof. Ruichong Zhang and Dr. Xingchao Wang (Colorado School of Mines); Mr. Matthew Lambert (Allied Mineral Products); and Mr. Thomas Flynn and Mr. Timothy A. Fuller (Babcock & Wilcox). We appreciate the involvement of Mr. Ryan Bowers (Worley-Advisian) in the project. The authors thank the following colleagues from the NREL Communications Office: Susannah Shoemaker, Deanna Cook, Patrick Hayes, and Star Brunton. We also thank Mark Mehos of NREL for advising the project development and reviewing this report.

List of Acronyms

ABCC	air-Brayton combined cycle
AMO	Advanced Manufacturing Office
ARPA-E	Advanced Research Projects Agency–Energy
ASME	The American Society of Mechanical Engineers
B&W	Babcock & Wilcox
BC	Bottom Cycle
BEC	bare erected cost
BOP	Balance of Plant
BPV	Boiler and Pressure Vessel
CAPEX	Capital Expenditure
CC	combined cycle
CEC	California Energy Commission
CEPCI	Conversion Factor of Chemical Engineering Plant Index
CFD	computational fluid dynamic
CSM	Colorado School of Mines
CSP	Concentrating Solar Power
DAYS	Duration Addition to electricitY Storage
DEM	discrete element method
DOE	U.S. Department of Energy
DSC	differential scanning calorimetry
ENDURING	Economic Long-Duration Electricity Storage by Using Low-Cost Thermal Energy Storage and High-Efficiency Power Cycle
ETES	Electric-Thermal Energy Storage
FEA	finite element analysis
GE GRC	General Electric Global Research Center
GE	General Electric
GTCC	gas turbine combined cycle
GTW	Gas Turbine World
HPC4ei	High-Performance Computing for Energy Innovation
HRSG	heat recovery steam generator
HX	heat exchanger
IP	intellectual property
LCOS	levelized cost of storage
LDES	long-duration electricity storage
MFIX	Multiphase Flow with Interphase eXchanges
NETL	National Energy Technology Laboratory
NGCC	natural gas combined cycle
NREL	National Renewable Energy Laboratory
NTU	Number of Transfer Units
NYPA	New York Power Authority
O&M	Operation & Maintenance
OTT	Office of Technology Transitions
PFB HX	pressurized fluidized bed heat exchanger
PFBPV	pressurized fluidized bed pressure vessel
PTES	pumped thermal energy storage

RTE	round-trip efficiency
SBIR	Small Business Innovative Fund
SCR	Selective Catalytic Reduction
SETO	Solar Energy Technologies Office
SOC	State of Charge
T2M	technology to market
TEA	Technoeconomic Analysis
TES	thermal energy storage
TIT	turbine inlet temperature
UA	Conductance

Executive Summary

Robust, efficient, cost-effective long-duration electricity storage (LDES) solutions can enhance grid resiliency, support existing transmission and distribution infrastructure, and enable a greater share of low-cost, variable sources of wind and solar to penetrate the market. The National Renewable Energy Laboratory (NREL) aims to meet this need by developing a transformative LDES system aptly named the Economic Long-Duration Electricity Storage by Using Low-Cost Thermal Energy Storage and High-Efficiency Power Cycle (ENDURING). The ENDURING system comprises high-temperature, low-cost particle thermal energy storage coupled with an advanced pressurized fluidized bed heat exchanger (PFB HX) that supports a high-efficiency, air-Brayton combined power cycle. At times of low energy demand (or high renewable production), a particle heater uses low-cost grid electricity to heat large volumes of solid particles to temperatures in excess of 1100°C, effectively charging the system. Later, to discharge the system at times of high energy demand (or low renewable production), these hot particles are gravity-fed through a PFB HX, where they transfer the heat to working fluid to drive a high-efficiency gas turbine power generation system, thereby converting the thermal energy back into electricity for the grid. The cold particles leaving the PFB HX are returned to the storage silos via a well-insulated particle conveyor. Unlike various alternatives, this LDES system can be sited anywhere for energy demand. With the option to site the LDES system at retired coal plants to leverage existing power generation infrastructure, the system can benefit the owners of otherwise retired coal-fired power plants by providing them with new revenue in grid storage to secure the future electric grid with the added benefit of enabling a source of continued employment within the local community.

The ENDURING system takes advantage of stable, inexpensive silica sand sustainably produced in the Midwestern United States as the thermal storage medium. Over the course of this ARPA-E 3-year funded project, we have successfully developed the ENDURING system configuration and component designs. Key component designs and performance were validated with prototype testing and model simulations. Prototype testing has demonstrated the component operation mechanisms, and the modeling methods have been verified against the experimental testing data. Product-scale component models and integrated system modeling have simulated the commercial-scale designs and predicted performance that achieves initial design goals. We performed cost analysis at the component and system level based on bare erected cost estimation before pandemic and supply chain constraints. Various deployment paths were compared to potentially meet the project's 5¢/kWh storage cost target by leveraging the infrastructure of existing thermal-power plants to minimize capital investment. The development shows that the technology is promising for future demonstration and subsequent commercialization. In addition, technology applications beyond electricity storage were explored for industry process heat and showed potentials in broad decarbonization by integrating with renewable energy supply.

The project involved considerable industry participation, including General Electric (GE; power cycle analysis), Babcock & Wilcox (B&W), Allied Mineral Products (insulation materials), and Worley-Advisian (system integration). These industry participants provided insights for component and system designs. The project successfully evaluated technology feasibility and has generated four awarded patents, five published journal papers, and a book chapter. Several manuscripts were under preparation, in addition to conference papers and presentations. An intellectual property (IP) option agreement has been signed with a U.S. manufacturer.

Table of Contents

Executive Summary	vii
1 Accomplishments and Objectives	1
2 Project Activities	7
2.1 Task 1. Design and Analysis of Sub-Scale and Full-Scale Systems	7
2.1.1 Storage Media Selection and Particle Stability	7
2.1.2 System Configuration and Component Specifications for TES Development.....	10
2.1.3 Brayton Combined-Cycle Power System Configuration and Performance	12
2.1.4 Key Component Designs and Analysis and System Economics	21
2.2 Task 2. Cold PFB Prototype Development and Testing.....	44
2.3 Task 3. Particle Heating Demonstration and TES Model Validation.....	46
2.3.1 Electric Charger Heater Design and Prototype Development.....	46
2.3.2 Particle TES Design and Modeling.....	51
2.3.3 Particle Heating Cycling Demonstration.....	56
2.4 Task 4. Hot PFB Prototype Development and Testing	57
2.5 Task 5. Full-Scale System Modeling	59
2.5.1 Component Model Development and Validation.....	60
2.5.2 System Modeling and Results	73
References	75
Project Outputs	78
Summary of Technology Achievements	78
Journal Articles	78
Papers (Manuscripts in Preparation)	79
Status Reports (Conference and Workshop Presentations)	79
Media Reports	80
Patent Applications/Issued Patents.....	80
Licensed Technologies	81
Awards, Prizes, and Recognition	81
Follow-On Funding	81

List of Figures

Figure 1. Configuration of a particle ENDURING system based on an air-Brayton combined cycle for thermal electricity generation.....	1
Figure 2. Experimental setup used to purge a Lindberg/Blue MTM box furnace.	8
Figure 3. Particle distribution shifts after 25, 50, and 100 cycles relative to the baseline for silica type 460.	8
Figure 4. Heat capacity of quartz from 300°C–1,200°C, including the α - β inversion at 573°C, and specific heat with temperatures measured by DSC (Netzsch STA 449 F3 Jupiter).	9
Figure 5. System flow diagram and storage configuration using particle TES with ABCC power generation for ETES.....	11
Figure 6. The open-loop configuration of the power generation subsystem.....	13
Figure 7. The closed-loop configuration of the power generation subsystem.	13
Figure 8. At >1,150°C turbine inlet temperature, the Class-E GTCC can achieve >52% efficiency, and a Class-E turbine was referred for ABCC performance (from reference [6]).....	14
Figure 9. A GE 7E.03 gas turbine with the top casing removed and the retrofit approach.	16
Figure 10. A path for further improving ABCC power efficiency via compressor inlet air cooling and increasing the turbine inlet temperature.	17
Figure 11. Turbine and storage layout for an assumed 3:1 ABCC plant. Modular PFB HX and TES are coupled to each Brayton turbine. Three Brayton turbines share one steam turbine.....	20
Figure 12. Media flow and heat/mass balance in computation tool.....	21
Figure 13. Capital cost levels defined by NETL.....	23
Figure 14. Power system layout and ENDURING plant schematic.	33
Figure 15. Published NGCC BEC data.	34
Figure 16. Cost breakdown of essential components or sectors in a conventional combined cycle gas plant.....	35
Figure 17. Average cost breakdown percentages of essential components or sectors in a conventional combined cycle gas plant.	36
Figure 18. New construction ENDURING ABCC power plant layout.	37
Figure 19. A storage configuration built on a retrofitted NGCC plant.	38
Figure 20. A storage configuration built upon a retrofitted coal plant.....	39
Figure 21. Capital costs of different ENDURING plant scenarios for a capacity of 405 MWe.	40
Figure 22. TEA scenarios for achieving the 5¢/kWh LCOS target (20 years life).	42
Figure 23. Techno-Economic Analysis sensitivities for a path to achieve the 5¢/kWh LCOS target: charging electricity price and round-trip storage efficiencies are two significant factors besides capital costs.	43
Figure 24. The design of a PFB for direct air/particle heat transfer.....	45
Figure 25. Cold PFB prototype fluidization test at ambient, pressurized conditions.....	45
Figure 26. Modular design of electric particle heater for charging particle TES. <i>Illustrations and Photo by NREL</i>	47
Figure 27. Overview of the MFIX-DEM modeling effort, including (a) definition of the modeling domain, (b) particle velocity contour plot, and (c) average particle temperature profiles for several geometry angles as a function of heater depth over the computational domain.	48
Figure 28. Experimental results, including (a) testing of four different cases from the parametric study described in Section 3.1.2 and (b) determination of the resulting mass flow rates.....	49
Figure 29. Detailed rendering of the entire assembly (left), a cross section revealing the particle flow path (middle), and an image of the assembled test station (right).	50
Figure 30. Effects of surface angle and friction on the overall heat transfer coefficient.	51
Figure 31. Particle TES containment design and insulation layers.....	52
Figure 32. Graphical representation of the mathematical description of both the volume and the insulation model that comprise a single particle storage silo model.....	53

Figure 33. Bulk average particle temperature over selected operational cycles; not all cycles are presented for conciseness. Vertical dotted lines mark changes in operating step; x-axis is not to scale.	54
Figure 34. Temperature profiles from product-scale TES containment model.....	55
Figure 35. Temperature profiles of (a) cycle 1: 1,100°C and (b) cycle 7: 1,250°C.	56
Figure 36. Cumulative particle size distributions before and after particle heating.....	57
Figure 37. The design of a PFB in batch operation for direct air/particle heat transfer.....	58
Figure 38. Sample results from both scales of CFD models of PFB HX.....	58
Figure 39. Integrated system model for a 10-hour ENDURING system with inputs for dispatch signal, ambient temperatures, and ambient pressure.	60
Figure 40. Validation pathways for the three key Modelon-based ROMs.....	62
Figure 41. Heater array control logic based on dispatch signal.	63
Figure 42. Example result of heater array controller processing dispatch signal.	63
Figure 43. Comparison of 1D temperature profiles predicted by the high-fidelity MFIX and Modelon-based ROM of the electric particle heater at two different surface angles (θ) and friction coefficients (μ).	65
Figure 44. Fully packaged particle storage array model with connection points (class). Individual components that comprise the particle storage array model and the components' structure (subclass).....	66
Figure 45. SOC of the particle storage silo over a seven-day cooling process.	67
Figure 46. Comparison of the (a) gas-phase bed pressure drop and (b) effectiveness predicted by high-fidelity CFD and Modelon-based ROM models of the PFB HX with 10% error bars.	68
Figure 47. Simplified combined cycle gas turbine model for 7E.03 developed in Modelon Impact.....	69
Figure 48. Comparison of performance of baseline 7E.03 CC model vs. modified CC with PFB HX BC efficiency refers to second law exergetic efficiency.	70
Figure 49. Effect of particle temperature and mass flow rate on net power produced in the modified CC cycle with PFB HX.	71
Figure 50. Effect of combustor (or heat exchanger in storage operation) pressure drop on (a) simple and combined cycle power and efficiency and (b) turbine inlet temperature.	72
Figure 51. Performance map component of the power cycle, built in Modelon Impact.....	73
Figure 52. The impact of simulation time on predicted RTE. Dispatch signal for this simulation contained a pause in the operation of the storage system during the summer due to grid price signals, therefore, the RTE is constant in this region until operation is resumed.	73
Figure 53. The relative change in RTE to base case (relative insulation thickness equal to 1) for different relative insulation thicknesses for different assumed operating schedules (i.e., days between charge and discharge cycles).....	74

List of Tables

Table 1. Key Tasks, Milestones, and Deliverables	2
Table 2. Physical Properties of Silica Sand as Storage Medium	9
Table 3. Specification of Commercial-Scale System and Components.....	12
Table 4. Comparison Between Published Data and Modeling Results for 7E.03 CC	15
Table 5. Firing Temperatures of GE Turbines.....	16
Table 6. Simulation Results for Various Plant Configurations and Process Conditions	18
Table 7. Open-/Closed-Loop Cost Comparison Summary	20
Table 8. Key Component Designs and Laboratory Prototypes for the Particle ETES System.....	22
Table 9. Particle Containment Silo Design Specifications and Cost Estimation	25
Table 10. Particle Lifting Skip Hoist Design Specifications and Cost Estimation of Key Parts Excluding Supporting Structure and Motor Power Control	26
Table 11. Cost Factors of Power-Specific Components	27
Table 12. Air Pipeline Design Specifications and Cost Estimation.....	29
Table 13. Design Specifications and Cost Estimation	30
Table 14. Design Specifications and Cost Estimation	31
Table 15. Design Specifications and Cost Estimation	32
Table 16. Estimated Capital Costs of Different Storage Configuration Scenarios	40
Table 17. Input Values for Power System Integration Scenarios	41
Table 18. Sensitivity Analysis Input Values	42
Table 19. Summary of Component Model Development	61
Table 20. Combined Cycle Performance Estimates Comparison: Modelon vs. HYSYS	70
Table 21. Follow-On Funding Received.....	81

1 Accomplishments and Objectives

Funded by ARPA-E Duration Addition to electricity Storage (DAYS) program, Figure 1 shows the schematic of the Economic Long-Duration Electricity Storage by Using Low-Cost Thermal Energy Storage and High-Efficiency Power Cycle (ENDURING) system developed in this project. The system performs as a thermal battery, which charges the thermal storage by using low-cost, off-peak electricity to heat solid particles. Heated particles are then stored in internally insulated containment silos. At peak-demand hours, stored thermal energy is discharged through a fluidized bed heat exchanger to drive a combined-cycle power system. The project aims to develop a full-scale system design with a round-trip efficiency (RTE) of $\geq 50\%$.

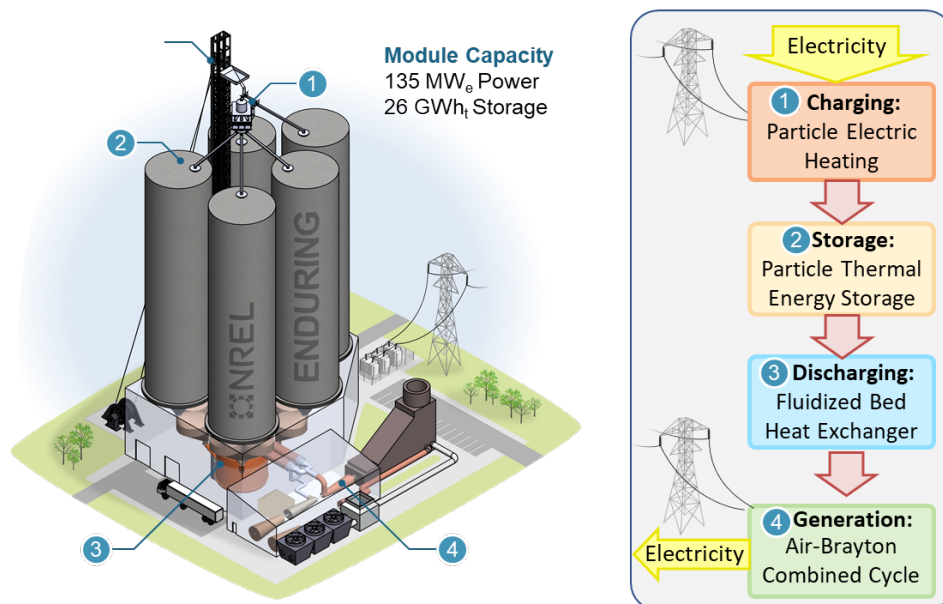


Figure 1. Configuration of a particle ENDURING system based on an air-Brayton combined cycle for thermal electricity generation.

The project team has successfully achieved the original goals and milestones set for this project. Table 1 shows the major tasks, key milestones, and deliverables from the project. Project objectives were aimed at project objectives of a conceptual full-scale system design and analysis demonstrating a round-trip efficiency (RTE) of $\geq 50\%$ and capital costs of \$650/kW (power components only) and \$2/kWh_t (energy-storage specific components). The estimation was based on material and fabrication cost for bare erected cost and performed before Covid-19 pandemic and supply chain constrain, and might change with economic conditions. The project developed modeling tools and testing prototypes to validate the component design approaches, operation, and performance evaluation.

Table 1. Key Tasks, Milestones, and Deliverables

Task 1: Design and analysis of sub-scale and full-scale systems.
Subtask 1.1: Finalization of agglomeration, attrition, fluidization, pressure drop, and heat transfer metrics for the system.
<p>M1.1 – Finalization of agglomeration, attrition, fluidization, pressure drop, and heat transfer metrics (completed, Q1).</p> <ul style="list-style-type: none"> Finalize the metrics (demonstrated in M1.4) for particle agglomeration and particle attrition related to both thermal and mechanical aspects. Finalize the nondimensional particle size (5–40) and nondimensional velocity (0.2–2) for the full-scale and sub-scale demonstration systems. Nondimensional particle diameter and velocity are defined as per Ibanez et al. [1]. Estimate dP/dz, $d\dot{q}/dz$, and dT/dz (~300°C/m) metrics for full-scale and sub-scale systems. dP/dz will be evaluated for the PFB flow design and benchtop PFB HX. dP/dz, $d\dot{q}/dz$, and dT/dz will be tested using the benchtop PFB HX.
Subtask 1.2: Pressurized fluidized bed (PFB) flow test design.
<p>M1.2 – PFB flow test design (completed, Q2).</p> <ul style="list-style-type: none"> Reviewed PFB flow test design and analysis with ARPA-E team. Cold PFB design completed, and appropriate metrics finalized for operation at 25°C and 1.5 atm. Nondimensional particle size and nondimensional velocity matched the metric defined in M1.1.
Subtask 1.3: Closed vs. open Brayton cycle performance and cost study.
<p>M1.3 – Closed vs. open Brayton cycle performance and cost study (completed, Q4).</p> <ul style="list-style-type: none"> Team presented cycle modeling and cost trade-off studies for open Brayton cycle and closed Brayton cycle concepts with and without water/fog injection for the full-scale system. Down-selected to GE turbine types (7E versus 9E or GT13) and Brayton cycle design.
Subtask 1.4: Particle stability test.
<p>M1.4 – Particle stability test (completed, Q2 and Q3).</p> <p>Stability testing for three types of particles at three different conditions was completed. At least one particle type met requirements on thermal stability, cost, and agglomeration as defined below:</p> <ul style="list-style-type: none"> Tests performed with silica sand, calcined flint clay, and brown fused alumina with pure N₂ (or other inert), with N₂ (or other inert) at 50% relative humidity, and with air at 50% relative humidity. Demonstrated thermal stability (including sintering/agglomeration) of particles. Particles held at 1,200°C for 100 hours and cycled 100 times between 300°C and 1,200°C. Measured average particle size for three random samples of particles before and after high-temperature treatment in a crucible at regular intervals. Average particle diameter of the 10 samples did not exceed 50% variation from the initial average particle diameter of the three samples. Investigated the particle distribution, mode, skewness, and kurtosis, and ensured 90% of particles were within 75–600 μm. Cost of the particles was ≤\$1.3/L. Validated agglomeration metric as defined in M1.1.
Subtask 1.5: Design review of 10-kW heater and TES insulation test.
<p>M1.5 – Design review of 10-kW heater and TES insulation test (completed, Q4).</p> <ul style="list-style-type: none"> 10-kW heater design: Defined the number of passes needed for heating the particles from 25°C to 1,200°C. Presented a layout of the prototype and testing procedure. Achieved a model-predicted heat transfer coefficient (h) ≥ 500 W/m²K.

<ul style="list-style-type: none"> • TES insulation: Insulation material (refractory and second layer) compatibility tested at 1,200°C for 100 hours. Experimentally demonstrated <3% degradation in insulation effectiveness after 100 hours at 1,200°C. Insulation compatibility test was performed with Brayton cycle working fluid (N₂ and air) with water vapor.
Subtask 1.6: Design review of PFB hot heat exchanger (HX).
<p>M1.6 – Design review of PFB hot HX (completed, Q5).</p> <ul style="list-style-type: none"> • Design and analysis of PFB benchtop HX for characterizing heat transfer for 10-bar operation at an inlet temperature of 300°C and an outlet temperature of 1,170°C. Refined dP/dz, dT/dz, and dq/dz values have been demonstrated.
Subtask 1.7: PFB benchtop computational fluid dynamics (CFD) model and full-scale system design review.
<p>M1.7 – PFB benchtop CFD model and full-scale system design review (completed, Q6).</p> <p><i>Components and subsystems</i></p> <ul style="list-style-type: none"> • PFB benchtop sub-scale Lagrangian-Eulerian (particle-gas) CFD model predictions of dP/dz, dT/dz, and dq/dz (flow and heat transfer). Developed and validated the Eulerian-Eulerian (gas-gas) CFD model with the Lagrangian-Eulerian model for the PFB benchtop setup. Discrepancies between the two models' results were ≤10%. <p><i>Full-scale system</i></p> <ul style="list-style-type: none"> • Design and analysis of full-scale system met the RTE target of ≥50%. Brayton cycle plus steam cycle models demonstrated >54% efficiency. • Techno-economic analysis met the capital expenditure (CAPEX) requirements: installed capital cost of \$650/kW (power components) and \$1–\$2/kWh (energy-storage components). Cost breakdown was completed for major power block components (gas turbine, steam bottoming cycle, BOP, estimates for PFB HX and gas turbine modifications). Showed a pathway to a combined metric of \$0.05/kWh-cycle at 100-hr duration (Figure 2(b) of the DAYS Funding Opportunity Announcement by ARPA-E).
Task 2: PFB flow test.
Subtask 2.1: Demonstration of PFB flow test.
<p>M2.1 – Cold PFB prototype development and testing (completed, Q7).</p> <p>Built and demonstrated a transparent PFB flow test for visualizing particle flow under 25°C and 1.5 atm. Mass flow rate and other conditions represented similitude to the full-scale system. Simulation of the PFB test system was completed for model validation.</p> <p>Demonstrated operation at 25°C and 1.5 atm with down-selected particle type:</p> <ul style="list-style-type: none"> • Confirmed no visual stagnation and channeling through the particles. $\Delta P/\Delta P_{\text{fluidization}}$ value was less than 6% of the intake pressure. Both measured and modeled ΔP was within 6% of intake pressure and met M2.3 for the full-scale design. • Visually confirmed that the fluidized bed top was flat and measured the temporal evolution of the bed height. • Validated that the nondimensional velocity matches the value established in M1.1, and validated that the nondimensional particle diameter matches the value established in M1.1. Verified that the process is in the fluidization regime.
Subtask 2.2: PFB flow test: validation of measured and simulated ΔP .
<p>M2.2 – PFB flow test: validation of measured and simulated ΔP (completed, Q8).</p> <ul style="list-style-type: none"> • Measured ΔP matched the Lagrangian-Eulerian CFD model-predicted value (M1.7) within 10% (25°C and 1.5-atm operation of the PFB flow test).

Subtask 2.3: Gas distribution design for full-scale system.
<p>M2.3 – Gas distribution design for full-scale system (completed, Q9).</p> <ul style="list-style-type: none"> • Recommended gas distribution design for full scale system based on PFB flow test learnings. • Designed ΔP less than 6% of the intake pressure for Brayton cycle integration.
Task 3: Demonstration of particle heating with 10-kW heater.
Subtask 3.1: Particle heating batch demonstration.
<p>M3.1 – Particle heating batch demonstration (completed, Q11).</p> <ul style="list-style-type: none"> • Demonstrated that the 10-kW heater can heat particles from an initial temperature of 300°C to 1,200°C. Demonstrated both batch and cycling operation. • 10-kW heater built and tested to demonstrate heating of particles from 300°C to 1,200°C, with the number of passes as defined in milestone M1.5. • Demonstrated a heat transfer coefficient (h) > 500 W/m²/K (heater area). Evaluated heater cost is <\$15/kWt.
Subtask 3.2 Particle heating cycling demonstration.
<p>M3.2 – Particle heating cycling demonstration (completed, Q12).</p> <ul style="list-style-type: none"> • 10-kW heater used to heat particles from 300°C to 1,200°C, then particles were cooled down. One hot/cold cycle was conducted per day for 7 continuous days. • Confirmed particle stability with the metrics from M1.4.
Subtask 3.3: TES model validation.
<p>M3.3 – TES modeling validation (completed, Q12).</p> <ul style="list-style-type: none"> • Predicted heat losses from a silo using a conjugate heat transfer model for 100-kWht TES. The model was validated against testing data from a small-scale TES system within <10% uncertainty.
Task 4: Testing of benchtop PFB HX and TES system. Full-scale PFB CFD model development and validation.
Subtask 4.1: Measurement of preliminary heat transfer metrics on benchtop HX
<p>M4.1 – Preliminary heat transfer metrics measured on benchtop HX (completed, Q8).</p> <ul style="list-style-type: none"> • Built and demonstrated the operation of the benchtop PFB HX for characterizing fluidization and heat transfer. Developed and validated full-scale CFD model for the PFB. • The benchtop HX was assembled, tested at 10-atm pressure and particle inlet temperature of 300°C, and provided initial data on dq/dz, dT/dz, and dP/dz. The benchtop setup was instrumented with thermocouples, and the temperature stratification in the fluidized bed was measured as a function of bed height. The air outlet temperature was characterized, and the air was heated by hot particles to the desired temperature in M4.3.
Subtask 4.2: Full-scale flow and heat transfer CFD model predictions.
<p>M4.2 – Full-scale flow and heat transfer CFD model predictions (completed, Q8).</p> <ul style="list-style-type: none"> • Evaluated ΔP for the full-scale PFB system using the Eulerian-Eulerian CFD model, and predicted ΔP within 10% of the experimental value (M2.1). • Fluidized bed HX Eulerian-Eulerian CFD model to match within 10% of the benchtop Lagrangian-Eulerian CFD predictions and predicted dT/dz, dP/dz, and dq/dz (M1.7).
Subtask 4.3: Final demonstration of benchtop HX.

<p>M4.3 – Final demonstration of benchtop HX (completed, Q11).</p> <p>Demonstrated the operation of the benchtop HX (5-kW thermal) at 10-atm pressure and 300°C inlet gas temperature:</p> <ul style="list-style-type: none"> • Confirmed that nondimensional particle size is between 5 and 20 and nondimensional velocity is between 0.2 and 1. • Lagrangian-Eulerian CFD predictions matched values of tested dq/dz, dT/dz and dP/dz within 10% (M1.7) with a particle inlet temperature of 300°C.
Task 5: Full-scale Modelica model performance.
Subtask 5.1: Power cycle layout and initial results from full-scale Modelica model.
<p>M5.1 – Initial results from full-scale Modelica model (completed, Q10).</p> <ul style="list-style-type: none"> • Developed and integrated sub-models for Brayton cycle (open or closed) and thermal energy storage systems.
Subtask 5.2: Refinement and validation of full-scale Modelica model.
<p>M5.2 – Refinement and validation of full-scale Modelica model (completed, Q12).</p> <ul style="list-style-type: none"> • Full-scale Modelica simulations were refined and predicted an RTE >50% with Brayton cycle efficiency >54%. Component sub-models were validated against experimental data.
Task 6: Technology-to-market (T2M) transition. Deliver T2M plan, IP strategy, and product manufacturing plan.
Subtask 6.1: T2M plan v.1.
<p>M6.1 – T2M plan v.1 (completed, Q2).</p> <ul style="list-style-type: none"> • Provided an initial T2M plan that describes what product will be “sold” from the technology developed, and how it will be provided (manufacturer sale or licenses). Also described critical customers and partners in the T2M plan that have been outreached/engaged throughout the project.
Subtask 6.2: T2M plan v.2.
<p>M6.2 – T2M plan v.2 (completed, Q5).</p> <ul style="list-style-type: none"> • Updated the plan based on learnings from the market, technology, and manufacturing economics. Assessed the team’s ability to meet them and identified gaps to moving forward.
Subtask 6.3: T2M plan v.3.
<p>M6.3 – T2M plan v.3 (completed, Q9).</p> <ul style="list-style-type: none"> • Updated the T2M plan, identified potential partners and funding groups, and provided a strategy to move on those. Also conducted a market assessment for assisting near-term market entry and for meeting the long-term DAYS Program goal.
Subtask 6.4: Definition of initial assets. Subtask 6.5: Determination of prior art.
<p>M6.4 & 6.5 – Define initial assets and determine prior art (completed, Q2 & Q3).</p> <ul style="list-style-type: none"> • Defined inventions, including both basic technologies and potential products. Investigated potential competing technologies and compared them with the ENDURING technology developed during this project.
Subtask 6.6: Preliminary economics and supply chain and product scale-up.

M6.6 – Product manufacturing concept.

- Defined the basic components of the ENDURING product and estimated the basic materials cost and the cost to manufacture, which is established by analogy to existing devices or materials.
- Considered preliminary economics and supply chain with industry partners.
- Expanded the manufacturing plan with details of the supply chain and further economics. Provided a sensitivity analysis that showed which aspects of the product will dominate cost and which aspects are therefore useful to improve upon.

Provided a plan for scaling up and manufacturing ENDURING product:

- Subscale plant layout: Evaluated the potential of modifying an existing small gas turbine in the 2–10-MWe size range for a subscale risk reduction demonstration plant. Scoped to include gas turbine, PFB HX, particle storage, and heater.

The project has achieved all its milestone goals for feasible development of the ENDURING system through system analysis and component design, modeling, and laboratory prototype testing. The following sections detail the project tasks and the major outcomes. Task 6 T2M plans were not included in this final report to the public due to the business sensitivity of NREL and partners.

2 Project Activities

The ENDURING project consisted of five technology development tasks and one technology-to-market task as shown in Table 1. Tasks supporting technology development included the design and techno-economic analysis (TEA) of sub-scale and full-scale systems (Task 1), testing of critical system components (Tasks 2-4), and the development of a verifiable Modelica-based performance model designed to predict the performance of a full-scale ENDURING system (Task 5). The project focused on designing and, where appropriate, de-risking critical components through prototype testing. The components include the high-temperature electric heater used for charging, low-cost thermal energy storage modules, a high-performance heat exchanger, and the air-Brayton combined-cycle (ABCC) power system. Associated cost targets included targeted capital costs of \$650/kW (power-relevant components) and ~\$2/kWh (energy-storage-specific components). This report documents the outcomes of the ENDURING technology development and project activities undertaken to achieve the milestone goals. Task 6, technology-to-market plans, was not included in this report because it involved confidential discussions and business strategies inputted from industry partners.

2.1 Task 1. Design and Analysis of Sub-Scale and Full-Scale Systems

2.1.1 Storage Media Selection and Particle Stability

(Note: Work contributed by Patrick Davenport.)

A first step in storage development included screening and selecting the storage medium, which in this case required stable, low-cost particles. Detailed studies have been performed on the thermal stability, material compatibility, and physical properties of silica sand. The durability of silica sand has been tested for 500 hours at 1,200°C with the presence of refractory coupon samples. The particle stability tests were conducted in a Lindberg/Blue box furnace equipped with a gas inlet. The furnace was ramped to 1,200°C (10°C/min), held for 500 hours, and left to cool to ambient temperature at its natural cooling rate. In each case, the respective cover gas was supplied at a rate of 400 sccm (standard cubic centimeter) to refresh the furnace volume approximately every 15 minutes. Figure 2 shows the experimental setup used to supply the furnace with 50% partial pressure steam. This includes (1) supplying the furnace with humidified air ($p_{H_2O} = 50\%$) for 500 hours. Supply gas (2) is then bubbled through a humidifier (3) at a rate of 400 sccm. The humidifier and subsequent delivery line (4) are maintained by set point in a controller (5) at 80°C and 90°C, respectively, to prevent condensation. A deionized water reservoir (6) maintains the humidifier via a solenoid valve actuated by an optical water-level sensor (7). Humidified air ($p_{H_2O} = 50\%$) is confirmed using an in-line humidity meter (series HMT330).

The focus of the particle stability tests was on the particle size changes during the heating and cycling processes, including particle agglomeration or sintering at high-temperature conditions. Particle size was measured by Mastersizer laser diffraction particle size analyzers produced by Malvern Panalytical Company. These analyzers measure particle sizes ranging from 0.02 μm to 2000 μm . We measured the particle sizes before and after the particle heating and cycling tests to gauge the particle size stability and screened the particles through a mesh to observe if agglomeration had occurred.

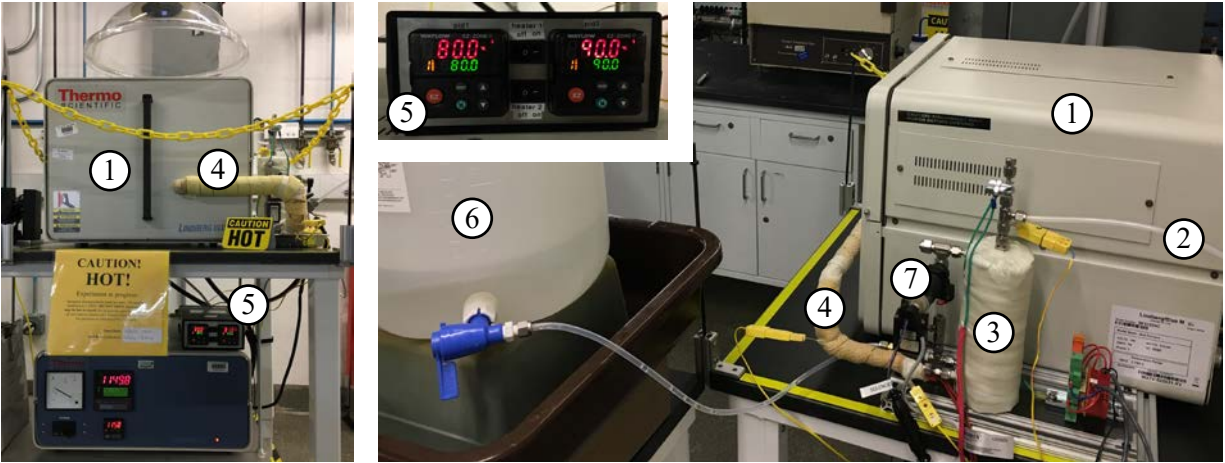


Figure 2. Experimental setup used to purge a Lindberg/Blue MTM box furnace.

Thermal cycling tests were performed between 300°C and 1,200°C for 100 cycles, and no obvious size change was observed, as shown in Figure 3. These thermal tests verified both the stability and the compatibility of the particles with the refractory insulations [2].

Figure 3 shows typical results from the thermal cycling tests as well as the heat capacity measurements of silica sand type 460 supplied by Covia [3]. The thermo-cycle test results shown in Figure 3 indicate size changes of approximately 3% after 100 thermal cycles.

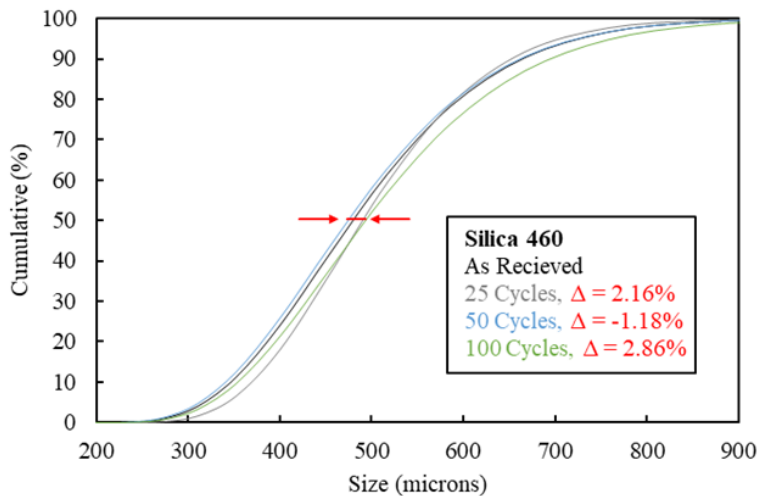


Figure 3. Particle distribution shifts after 25, 50, and 100 cycles relative to the baseline for silica type 460.

The results indicate that the silica sand particles have adequate stability in their service life, while fine particles generated from storage cycles can be replenished regularly to maintain a desired particle size distribution inside the system. No agglomeration was observed for silica 460 after heating to 1,400°C, indicating particle reliability in thermal storage use.

Figure 4 shows the specific heat as a function of particle temperature from National Institute of Standards and Technology data sources and actual differential scanning calorimetry (DSC)

measurements taken using a Netzsch STA 449 F3 Jupiter. The heat capacity of silica sand varies with temperature and has a peak point associated with α - β quartz inversion. The potential negative effects of α - β quartz inversion at approximately 573°C on particle durability or fluidization have not shown up in thermal cycle tests or benchtop heating tests. The average specific heat capacity within the operational temperature range of 300°–1,200°C is greater than 1.1 kJ/kg-K, indicating an adequate capacity for sensible heat energy storage based on a reasonable containment design.

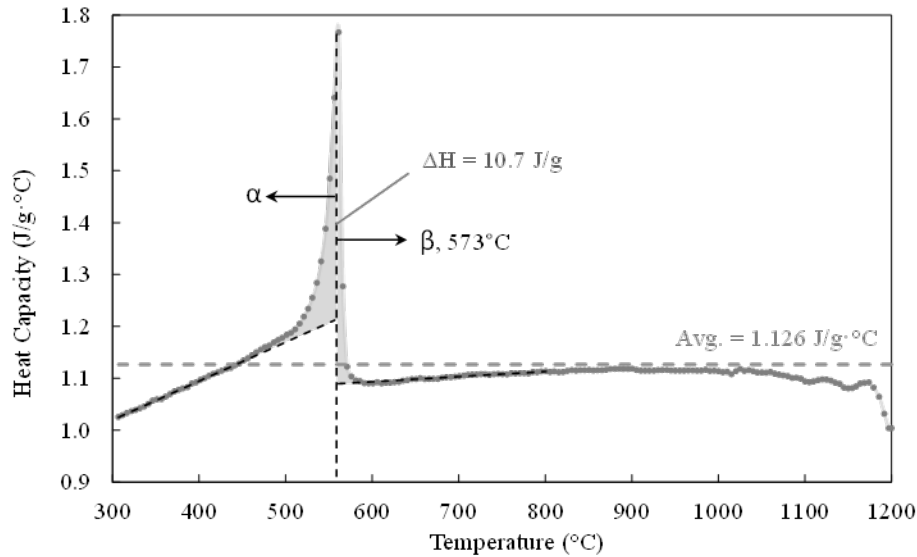


Figure 4. Heat capacity of quartz from 300°C–1,200°C, including the α - β inversion at 573°C, and specific heat with temperatures measured by DSC (Netzsch STA 449 F3 Jupiter).

Silica sand is mined in the Midwestern United States and is selected from product lines with high SiO₂ purity (>99%, as shown in Table 2).

Table 2. Physical Properties of Silica Sand as Storage Medium

Particle Properties	Value	Unit
Particle average diameter	450	μm
Real particle density	2,650	kg/m ³
Bulk particle density	1,543	kg/m ³
Thermal conductivity (bulk)	1.402	W/m-K
Specific heat (temperature dependent)	Figure 4	J/kg-K
Composition [3]		
	SiO ₂	99.65%
	Al ₂ O ₃	0.065%
	Fe ₂ O ₃	0.018%
	CaO	0.012%
	TiO ₂	0.011%

Table 2 summarizes other thermal/physical properties of silica sand. High silica purity provides particle stability preventing sintering or agglomeration at high temperatures. The mined sand maintains the desired roundness for flowability. Similar particles have also been used in fracking applications. Vendor quotes indicate that silica sand costs \$30–\$40/ton, which is a fraction of the cost of molten salt or other typical thermal storage media.

With the verified silica sand as a storage medium, the system uses insulated concrete silos as TES containment to hold the heated and cooled particles. The TES module is scalable, with flexible storage capacity depending on the grid storage needs. The storage capacities can be sized to an electricity discharge duration ranging from less than 10 hours to more than 100 hours. The 100-hour, long-duration storage module shown in Figure 1 consists of four particle containment silos and one buffer silo for temporary transfer of particles. Each containment silo can store either hot or cooled particles, thus eliminating nearly half of the storage containment cost compared to separate hot/cold storage. A buffer silo is used to temporarily store low-temperature particles when a containment silo is not completely emptied during discharging, enabling flexible charging/discharging operations. A single full TES silo stores 6.5 GWh_{th}, or approximately 25 hours of full-load, 135-MW_e ABCC operation, based on an existing air turbine combined-cycle system, as described in Section 3.4. Four TES silos contain approximately 26 GWh_{th} to provide 100-hour storage duration as one storage module. The low effective thermal conductivity through the packed particle bed means that static stored particles reduce thermal conduction during the storage period by forming a self-insulating layer. With the internally insulated TES containment, heat loss can be limited to less than 1% per day using the insulation designs that have been analyzed [4].

2.1.2 System Configuration and Component Specifications for TES Development

The particle ETES system includes an electric charging particle heater, TES modules, skip hoists for transporting particles, a PFB HX, and a high-performance ABCC power generation system. Figure 5 shows the storage process, the energy flow, and air and particle flow paths through the charging and discharging components.

The ABCC power cycle, as shown in Figure 5 and discussed in Section 3.4, provides the operating parameters that determine the charging/discharging components and storage capacity. The PFB HX is based on the configuration of commercial PFB combustion boilers [5] and has an inner hot fluidized bed for air/particle direct contact heat transfer surrounded by an external pressure vessel to hold the air pressure. The ABCC power system is adopted from a commercial gas turbine combined cycle (GTCC) system by substituting gas combustors with hot air passages connected with the PFB HX. The high-pressure air from the turbine compressor contacts the hot particles, which are fed through the PFB HX and heated to the turbine inlet temperature. Entrained fine particles are removed via cyclone separators, and the hot air then flows through the turbine and drives a power generator. The turbine exhaust hot air flows through a heat recovery steam generator that drives a bottom steam Rankine power cycle. The current work investigated the particle ETES system and major components through conceptual design, performance modeling, and prototype testing.

Figure 5 shows the process flow diagram and the energy flow path during charging in which particles are heated via the charging electric heater and collected in the storage silo. When discharging, hot particles flow through a lock hopper to isolate the storage silo at ambient

pressure from the PFB HX. Many different ways have been developed to dispense particles into a pressurized vessel and to seal hot air, and many of these methods have been used in industry. A few examples include lock hoppers, as described for the particle inlets; rotary valves; and loop seals for fluidized beds. We decided upon lock hoppers to feed hot particles from a particle storage silo to the PFB HX in the ENDURING system. A lock hopper is a conventional device developed for integrated gasification combined cycle technology and has been applied broadly in process engineering and plants. Two such lock hoppers would operate alternately to maintain continuous particle flow to the PFB HX. Particles first fill the lock hopper container, and then the lock hopper is pressurized to a pressure equal to that of the PFB HX and then releases particles into the PFB HX gravitationally. Either a lock hopper or an array of rotary valves under the PFB HX is possible to dispense cooled particles exiting from PFB HX back to a storage silo. Currently, when low-temperature particles exit the HX, a pressure regulation rotary valve and transport to a buffer silo are used.

The particle storage containment was designed to store particles at both heated (1,200°C) and cooled (300°C) conditions and uses a concrete silo with refractory insulation liners. The particle TES uses stable, inexpensive silica sand and provides a large storage capacity and high-temperature energy. Such a temperature supports the ABCC power system studied below. Several particle transport methods are available to lift particles to the top of storage containment; however, transporting warm particles (~300°C) to a height of 100s meters is still uncommon and needs an industry supplier for commercial applications. In this project, a particle lifting skip hoist was selected to transport particles above the electric heater to charge the storage. A skip hoist can lift large quantities of bulk material efficiently, with two skips moving up/down in opposite direction to recover the potential energy of the opposing skip. Skips can be insulated to minimize heat losses to the ambient when lifting the hot particles.

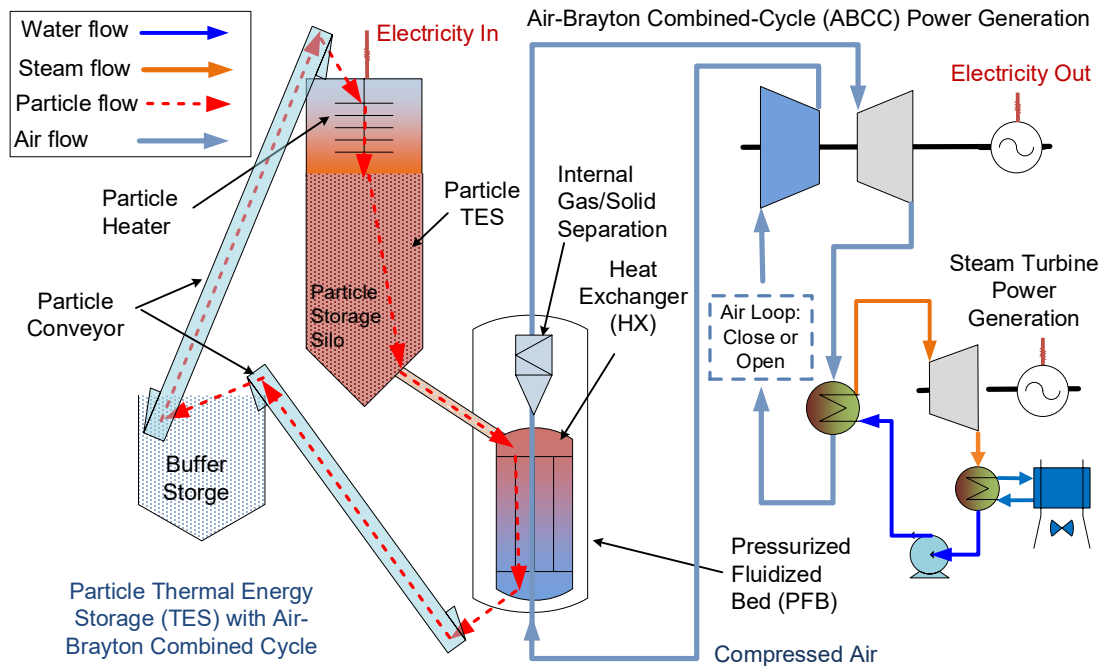


Figure 5. System flow diagram and storage configuration using particle TES with ABCC power generation for ETES.

The component specifications for the system diagram shown in Figure 5 are listed in Table 3 and serve as design conditions for component sizing and configuration. Component designs are based on heat/mass balances for the electric heater, particle TES, PFB HX, and auxiliary equipment, including particle transport and compressed air connections with the power block. The power-specific components include the power blocks and the components for energy conversion, including the PFB HX.

Table 3. Specification of Commercial-Scale System and Components

Items	Preliminary Design Specifications
Storage module	135-MW _e discharge electric generation capacity 26-GWh _{th} storage capacity (100 hours at full-load discharge capacity) RTE >50%
Particles as storage media	Silica sand with >99% silica purity, stable at >1,200°C Cost: \$30–\$40/ton
Electric charging particle heater	315 MW _{th} Thermal efficiency ≥98% Outlet particle temperature ≥1,200°C
Particle thermal energy storage	7 GWh _{th} per storage silo Storage temperature ≥1,200°C <1% thermal loss per day
Lock hoppers	Feeds hot particles from ambient-pressure storage to PFB HX A pair of lock hoppers operate alternately to maintain constant particle flow into the PFB HX
Pressurized fluidized bed heat exchanger	Direct air/particle contact PFB HX design 300 MW _{th} , 292-kg/s air flow rate, 300-kg/s particle flow rate Air inlet temperature: 300°C Air outlet temperature ≥1,170°C
Air-Brayton combined-cycle power system	Refractory-insulated piping for air connections Air-Brayton combined cycle >52% power generation efficiency

2.1.3 Brayton Combined-Cycle Power System Configuration and Performance

(Note: Work contributed by General Electric Global Research Center’s Dr. James Tallman, Dr. Naveenan Thiagarajan, Dr. Doug Hofer, and Dr. Ching-Jen Tang.)

The cost and performance of the power generation subsystem are critical to the overall value proposition of the ENDURING energy storage system. General Electric Global Research Center (GE GRC) conducted cycle modeling of the power system and has completed a performance and economic evaluation of two cycle configurations: open- and closed-loop systems. The model was built based on relevant experience from GE GRC and knowledge of combined cycle (CC) power plants. The performance and water use of both open- and closed-loop power cycles show that the open-loop cycle is favorable.

2.1.3.1 Power Cycle Performance Models

An air Brayton cycle operates in a single working fluid phase without condensation or phase change. It is the same thermodynamic cycle run by natural gas turbines, which makes a gas turbine integrated with a steam turbine an ideal choice for the ENDURING energy storage system. Air was selected as a working fluid for the power cycle. The overall and subcomponent models for the gas turbine, particle HX, compressor, and steam cycle, and the interactions between the components, were developed using Aspen HYSYS software¹. Aspen HYSYS is a simulator used to mathematically model processes from unit operations to full plants. The HYSYS model was developed with mass balances, energy balances, vapor-liquid equilibrium, thermodynamic power cycle analysis, and component performance modeling. It can be used in HX design, steady-state and dynamic process simulation and design, and component and process optimization. The bottoming cycle and the optimization for the power generation subsystem were embedded in the model using Excel. Two cycle configurations—open and closed loops—were evaluated (Figure 6 and Figure 7, respectively).

The cycle consists of a compressor, particle HX, gas turbine, heat recovery steam generator (HRSG), and a steam turbine. The performance models can simulate each individual subsystem component, such as the gas turbine, particle HX, or exhaust gas cooler, as well as the interactions among the components. The description of the steam cycle performance was based on an analytic formulation² that draws upon the second law of thermodynamics in the form of an exergy balance. This formulation was embedded in the HYSYS model.

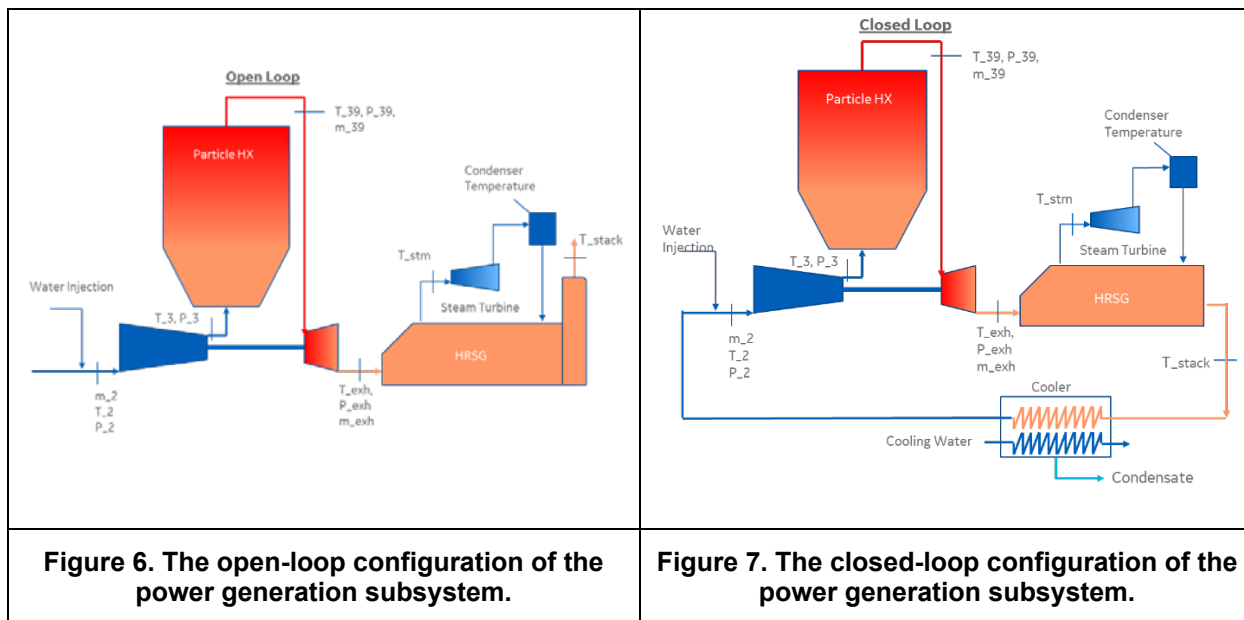


Figure 6. The open-loop configuration of the power generation subsystem.

Figure 7. The closed-loop configuration of the power generation subsystem.

¹ <https://www.aspentech.com/en/products/engineering/aspen-hysys>

² S. Gulen and R. Smith. "COMBINED CYCLE PERFORMANCE, PART I: 2NDLAW EFFICIENCY OF THE RANKINE BOTTOMING CYCLE". Proceedings of GT2008: ASME TURBO EXPO Power for Land, Sea & Air, 2008.

The open- and closed-loop configurations in Figure 6 and Figure 7 are very similar, and each of the two configurations is equipped with a 7E.03 gas turbine. The key difference between the two configurations is that the exhaust flow from the HRSG is vented to the atmosphere in the open loop but directed back to the inlet of the compressor through a cooler in the closed loop. The cooler is needed to lower the temperature of the gas leaving the HRSG before entering the compressor. This reduces the compressor shaft power and the temperature of the air leaving the compressor. Both configurations are equipped with water injection systems to ensure that the temperature of the air leaving the compressor does not exceed 300°C, the upper temperature limit for air set by the design of the fluidized bed HX. While being compressed with air, the water droplets absorb the heat from the air and evaporate, thereby reducing air temperature. This wet compression is often used in industry to augment the output of a gas turbine and can effectively reduce compressor power requirements. The water injected into the air is eventually vented to the ambient in the open loop or condensed in the cooler in the closed loop. Basic differences between open and closed loops are as follows:

- Open loop requires continuous injection of demineralized water, whereas closed loop recycles water collected in the condenser.
- Closed loop has slightly lower efficiency because air going into the compressor is about 13°C warmer than ambient air used in the open loop.

2.1.3.2 Net Power Cycle Efficiency

The net efficiency is defined as:

$$\text{Net Efficiency} = \frac{\text{Electricity at Generator} - \text{Auxiliary Power}}{\text{Electricity to Storage}}$$

Figure 8 indicates that the turbine inlet temperature (TIT) of the TES system and ABCC power block needs to be greater than 1,150°C to reach the 52% cycle efficiency target.

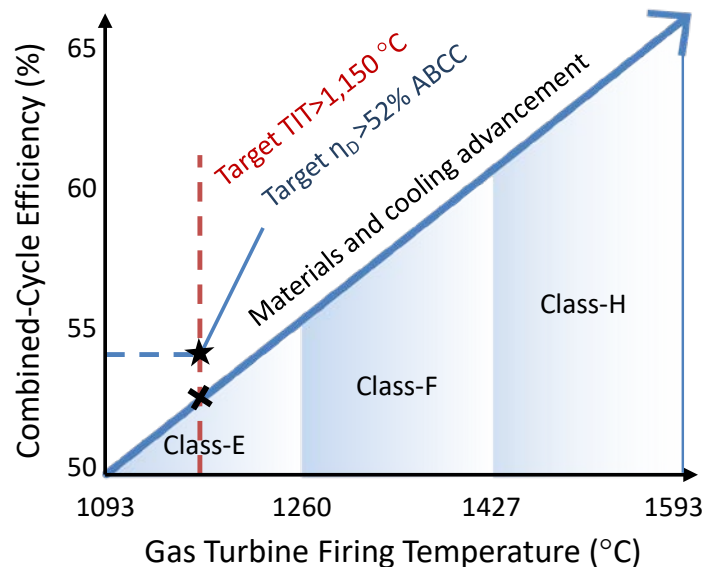


Figure 8. At >1,150°C turbine inlet temperature, the Class-E GTCC can achieve >52% efficiency, and a Class-E turbine was referred for ABCC performance (from reference [6]).

The model described in the previous section simulated a Class-E combined-cycle power block from GE GRC to obtain the state conditions, including air and particle flow rates, air pressure, and temperatures, in order to size the storage components. The performance data for the 7E.03 CC was used to validate the performance models described above. First, the HYSYS model was calibrated against available 7E.03 CC performance data using natural gas as a fuel. Two gas-steam turbine configurations were evaluated: 1:1 (one gas turbine on one steam turbine), 2:1 (two gas turbines on one steam turbine), and 3:1 (three gas turbines on one steam turbine). The 2:1 configuration is slightly more efficient because it is based on a larger steam turbine.

The following boundary conditions were set based on preliminary design of the particle HX:

- The compressor discharge temperature should not exceed 300°C.
- The maximum temperature of the air leaving particle HX is 1,200°C.

Table 4 compares the modeling results with published data.³ Differences between the modeling results and the published data are small and considered acceptable.

Table 4. Comparison Between Published Data and Modeling Results for 7E.03 CC

		Published Data	Modeling Results
1x 7E.03 CC	Net output (MW)	141	142
	Net efficiency	52.0%	52.1%
2x 7E.03 CC	Net output (MW)	283	281
	Net efficiency	52.3%	52.0%

There is no publicly available data for the 3:1 (three gas turbines and one steam turbine) configuration, which has the highest efficiency among the configurations considered. Nonetheless, calibration of the model against the available 1:1 or 2:1 configuration gave the team confidence in the performance of the 3:1 configuration. The 3:1 configuration was eventually recommended for the ENDURING process.

2.1.3.3 Selection of Power Generation Equipment

To determine the conceptual design of the CC used to convert stored heat into electricity, answers to the following questions are needed:

1. What gas turbine is suitable for the application?
2. What steam turbine is suitable for the application?
3. How many gas turbines is the CC equipped with? (1:1, 2:1, or 3:1 configuration)
4. What methods can reduce the compressor discharge temperature (T3) down to 300°C?
5. What are the advantages/disadvantages of the open and closed loops?

Of the GE E, F, and H-class gas turbines⁴, 7E.03, shown in Figure 9, is the most suitable for the proposed concept, mainly because the turbine inlet temperature for this gas turbine (1,260°C) is very close to the desired service temperature of the silica sand (1,200°C).

³ E-Class 7E03 Gas Turbine. GE Power, www.gepower.com.

⁴ <http://www.mcilvaine.com/>. Source: Gas Turbine World.

Table 5. Firing Temperatures of GE Turbines

Class	Firing Temperature, C		Notes
	Low	High	
E	1,093	1,260	Air cooled
F	1,260	1,427	Air cooled
H	1,427	1,593	Steam cooled

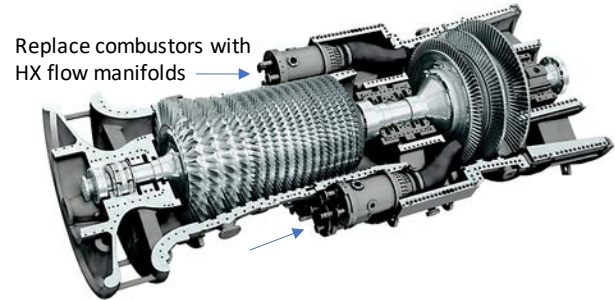


Figure 9. A GE 7E.03 gas turbine with the top casing removed and the retrofit approach.

A 7E.03 gas turbine is ordinarily equipped with combustors to provide heating value to the turbine. Because the proposed concept utilizes stored heat instead of natural gas, it does not require combustors. Instead, it requires manifolds to direct the hot air from the particle HX to the turbine. In the modification, the manifold replaces the 10 combustor cans, as shown in Figure 9. In addition to this replacement, the orifice plates regulating turbine cooling flow may be exchanged with plates that have smaller orifices, because the temperature of the hot air from the particle HX is lower than the temperature of the exhaust gas from the combustor.

The comparison of major GE steam turbine products and the selected steam turbine are based on the power output ranges. A GE STF-A650 reheat steam turbine was chosen as the bottom cycle for the 7E.03 gas turbines because its output range (70–300 MW) is suitable for the combined exhaust gas heat from 2–5 7E.03 gas turbines. The configurations of the modular power systems are the basis of the modeling results in this report. This report focuses on screening ABCC configurations of combining air turbines and a steam turbine for cost and performance of a thermal-power conversion system.

Figure 10 indicates a path for further improving ABCC power conversion efficiency. Additional measures to improve cycle efficiencies, including implementing inlet air cooling using a condenser chiller and increasing turbine inlet temperature to 1,230°C, can potentially achieve 55% ABCC power efficiency, as shown in Figure 10.

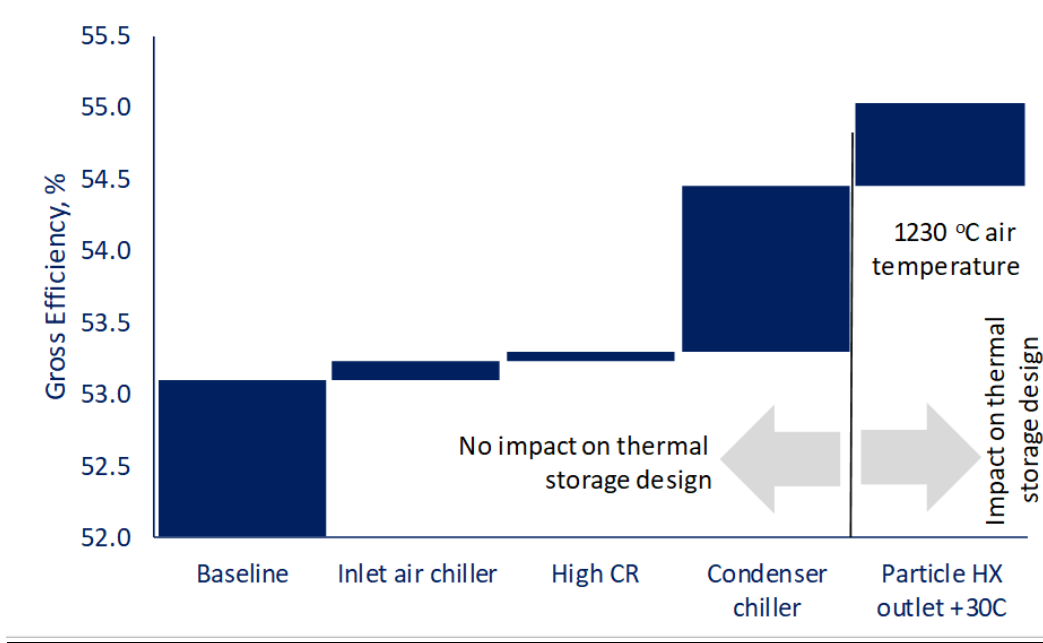


Figure 10. A path for further improving ABCC power efficiency via compressor inlet air cooling and increasing the turbine inlet temperature.

2.1.3.4 Configuration Selection

The first run represents the baseline, and remaining runs represent configurations that were evaluated. Rows 1–10 in Table 6 display the assumed values of key input variables. The simulation results are shown in rows 11 to 41. The nomenclatures displayed in column “Run” are consistent with those displayed in Figure 6 and Figure 7. Note that the net and gross efficiencies in rows 11 and 12 in Table 6 do not account for the storage vessels’ heat losses to the ambient.

Table 6 shows a summary of the modeling runs for different power island configurations. The simulation results for the 3:1 and 1:1 configurations can be found in cases 1 and 5 in Table 6, respectively. The net efficiency for the 3:1 configuration is 0.5 pts higher than that for the 1:1 configuration, mainly due to higher efficiencies of the steam turbine from larger volumetric flow. The 2:1 efficiency (not shown in Table 6) is expected to be lower than 3:1 but higher than 1:1. Because of the advantage in net efficiency, the 3:1 is the preferred configuration and is recommended for the ENDURING system.

Table 6. Simulation Results for Various Plant Configurations and Process Conditions

Row	Run	1	2	3	4	5	6	7	8	9
1	T39, C	1200	1100	1200	1200	1200	1200	1200	1200	1200
2	T3, C	300	300	355	300	300	300	300	250	250
3	Open vs Closed Loop	Open	Open	Open	Closed	Open	Open	closed	Open	Open
4	3x1 vs 1x1	3x1	3x1	3x1	3x1	1x1	3x1	3x1	3x1	3x1
5	Water Injection	Yes	Yes	No	Yes	Yes	No	Yes	Yes	Yes
6	Cmp Pressure Ratio	12.67	12.67	12.67	12.67	12.67	9.4	12.67	12.67	9.4
7	Cmp Inlet Pressure	1.013	1.013	1.013	1.013	1.013	1.013	1.056	1.013	1.013
8	Particle HX Pressure Drop, kPa	43	43	43	43	43	43	43	43	43
9	Cooler Pressure Drop, kPa	1.5	1.5	1.5	1.5	1.5	1.5	1.5	1.5	1.5
10	Comment	17 compressor stages	15 compressor stages	17 compressor stages	17 compressor stages	15 compressor stages				
11	Net Efficiency	0.517	0.492	0.520	0.513	0.512	0.518	0.514	0.511	0.513
12	Gross Efficiency	0.530	0.505	0.534	0.527	0.524	0.533	0.527	0.523	0.527
13	Gross Output, kW	408,405	343,634	374,777	391,361	134,611	396,188	408,233	433,335	426,196
14	Bottoming Cycle Gross Output	139,968	111,426	137,069	137,986	45,132	164,615	143,622	141,679	168,383
15	T_2, C	11.2	11.2	15.0	27.9	11.2	15.0	27.9	11.5	11.2
16	P_2, kPa	100.7	100.7	100.7	100.7	100.7	100.7	105.0	100.7	100.7
17	m_2, kg/s	292.5	292.5	286.1	275.9	292.5	286.1	287.8	295.7	292.5
18	Water Injection, kg/s	3.44E+00	3.44E+00	0.00E+00	4.86E+00	3.44E+00	0.00E+00	5.08E+00	7.17E+00	3.40E+00
19	T_3, C	299.7	299.7	355.0	300.3	299.7	300.2	300.3	249.7	250.0
20	P_3, kPa	1,275.7	1,275.7	1,275.7	1,275.7	1,275.7	937.9	1,329.9	1,275.7	937.9
21	m_3, kg/s	267.4	267.4	261.5	252.1	267.4	261.5	263.1	270.3	267.3
22	T_39, C	1,200.0	1,100.0	1,200.0	1,200.0	1,200.0	1,200.0	1,200.0	1,200.0	1,200.0
23	m_39, kg/s	244.9	244.9	239.6	231.0	244.9	239.6	241.0	247.6	244.9
24	T_41, C	1,128.1	1,035.9	1,132.2	1,128.3	1,128.1	1,128.1	1,128.3	1,124.5	1,124.5
25	P_41, kPa	1,232.7	1,232.7	1,232.7	1,232.7	1,232.7	894.9	1,286.9	1,232.7	894.9
26	m_41, kg/s	267.4	267.4	261.5	252.1	267.4	261.5	263.1	270.3	267.3
27	T_exh, C	512.9	459.3	516.1	519.3	512.9	566.8	518.7	510.4	563.7
28	P_exh, kPa	102.6	102.6	102.6	104.1	102.6	102.6	108.4	102.6	102.6
29	m_exh, kg/s	292.5	292.5	286.1	275.9	292.5	286.1	287.8	295.7	292.5
30	PARTICLE HX duty, kW	256,718	226,783	233,844	247,448	256,718	247,956	257,968	276,291	269,736
31	T_stm Steam Temperature, C	485.1	431.6	488.3	491.5	485.1	539.0	490.9	482.6	536.0
32	T_stack Stack Temperature, C	85.5	89.8	85.2	80.7	85.5	80.4	84.9	85.7	80.7
33	Condenser Temperature, C	29.4	29.4	29.4	29.4	29.4	29.4	29.4	29.4	29.4
34	GT Exhaust Ar Molar Fraction	0.006	0.006	0.007	0.006	0.006	0.007	0.006	0.006	0.006
35	GT Exhaust N2 Molar Fraction	0.781	0.781	0.796	0.753	0.781	0.796	0.754	0.766	0.781
36	GT Exhaust O2 Molar Fraction	0.183	0.183	0.187	0.177	0.183	0.187	0.177	0.180	0.184
37	GT Exhaust CO2 Molar Fraction	0.000	0.000	0.000	0.000	0.000	0.000	0.000	0.000	0.000
38	GT Exhaust H2O Molar Fraction	0.029	0.029	0.010	0.064	0.029	0.010	0.062	0.048	0.028
39	Conensate from cooler, kg/s	-	-	-	4.9	-	-	5.1	-	-
40	Cooler Heat Duty, kW	-	-	-	27,225	-	-	29,683	-	-
41	GT Compression Power, kW	93,671	93,671	99,502	90,327	93,671	82,788	94,187	88,550	78,055

2.1.3.5 Water Injection vs. Reducing Number of Compressor Stages

Water injection and reducing the number of the compressor stages are two options that were investigated for reducing the compressor discharge temperature to below 300°C. When small water droplets are injected into the air entering the compressor, some portion of those droplets evaporates, and this evaporation absorbs heat from the surrounding air, thus reducing the temperature of the air. The remaining water droplets are carried into the compressor, where they continue to absorb heat and evaporate. The evaporation in the compressor further reduces the temperature (T3) of the compressed air leaving the compressor. Thus, water injection is an effective method for reducing T3 down to 300°C or below. Temperature T3 values for runs 1 (water injection) and 3 (no water injection) are 300°C and 355°C, respectively. Run 8 shows that increasing the amount of injected water can further reduce T3 down to 250°C. However, if an excessive amount of water is injected into the inlet of the compressor, liquid water can be carried out of the compressor, where it can damage the particle HX vessel surfaces and storage media. (The damage results from liquid water flashing on hot vessel surfaces or storage media.) Thus, it is critical to examine whether any liquid water is carried out of the compressor. The simulation results indicate that no liquid water is carried out of the compressor for runs 1 and 8.

In addition to the water injection, reducing the number of compressor stages can result in a smaller compressor pressure ratio and in turn lower T3. Run 6 shows that when the number of compressor stages is reduced from 17 to 15, the pressure ratio is reduced from 12.7 to 9.4, resulting in a reduction in T3 from 355°C to 300°C. The stage reduction also results in a slight increase in net efficiency, from 51.7% to 51.8%.

Combining the two methods described above can also be an effective method for reducing T3, as demonstrated in run 9. Combining the two methods provides two advantages over the water injection alone: water consumption and net efficiency. Combining the two methods (run 9) consumes 3.4 kg/s water per each 7E.03, 0.04 kg/s less than the water injection method alone (run 1). However, combining the two methods results in a net efficiency 0.4% lower than the water injection method alone.

Run 1 (water injection) and run 6 (reduced number of compression stages, no water injection) demonstrate the highest net efficiency and are recommended for the ENDURING energy storage system. Run 3 shows the highest net efficiency and thus was chosen as the power cycle configuration.

2.1.3.6 Comparison of Open vs. Closed Loop

In this section, we compared the performance and cost trade-offs of the open- and closed-loop configurations, as shown in Figure 6 and Figure 7. Compared to the open-loop configuration, the closed-loop configuration requires additional components, such as the exhaust gas cooler and the piping connecting the compressor inlet to the HRSG outlet, resulting in higher costs. Runs 1 and 4 in Table 6 show the simulation results for the open- and closed-loop configurations, respectively. The net efficiency for the open loop is 0.4% pts higher than that of the closed loop. The power output for run 1 (open loop) is ~0.44% higher than that of run 4 (closed loop), due to a lower compressor inlet temperature and, in turn, an increased mass flow through the gas turbine compared to run 4. However, the open loop loses 3.44 kg/s of water for each turbine, whereas the closed loop does not lose water, as it can reclaim all the water injected into the inlet of the compressor. The output for run 4 can be increased by pressurizing the air at the inlet of the compressor, as shown in run 7. This technique enables the closed loop to achieve the same power output as that of the open loop (run 1). However, the net efficiency for run 7 is still 0.3 pts lower than that for run 1. Additionally, an HRSG, designed for operation at slightly below atmospheric pressure, requires upgrading the enclosure of the HRSG, which may increase cost significantly.

Table 7 presents a summary of capital and operation & maintenance (O&M) costs for open- and closed-loop configurations. The capital cost of the power island was assumed to be \$650/kW (refer to GTCC power system prices in [18]), and the total equipment costs for the power conversion plant components are the same for the two configurations. The closed loop has the additional cost of the moisture condenser, which was estimated at \$1.9M based on prior GE experience. Variable O&M costs were estimated using data⁵ for NGCC minus costs for Selective Catalytic Reduction (SCR) system (for NO_x emission control) maintenance. The O&M costs were the same for the two configurations, except that open loop has the additional cost of demineralized water injection.

⁵ “Cost of New Entry Estimates for Combustion Turbine and Combined Cycle Plants in PJM.” PJM Interconnection, L.L.C., 2018.

Table 7. Open-/Closed-Loop Cost Comparison Summary

Plant Configuration	Net Output, kW	CAPEX, \$M		Variable O&M		Demineralized Water		
		3GT+ST	Condenser	\$/MWh	\$/k/yr	Kg/s	Cost, \$/ton	\$/k/yr
Open Loop	398,374	259		1.8	6,282	10.3	Variable	Variable
Closed Loop	381,051	259	1.90	1.8	6,282			

2.1.3.7 Large Capacity 3:1 Configuration

Figure 11 shows an exemplary layout of a 3:1 ABCC system. The TES is coupled to each turbine as a modular storage unit, and multiple (one, two, or three) turbines are connected to a single steam turbine. The modular design allows each module to run independently. Thus, each PFB HX and each turbine will run at rated power and can be optimized for one operating condition. The power outputs can be 30%, 60%, or 100% of the rated power for this 3:1 configuration.

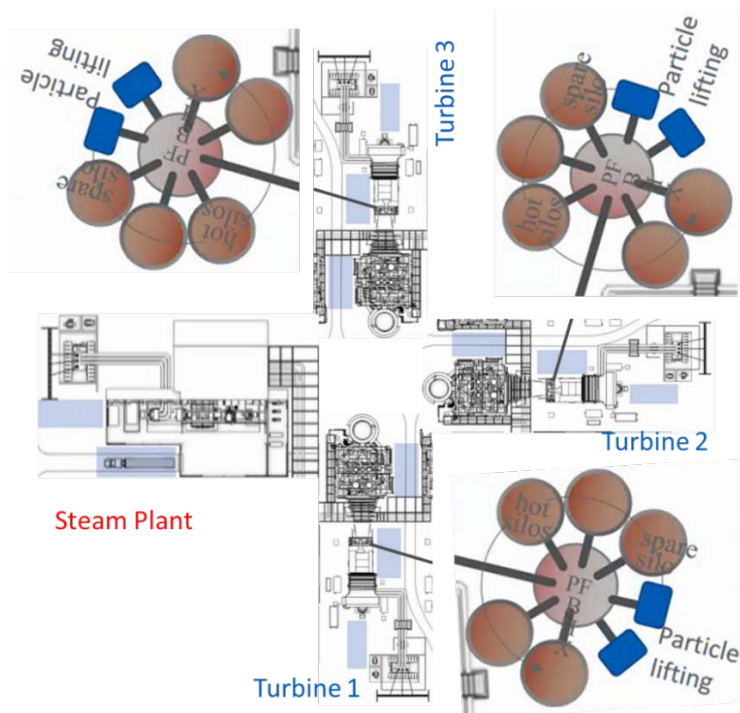


Figure 11. Turbine and storage layout for an assumed 3:1 ABCC plant. Modular PFB HX and TES are coupled to each Brayton turbine. Three Brayton turbines share one steam turbine.

As described in sections 1.3.4, 1.3.5 and 1.3.6, there are three main factors that determine the configuration of the power generation subsystem: (1) the number of 7E.03 gas turbines connected to a steam turbine of type STF-A650; (2) the addition of steam/water injection; and (3) the relative value between the open- and closed-loop configuration. As the number of gas turbines connected to an STF-A650 increases, the cost (\$/kW) for the combined cycle decreases, and the combined cycle efficiency increases. Lowering the cost and increasing the efficiency are supposed to improve the financial value of a combined cycle plant. However, maximizing the number of 7E.03 gas turbines may not always result in the greatest financial benefit, because the power demand also affects the optimal number of 7E.03 gas turbines.

The net efficiency for the 3:1 configuration is 0.5 pts higher than that for the 1:1 configuration (Table 6), mainly due to higher efficiencies for steam turbines (resulting from larger volumetric flow). Because of the advantage in the net efficiency, the 3:1 configuration is preferred over the 1:1 configuration when the power demand is larger than 390 MW.

2.1.4 Key Component Designs and Analysis and System Economics

A modeling tool has been developed to calculate component heat/mass balances, sizing, material needs and basic cost.

2.1.4.1 ENDURING Component Development Approach

Figure 12 shows the media flow stream for assessing the heat/mass balances through the key components. The modeling tool is capable of simulating different system scales, from pilot, precommercial, to commercial units, to evaluate the applicable component sizes and to calculate costs. Components were sized from the operating conditions and their performance was preliminarily evaluated using the modeling tool. The sizing results were used in component design and layout. Details of the system design and costing results provide the TEA inputs in the next step.

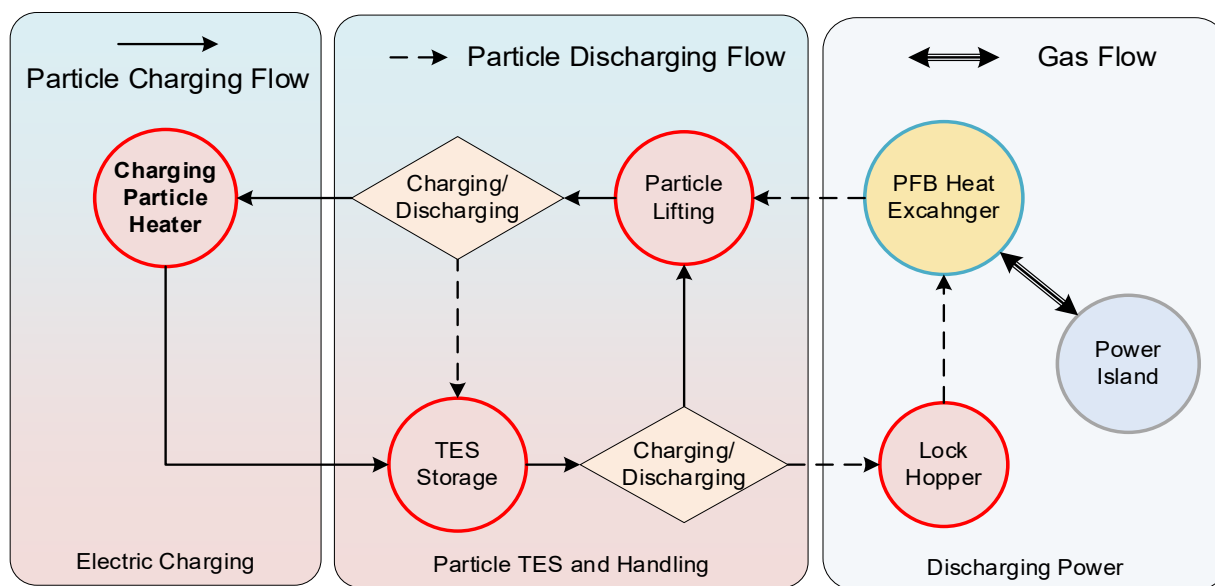
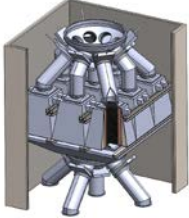
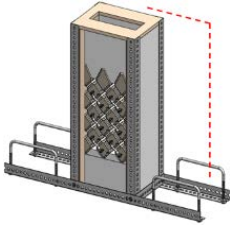
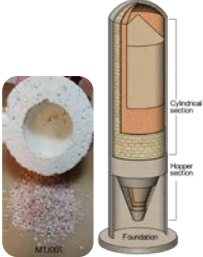
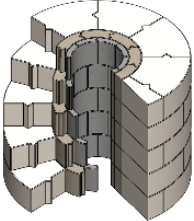


Figure 12. Media flow and heat/mass balance in computation tool.

The baseline plant design specifications are listed in Table 3 and are used to compute component heat/mass balances using the computational tool. Heat/mass balances provide component sizing and state operation conditions in system integration. All components are designed at a commercial scale for cost estimation and are verified by modeling and prototype testing.

Key components were developed on a conceptual level to address these challenges and to assess the design feasibility, manufacturability, and integration within the system. Table 8 lists the design features of three key components (except for the ABCC power cycle) and the approaches for proof of concepts.

Table 8. Key Component Designs and Laboratory Prototypes for the Particle ETES System

Key Components	Proof-of-Concept by Modeling and/or Testing	Design Approach, Working Mechanism, Initial Performance Targets, and Relevant Industry Practices
<p>Heater</p> 	<p>Heater prototype</p> 	<p>Resistive heating wires wrapped around refractory bars form the heating elements to heat particles to 1,200°C using electricity.</p> <p>Modular design with each module running at a fixed particle flow rate for optimum particle heat transfer and constant power in on/off mode.</p> <p>Nine heater modules can support nine charging load levels.</p>
<p>Particles/storage</p> 	<p>Storage bin prototype</p> 	<p>Low-cost storage using silica sand (\$30–\$40/ton) with particle stability verified at 1,200°C.</p> <p>Charging and discharging temperatures range from 300°C to 1,200°C.</p> <p>Concrete silo with internal insulation using low-cost refractory materials with conventional construction methods.</p> <p>Tests proved material compatibility at operating temperature.</p>
<p>Heat exchanger</p> 	<p>Cold/hot prototypes</p> 	<p>Direct contact between compressed air and hot particles inside the PFB HX eliminates the heat transfer interfaces in a conventional heat exchanger; thus, it can achieve high temperatures without expensive materials for the heat transfer surfaces to improve performance.</p> <p>Industry PFB HX design, engineering, and fabrication for a PFB boiler can be leveraged.</p>

The designed ENDURING plant is a modular system that consists of thermal energy storage (TES)-specific components and power-specific components. The TES-specific components include particle containment silos and particle lifting skip hoists. These two components are directly associated only with particle handling. The power-specific components include not only power islands, but also components associated with energy and mass transfer. Newly designed power-specific components include the gas pipeline, PFB system (including the pressure vessel), PFB heat exchanger, gas distributor, particle separation cyclones, lock hopper, and particle heater. In this analysis, the material costs, as well as the costs of component construction labor, were assumed to estimate the bare-bones cost to fabricate the ENDURING system. The engineering costs, procurement costs and fees, contingency costs, and other case- and/or site-specific costs are not included in the cost analysis presented in this report. Cost analysis shows that the ENDURING technology has the potential to achieve a levelized cost of storage (LCOS) of \$0.05/kWh-cycle for 100-hr duration via several pathways.

Laboratory prototypes have been built to verify the component operation and/or validate the modeling methods. The validated models are then used to gauge commercial-scale performance. The conceptual designs, prototype development, and testing validated the component modeling

approaches, fabrication processes, and operation mechanisms. The key components listed in Table 8 for the ABCC power generation system are described individually in the subsequent sections. The following sections describe Tasks 2, 3, and 4 and provide details of laboratory prototypes or modeling analysis for verification of component designs and operation. Task 1 performed cost analysis based on mechanical designs and material usage by estimating a cost factor to evaluate the capital cost of the storage system.

2.1.4.2 ENDURING System Component Specification and Cost Estimation

(Note: Work contributed by Xingchao Wang of Colorado School of Mines.)

The capital cost of a power generation system often includes equipment, facilities, and infrastructure to support the plant, as well as construction and/or installation labor costs. However, this project for system and component development only referred to the bare erected cost (BEC) of components, based on the National Energy Technology Laboratory (NETL) cost estimation methodology for power plants (shown in Figure 13), or the instant cost as introduced in a report published by the California Energy Commission (CEC) [7], [8]. This cost analysis did not consider facilities or infrastructures such as land, buildings, substation, project finance, contingencies and engineering cost, etc. BEC estimation as shown in Figure 13 focuses only on the cost of component material usage and manufacturing.

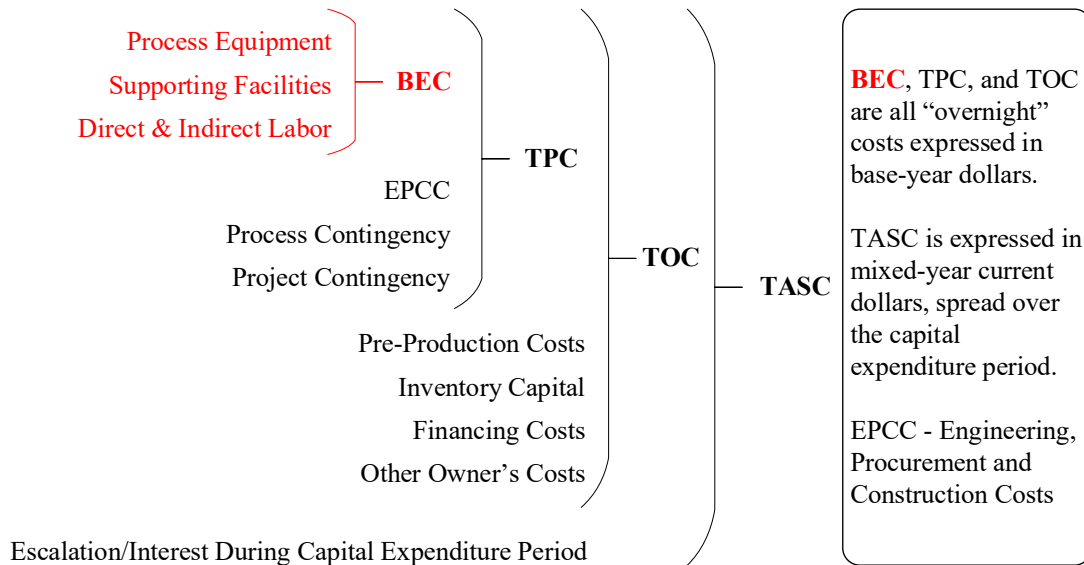


Figure 13. Capital cost levels defined by NETL.

By leveraging existing manufacturing methods for electric heaters, storage silo insulation, refractory insulation, and PFB HXs, some components of the modular ENDURING system can be built in a factory and brought on-site for easy construction. Most components are likely manufactured in the U.S., and it is feasible and cost effective to build an ENDURING plant on a retired thermal power plant after component development and demonstration. In contrast, constructing a new power plant—such as a coal-fired power plant or a nuclear power plant, is usually expensive and involves a significant amount of on-site construction work.

The cost estimation of an ENDURING plant can be performed component by component due to its modular nature. An ENDURING plant cost can be divided into two categories: energy storage-specific components and electric power-specific components.

2.1.4.3 Energy Storage -Specific Components

For energy storage-specific TES components, the unitized capital cost is used to evaluate the cost-effectiveness, which can be written as:

$$c_{i, TES} = \frac{C_{i, TES} \times N_i}{Q_{TES}} \quad (1)$$

where $c_{i, TES}$ is the TES-specific component i unitized capital cost, \$/kWh_{th}
 $C_{i, TES}$ is the TES-specific component i single unit construction cost, \$
 N_i is the number of TES-specific units needed in the system
 Q_{TES} is the total TES capacity, kWh_{th}

Therefore, the overall unitized capital cost c_E relevant to energy storage-specific TES components can be expressed as:

$$c_E = \sum_i c_{i, TES} \quad (2)$$

where $c_{i, TES}$ consists of two major components: particle containment and particle lifting.

Particle Containment

Following the previous design efforts, the silo geometry, the silo structure and foundation, and the insulation design are determined [4,9]. The resulting key design specification values of a TES design in this report are shown in Table 9. The required amount of construction and insulation materials can be calculated based on the designed geometries of the silo and the foundation.

The containment silo construction cost can be divided into three parts: silo, foundation, and insulation. Each category includes both material and labor costs, which can be expressed as:

$$\begin{aligned} C_{containment, tot} &= C_{containment} + C_{particle} \\ &= (C_{silo, tot} + C_{foundation, tot} + C_{insulation, tot}) + C_{particle} \end{aligned} \quad (3)$$

As described in Table 9, the single containment silo construction cost, including the storage media cost, is approximately \$12,500,000 for a single unit with a storage capacity of 6.4-GWh_t. For the base case 405-MW_e ENDURING plant, 12 units of containment silos are required, resulting in a total unitized capital cost of \$2/kWh_{th}, including the skip hoister (see Table 10).

Note that highest-cost item in the TES containment is the insulation, which has not been optimized for design and installation. To achieve the thermal loss goal of 3% for 5-day duration, current modeling is based on a monolithic insulation block, which uses a large amount of

materials with high installation cost. Future optimization work with thermal-mechanical analysis may reduce material and installation costs by recasting refractory blocks with inner voids filled with ceramic fibers that can reduce material use but increase the thermal resistance. Further cost reduction in TES may be achievable with design iterations.

Table 9. Particle Containment Silo Design Specifications and Cost Estimation

Particle Storage Containment Silo				
	Items	Units	Values	
	Design Specifications			
	Whole System Silo # Required	-		12
	Single Silo Capacity	ton		22500
	Silo Height (Cylinder Section Only)	m		65.8
	Silo Outer Diameter	m		20
	Silo Inner Diameter	m		17.0
	Insul. L1 - Thickness - Concrete	m		0.3
	Insul. L2 - Thickness - CaSi	m		0.7
	Insul. L3 - Thickness - P550	m		0.4
	Insul. L4 - Thickness - P700	m		0.1
	Thermal Energy Storage Capacity	GWht		6.4 X 12
	Categories		Units	Cost Values
Single Unit Cost				
Single Containment Silo Capital Cost		\$	12,503,325	
Single Silo Containment Construction Cost		\$	11,731,455	
Silo and Foundation Construction		\$	3,857,262	
Insulation Cost		\$	7,874,193	
Single Silo Storage Media Cost		\$	771,870	
Gross Capital Costs (12 Units)				
Whole System Containment Silo Total Cost		\$	150,039,896	
Unitized Capital Costs				
Containment Silo Cost per Unit TE Stored		\$/kWh_th	1.96	

Particle Lifting Skip Hoist

The major components of a skip hoist system, including a motor, a drum brake, two hoist drums, two skips, wire rope, and two pulleys, are shown in Table 10. The skip hoist is a mature industry product that is also highly modular. Therefore, the bare bones skip hoist purchased equipment cost is:

$$C_{skip_hoist, equip} = C_{motor} + C_{drum_brake} + C_{drum} + C_{skip} + C_{wire_rope} + C_{pulley} \quad (4)$$

The equipment cost breakdown is based on a previous study conducted by Georgia Institute of Technology [10]. Considering installation labor, material, and accessory cost factors, the capital cost of a skip hoist can be estimated as follows:

$$C_{skip_hoist,tot} = C_{skip_hoist,equip} \times (1 + F_{installation} + F_{parts\&accessories}) \quad (5)$$

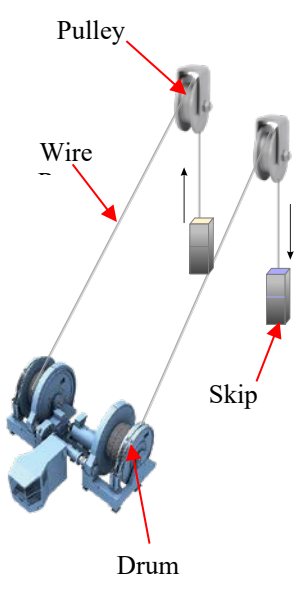
where $C_{skip_hoist,tot}$ is the single skip hoist capital cost, \$

$F_{installation}$ is the installation factor

$F_{parts\&accessories}$ is the parts and accessories factor

The unitized capital cost of \$0.042/kWh_{th} for the entire skip hoist system can be then obtained.

Table 10. Particle Lifting Skip Hoist Design Specifications and Cost Estimation of Key Parts Excluding Supporting Structure and Motor Power Control

Particle Lifting Skip Hoist				
	Items	Units	Values	
	Design Specifications			
	Lifting Distance	m	125	
	Skip Lifting Trip Time	s	84.1	
	Time Discharge to Heater	s	84.1	
	Particle Load per Skip	kg	25248	
	Power Consumption at Required Particle Flow Rate	kW	482	
	Rated Motor Size	kW	1300	
	Overall Lifting Efficiency	%	78.8	
	Lifting Capacity	kg/s		
Categories		Units	Cost Values	
Key Component Equipment Cost				
Skip Hoist Equipment Cost	\$	613,913		
Single Unit Capital Cost				
Single Skip Hoist Capital Cost	\$	1,074,348		
Gross Capital Costs (3 Units)				
Whole-System Skip Hoist Capital Cost	\$	3,223,044		
Unitized Capital Costs				
Skip Host Cost per Unit TE Stored	\$/kWh _{th}	0.042		

2.1.4.4 Electric Power-Specific Components

Electric power-specific components provide bidirectional connection with the grid for charging and discharging electricity. They include the electric charge particle heater, discharge PFB HX and lock hopper, and power generation unit, which were designed as a storage module as shown in Figure 1. The installed capital costs for the modular power-specific components are derived

from the material costs of each component, considering necessary factors, such as fabrication, installation, and/or necessary material and accessory costs. The correlation of power-specific component cost estimation can be written as:

$$C_{j,PowerSpecific} = \frac{C_{j,PowerSpecific_materials}}{R_{fabrication}} \times (1 + F_{installation} + F_{materials\&accessories}) \quad (6)$$

where $C_{j,PowerSpecific}$ is the power-specific component j installed capital cost, \$

$C_{j,PowerSpecific_materials}$ is the power-specific component j fabrication and insulation material cost, \$

$R_{fabrication}$ is the fabrication material to purchased equipment cost ratio

$F_{installation}$ is the purchased equipment installation factor

$F_{materials\&accessories}$ is the materials and accessories factor

The cost factors for different power-specific components of the ENDURING plant are listed in Table 11.

Table 11. Cost Factors of Power-Specific Components

Items	Cost Factors		
	$R_{fabrication}$	$F_{installation}$ [11]	$F_{materials\&accessories}$ [11]
Air Pipeline	0.5 *	0.45	-
PFB Pressure Vessel	0.52 [12]	0.45	-
PFB HX	0.741 [13]	0.45	-
Cyclone	0.5 *	0.45	-
Lock Hopper	0.52 [12]	0.45	-
Electric Charging Heater	0.5 *	0.45	0.30

* Assumed. Typical Value.

The unitized capital cost of power-specific components of the ENDURING system can be expressed as:

$$C_{j,PowerSpecific} = \frac{C_{j,PowerSpecific} \times N_j}{W} \quad (7)$$

where $C_{j,PowerSpecific}$ is the power-specific component i unitized capital cost, \$/kW_e

$C_{j,PowerSpecific}$ is the power-specific component i single unit capital cost, \$

N_j is the number of power-specific units needed in the system

W is the total power generation capacity, kW_e

Accordingly, the total unitized capital cost of the power specific components, $c_{PowerSpecific}$ can be calculated as follows:

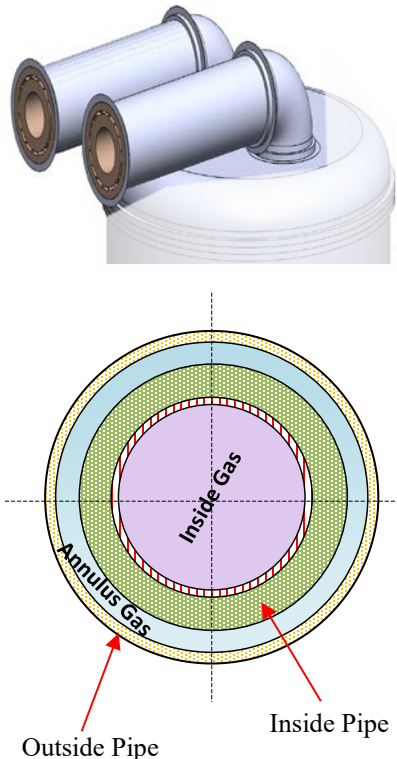
$$c_{PowerSpecific} = \sum_j c_{j,PowerSpecific} \quad (8)$$

where $c_{j,PowerSpecific}$ is the cost of power-specific equipment, including an electric charge particle heater, PFB HX, and auxiliary equipment, such as connecting air pipelines, and ABCC power generation system. Operating conditions were used in computing their pressure shell designs and insulation needs.

Air Pipelines

The pipe dimensions and insulation layers are designed to meet the pressure drop as well as the heat loss requirement. The unit purchased cost of the gas pipeline is \$15,539/m for the base case. The pipe-in-pipe design consists of an inner pipe for the hot gas at 1,200°C and an outer pipe for the cool gas at 300°C. The inner pipe will be fabricated with insulation materials provided by our partner, Allied Minerals, which are capable of working at the designed temperatures. The structure steel and fabrication used in the outer pipe/inner shell complies with the American Society of Mechanical Engineers (ASME) Boiler & Pressure Vessel (BPV) Section VIII Division 1, as the thickness of 0.034 m (shown in **Table 12**) is able to bear the operating pressure of 1.276 MPa [14]. Therefore, the cost of the fabrication and insulation materials for gas pipelines can be calculated based on the designed dimensions in **Table 12**. Subsequently, the capital cost of gas pipelines for the whole system can be calculated using Equation (1) and the cost factors in Table 11.

Table 12. Air Pipeline Design Specifications and Cost Estimation

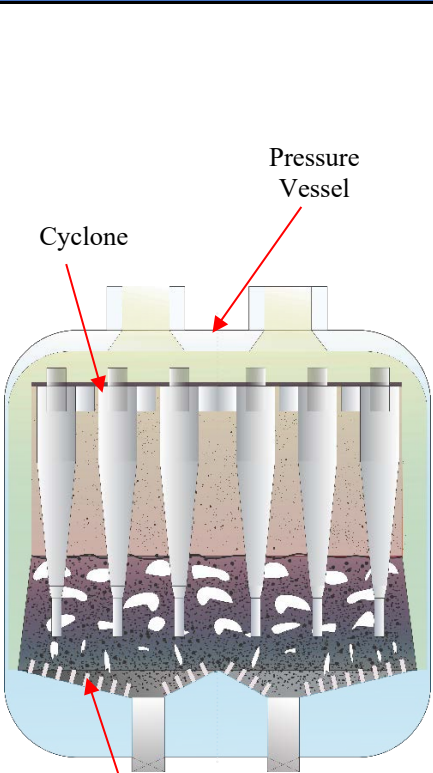
Gas Pipeline Cost				
	Items	Units	Values	
		Design Specifications		
Gas Pipeline Outer Pipe ID		m	2.85	
Gas Pipeline Outer Pipe OD		m	3.08	
Gas Pipeline Inner Pipe ID		m	1.65	
Gas Pipeline Inner Pipe OD		m	2.60	
Inner Insul. L1 - Thickness - GUNCAST		m	0.165	
Inner Insul. L2 - Thickness - INSUMIX		m	0.300	
Inner Insul. L3 - Thickness - A36 Structure Steel		m	0.008	
Outer Insul. L1 - Thickness - A36 Structure Steel		m	0.034	
Outer Insul. L2 - Thickness - Mineral Wool		m	0.100	
Outer Insul. L3 - Thickness - A36 Structure Steel		m	0.008	
Pipe # in Pipe Bundle		-	2	
Pipe Length		m	15	
Total Pressure Drop		kPa	4.04	
Categories		Units	Cost Values	
Purchased Cost				
Gas Pipeline Purchased Cost			\$/m	15,539
Single Unit Cost				
Single Unit Gas Pipeline Capital Cost	\$		675,932	
Gross Capital Costs (3 Units)				
Whole-System Gas Pipeline Capital Cost	\$		2,027,797	
Unitized Capital Costs				
Piping Cost per Unit Power Capacity	\$/kW		5.01	

PFB Heat Exchanger

Table 13 shows the PFB HX design specifications and cost estimation. The cost of a PFB HX consists of the PFB pressure vessel (PFBPV) cost, PFB inner bed cost, and particle separation cyclone cost:

$$C_{PFBHX, equip} = C_{PFBPV, equip} + C_{InnerBed, equip} + C_{cyclone, equip} \quad (9)$$

Table 13. Design Specifications and Cost Estimation

PFB System Cost				
 <p>The diagram shows a cross-section of a Pressure Vessel containing a distributor at the bottom, a PFBHX (PFB Heat Exchanger) in the middle, and three cyclones at the top. Labels with arrows point to the Cyclone, Pressure Vessel, and Distributor.</p>	Items	Units	Values	
	Design Specifications			
	PFBPV			
	PFB Dimensions	m	15.00	
	PFB Pressure Vessel OD	m	15.53	
	PFBHX			
	Dense Region ID	m	13.00	
	Freeboard Region ID	m	14.00	
	Dense Region Height	m	4.00	
	Freeboard Region Height	m	6.00	
	PFB HX OD	m	14.70	
	Minimum Fluidization Velocity, U_{mf}	m/s	0.204	
	Particle Separation Cyclone			
	Cyclone Separation Efficiency	%	99.98	
	Cyclone Pressure Drop	kPa	2.82	
	Cut Diameter, d_{50}	μm	8.71	
	PFB System Pressure Drop	kPa	38.91	
	Categories		Units	Cost Values
	Costs of Major Parts			
	PFBPV Equipment Cost	\$	2,071,334	
PFBHX Equipment Cost (including distributor, baffles, insulations and other accessories)	\$	4,574,561		
Particle Separation Cyclone Equipment Cost	\$	57,124		
Single PFB HX Capital Cost	\$	9,719,377		
Gross Capital Cost (3 Units)				
Entire PFB HX System Capital Cost	\$	29,158,132		
PFB Capital Cost of Unit Power Capacity	\$/kWe	72.00		

The PFB inner bed costs are taken from a 1977 DOE project that used PFB as a combustor to generate hot gas to drive a turbine [13,15]. This PFB combustor was 8.53 m in OD \times 23.16 m in height. Equation (10) can be used to scale this to the size of the current design by volume:

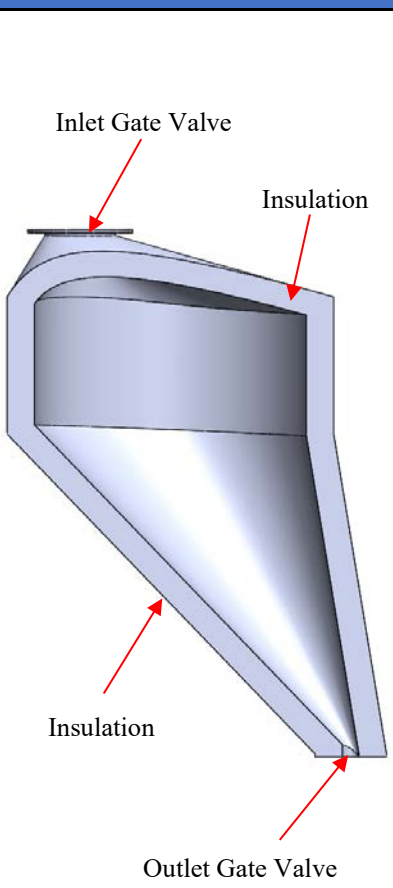
$$\frac{C_1}{C_2} = \left(\frac{V_1}{V_2}\right)^{0.6} \quad (10)$$

Here, C refers to the equipment cost and V is the equipment volume [16]. In this report, the basic cost scale factor of a conventional “0.6” value is employed. The Conversion Factor of Chemical Engineering Plant Index (CEPCI) cost conversion technique was also used to convert the PFB HX cost to the year of 2019 dollars. Accordingly, the PFB system capital cost is calculated as \$72/kW. The particle separation cyclone costs were estimated based on the fabrication material costs provided by Allied Minerals.

Particle Dispense Lock Hopper

Lock hoppers are used to balance the air pressure between particles dispensed from the TES to the PFB HX. The lock hoppers fill with particles and are then pressured to equalize the pressure for particles flowing into the PFB HX. Table 14 shows the particle dispensing lock hopper design parameters and a cost estimation of the lock hopper.

Table 14. Design Specifications and Cost Estimation

Lock Hopper Cost				
	Items	Units	Values	
	Design Specifications			
	Lock Hopper Design Height	m	10.00	
	Lock Hopper ID	m	8.63	
	Lock Hopper OD	m	9.65	
	Lock Hopper Inlet Diameter	m	0.80	
	Lock Hopper Outlet Diameter	m	0.57	
	Particle Load per Lock Hopper	kg	293976	
	Lock Hopper Volume	m ³	313	
	Charging Time of Single Lock Hopper	s	201	
	Discharging Time of Single Lock Hopper	s	462	
	Lock Hopper Unit Height	m	13.00	
	Insul. L1 - P700 - Thickness	m	0.20	
	Insul. L2 - Mineral Wool - Thickness	m	0.25	
	Insul. L3 - A36 Steel - Thickness	m	0.06	
	Categories		Units	Cost Values
	Equipment Costs			
	Single Lock Hopper Equipment Cost	\$	221,607	
	Top Gate Valve Equipment Cost	\$	15,652	
	Bottom Gate Valve Equipment Cost	\$	10,743	
Single Unit Capital Cost				
Single Lock Hopper Capital Cost	\$	359,602		
Gross Capital Cost (24 Units)				
Whole-System Lock Hopper Capital Cost	\$	8,630,459		
Unitized Capital Cost				
Lock Hopper Cost per Unit Power Capacity	\$/kW	21.31		

The lock hopper equipment costs include the inlet and outlet gate valves and the lock hopper body:

$$C_{lock_hopper, equip} = C_{gatevalve_inlet} + C_{gatevalve_outlet} + C_{lock_hopper, body} \quad (11)$$

The lock hopper body is basically a pressure vessel with necessary insulation measures. The insulation layers and the thicknesses were calculated for adequate thermal performance and mechanical strength. The gate valve costs were extrapolated from the IndustrialMartUSA.com cost database using Equation (12), based on the designed diameter of the gate valves [17]:

$$C_{gatevalve} = 550.86D_{gatevalve} - 1698 \quad (12)$$

where $C_{gatevalve}$ is the gate valve equipment cost, \$

$D_{gatevalve}$ is the dimension of gate valve, inches.

For the base-case system, 24 lock hoppers are required resulting in a total capital cost of \$21.31/kW. Similar to the air pipeline, pressure vessel designs for both PFB HX and lock hoppers were designed according to ASME BPV Section VIII Division 1 to calculate the shell wall thickness [14]. However, AISI 4340 steel, with its relatively high yield strength of 450 MPa at 300°C, is selected to fabricate the inner shell to reduce the amount of material used and the net weight of the PFBPV. In addition, mineral wool and A36 structure steel are placed outside of the inner vessel to provide the required insulation capability.

Electric Particle Charging Heater

Table 15 shows the detailed heater dimensions, structure, and insulation designs. The electric charging heater is a modular design for flexible maintenance and load control.

Table 15. Design Specifications and Cost Estimation

Particle Heater Cost				
	Items	Units	Values	
	Design Specifications			
		Total Heating Wire Length for one Unit	m	133720
		Heating Element # of Single Heater Unit	-	8613
		Entire Heater Height	m	18
		Heater Unit Inlet Diameter (Circle)	m	3
		Insul. L1 - P550 - Volume	m ³	19
		Insul. L2 - CaSi - Volume	m ³	22
		Insul. L3 - A36 Steel - Volume	m ³	1
		Single Heater Unit Capacity	MW	316
	Categories		Units	Cost Values
	Single Unit Equipment Cost			
		Single Heater Unit Equipment Cost	\$	1,316,688
	Single Unit Capital Cost			
		Single Heater Unit Capital Cost	\$	2,304,205
Gross Capital Cost (Three Units)				
	Whole-System Heater Capital Cost	\$	6,912,614	
Unitized Capital Costs				
	Heater Cost of Unit Power Capacity	\$/kW	7.3	

The particle heater is designed in a modular configuration with nine heater units. The heater load control is designed by on/off switching of each heater unit. Each heater unit is equipped with nine identical heater modules. The material cost of the particle heater consists of three major parts:

$$C_{heater_materials} = C_{heating_wire} + C_{heating_element_refactory} + C_{insulation} \quad (13)$$

The electric heater cost of \$7.3/kW accounts for the material and fabrication estimation. The cost of the power supply and control devices cannot be defined in the current stage without a system integration and configuration and would be resolved in future scale-up efforts.

Power Generation System

Figure 14 illustrates a conventional gas turbine combined cycle plant layout. An ENDURING plant uses a modular Brayton combined-cycle system adapted from a natural gas combined cycle (NGCC) system. Most of the components in an NGCC are identical to those in a newly constructed ENDURING ABCC power system, excluding natural gas combustion process related parts. In addition, NGCC plants are a mature technology and are widely used, with an extensive amount of cost information available. Accordingly, the cost estimation in this report for the ENDURING ABCC power unit is based on reported NGCC plant costs.

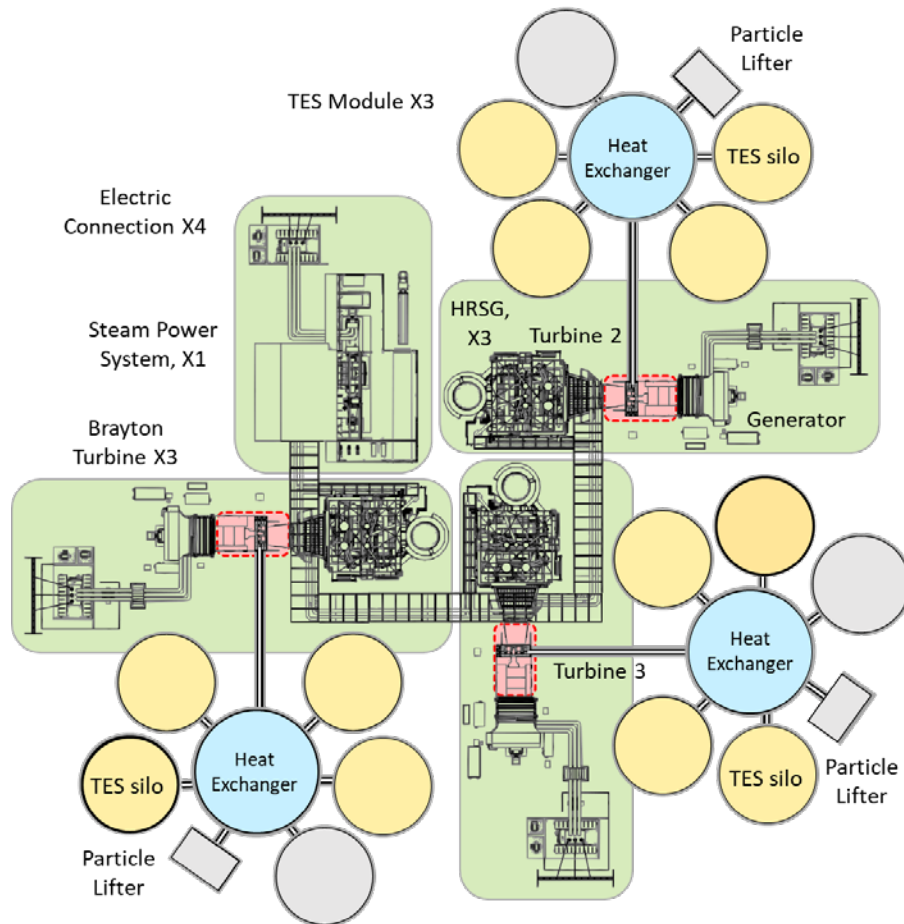


Figure 14. Power system layout and ENDURING plant schematic.

An extensively cited data source, the Gas Turbine World (GTW) Gas Turbine Handbook, was used as the baseline to conduct a literature survey to obtain the BEC of essential components of NGCC plants. The total BEC of NGCC plants is broken down into six sections, including gas turbine, heat recovery steam generator (HRSG), steam turbine, cooling system, generator with electric plant, balance of plant, miscellaneous, and control sector.

As Figure 15 indicates, the NGCC overnight capital costs published in different sources fall well into the cost range provided by GTW with an accuracy of $\pm 15\%$ [18]. Based on all these validated data, we performed a cost breakdown of NGCC plants, which is presented in Figure 16 with the average values as well as the standard deviations of each essential section [7, 18–22]. Note that the effect of plant capacity on the cost breakdown is relatively small within the range of 400–800 MW_e . In addition, a combined cycle plant capacity is typically larger than 400 MW_e . CEPCI is then employed to convert the cost in the present time period. The cost conversion can be defined as [24]:

$$C_{i,B} = C_{i,A} \times F_{CEPCI,A to B} \quad (14)$$

where $C_{i,A}$ is the component cost at year A

$C_{i,B}$ is the component cost at year B

$F_{CEPCI,A to B} = CEPCI \text{ at year B} / CEPCI \text{ at Year A}$ is the chemical engineering plant index factor.

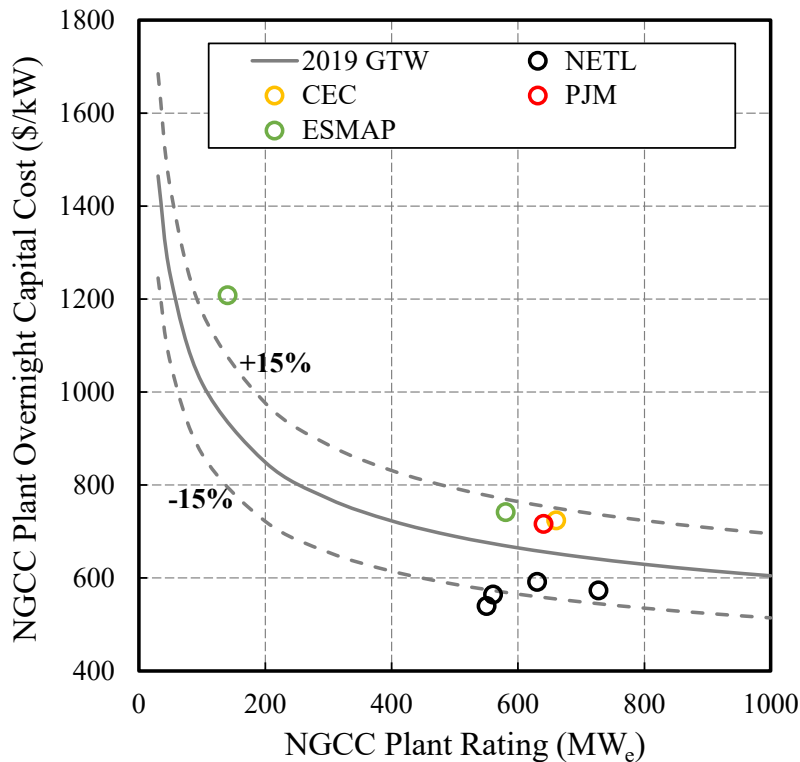


Figure 15. Published NGCC BEC data.

The data source and the breakdown cost for each power system component can be found in the next section.

Breakdown of Power System Cost

Based on the cost breakdown of essential components, cost estimates of three different ENDURING plant implementation scenarios can be obtained as follows. First, the power generation system cost, $c_{PowerSys}$, can be obtained. Considering the power-specific component cost, $c_{PowerSpecific}$, the overall power generation unitized cost, c_P , will be:

$$c_P = c_{PowerSpecific} + c_{PowerSys} \quad (15)$$

Figure 16 shows the cost breakdown of essential components or items in a conventional combined cycle gas plant by referring to [9], [12–16]. The cost breakdown was used to assess the cost of a newly built plant and facilitates the estimation of cost reduction by leveraging infrastructure from a repurposed thermal power plant using gas turbine or Rankine steam power generation. The BEC cost of the bare bones components for power generation is around \$535/kW on average. In addition to the power generation components, the total ENDURING power system cost also includes the charging electric heater (\$7.3/kW, plus electric supply) and the discharging fluidized bed (\$72/kW) with lock hoppers (\$22/kW). Thus, the BEC cost of basic power equipment is estimated to be about \$650/kW excluding the cost of land, building, grid-connection infrastructure, and engineering, procurement, and construction that are not in the scope of this cost estimation.

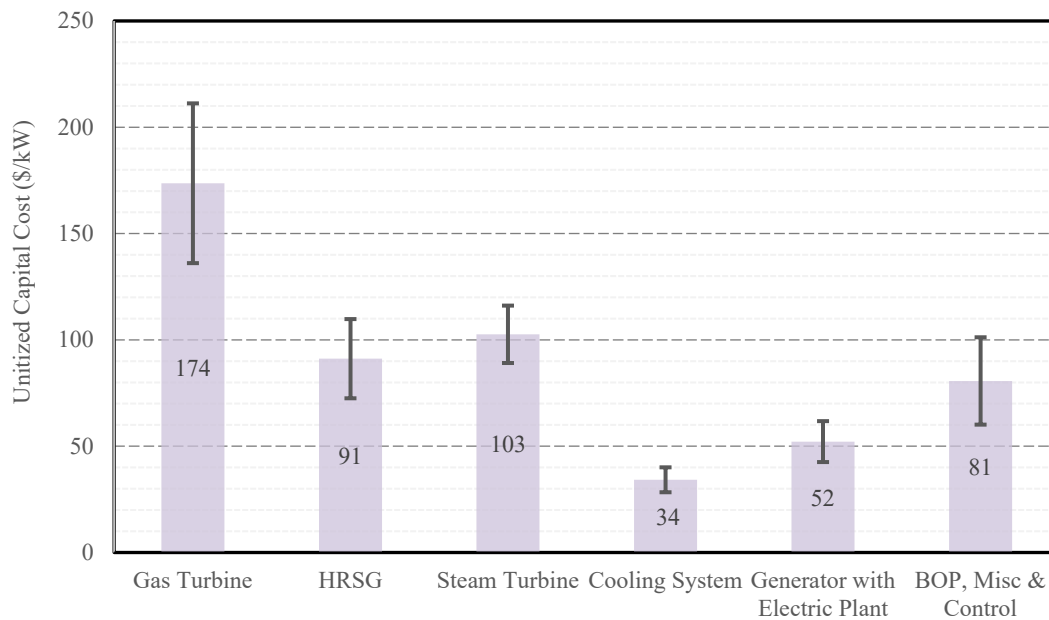


Figure 16. Cost breakdown of essential components or sectors in a conventional combined cycle gas plant.

SCR and natural gas pipeline costs were deducted from the cost breakdown analysis and the results of the GTCC power system presented in Figure 16. The BEC percentages of different

sections can be found in Figure 17. Gas turbine and HRSG costs make up 50% of the total gas turbine combined cycle power generation system costs. The cost breakdown indicates the major capital investment in an energy storage plant is the power generation equipment, which is a motivation to leverage existing thermal-power plants to minimize the capital investment. Thereby, three types ENDURING LDES plant designs were considered including a new-built TES facility, retrofitting a GTCC plant, and modifying a retiring coal-fired power plant to leverage their power generation components.

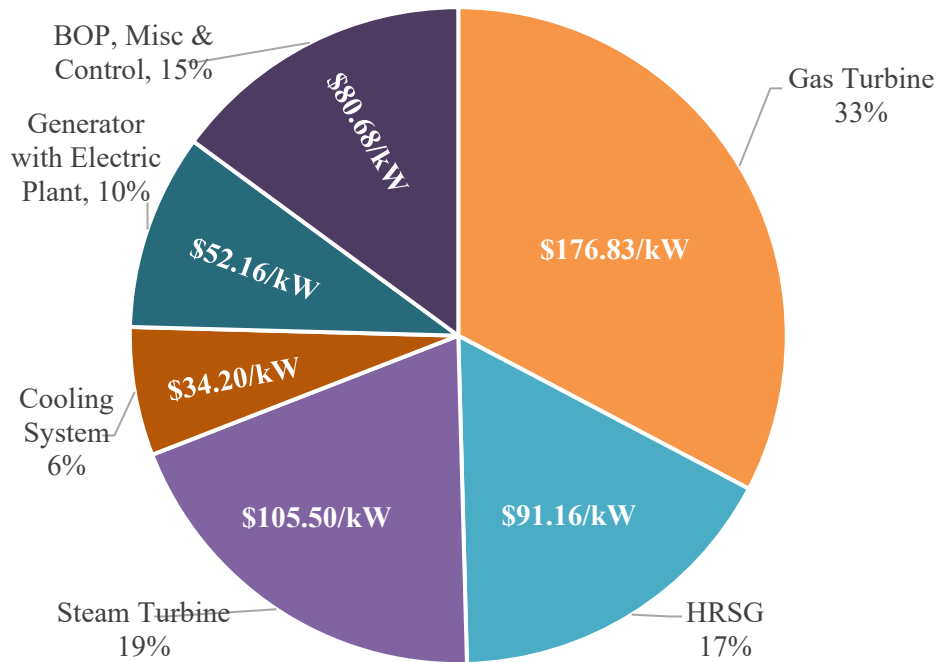


Figure 17. Average cost breakdown percentages of essential components or sectors in a conventional combined cycle gas plant.

New-Built ABCC Power System

The first design scenario is a newly built ABCC power generation system. Every major component will be newly constructed. Each component will be identical to that of an NGCC plant, except for a modified gas turbine and other new-built ENDURING power-specific components. The gas turbine of the ENDURING ABCC plant will be modified from the GE 7E.03 gas turbine after removing the combustor and replacing it with an air flow manifold.

As Figure 18 shows, the compressed air coming from the compressor will be led into a PFB HX through gas pipelines to transfer heat from the hot particles to compressed air. Then, the heated air (at 1,200°C) will pass through a turbine expander to generate electricity. Subsequently, the exhausted hot air will be led into a HRSG to recover heat in a bottom steam cycle. Therefore, the overall new construction ENDURING ABCC power system cost can be expressed with the breakdown costs of:

$$C_{PowerSys,GTCC} = C_{turbine} + C_{HRSG} + C_{steam_turbine} + C_{cooling} + C_{Generator,electric} + C_{BOP\&control} \quad (16)$$

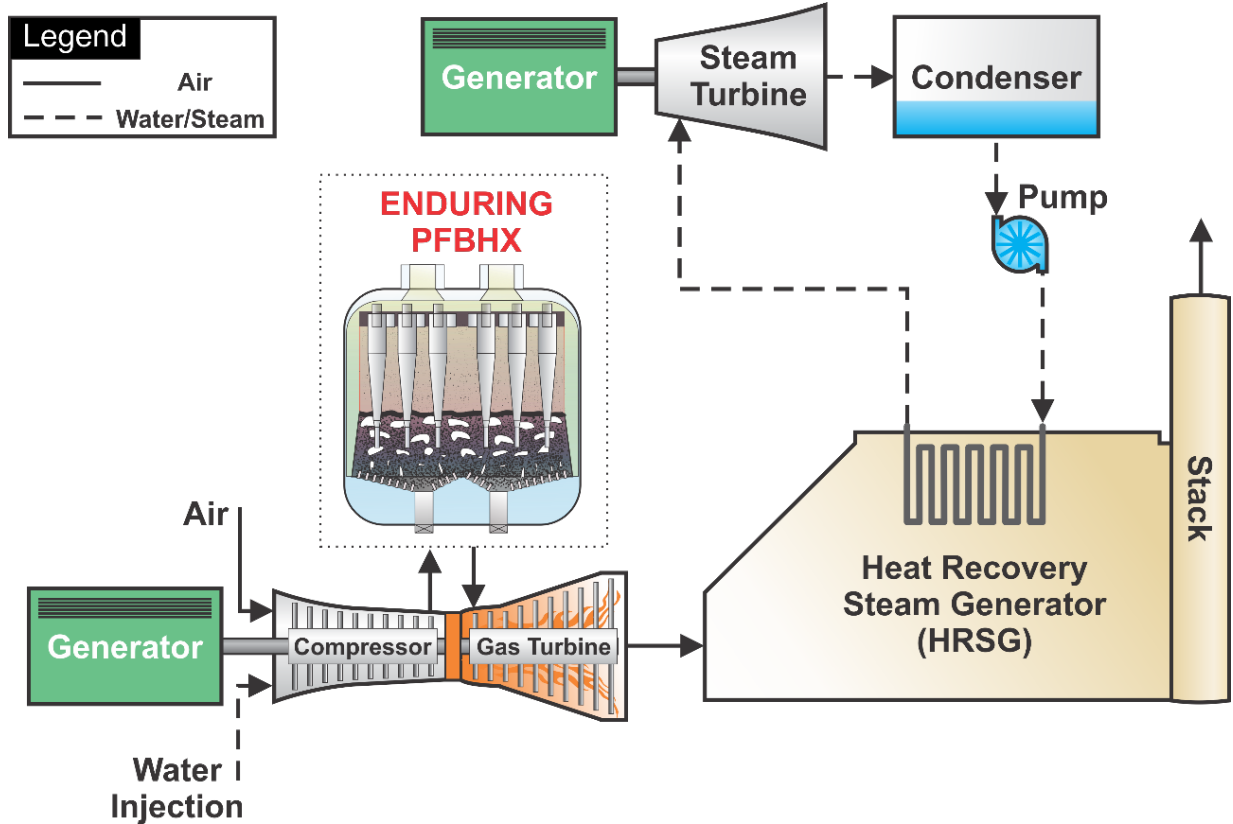


Figure 18. New construction ENDURING ABCC power plant layout.

Retrofitted NGCC Plant

The second scenario is retrofitting a retired NGCC plant. Except for the gas turbine unit, which will be redesigned, the rest of the existing components can be leveraged to reduce the capital investment. Figure 19 shows how a new gas turbine and a PFB HX can be installed to retrofit a retired NGCC plant. In some cases, a new HRSG is also necessary based on the exhausted hot air conditions from the new gas turbine. By leveraging steam turbines, cooling systems, and generators, the capital cost of a retrofitted NGCC plant can be less than half the cost of a new construction ABCC plant, based on the breakdown data shown in Figure 17. The retrofitted NGCC power system cost can be obtained using the following:

$$C_{PowerSys,Re-NGCC} = C_{turbine} + C_{HRSG} \quad (17)$$

where the HRSG cost will be deducted when the existing one can be repurposed.

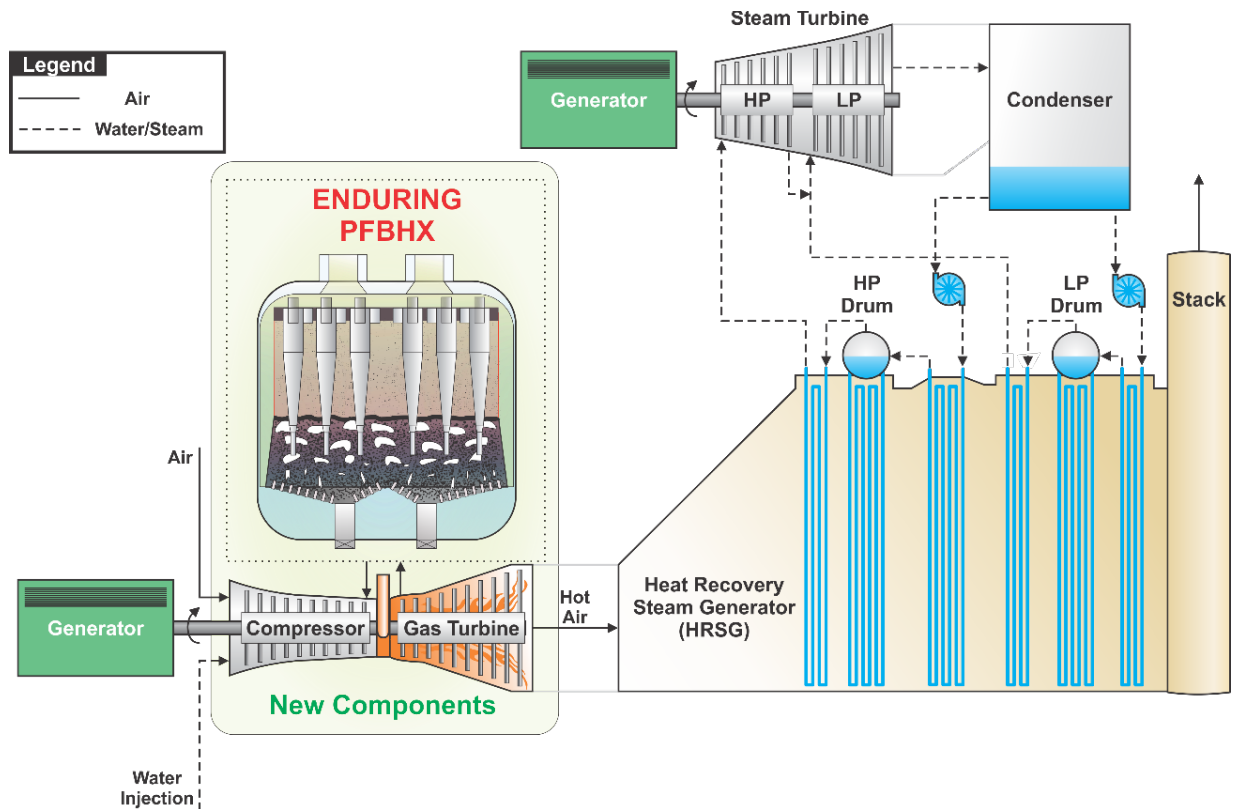


Figure 19. A storage configuration built on a retrofitted NGCC plant.

Retrofitted Coal Plant

The third scenario is leveraging the steam power generation unit in a retired coal plant. In order to generate steam, the fluidized bed boiler is equipped with water pipes located inside the fluidized bed to replace a combustion boiler. The air is circulated in the fluidized bed to enhance heat transfer. In addition, because the air will not be pressurized, the outer vessel no longer needs to withstand pressure, which reduces the material costs. Consequently, apart from the ENDURING power-specific and TES-specific components, the new, retrofitted system will only need an ambient-pressure fluidized bed boiler to replace the coal-fired boiler; this usually costs around \$150/kWt (\$300/kWe). The cost of a fluidized bed boiler is included in the retrofitting power system cost, while additional engineering and development cost would depend on retrofitting project that may be estimated per a relevant project.

Figure 20 shows a schematic of the retrofitted coal-fired power plant. This approach leverages existing infrastructure to reduce power system capital investment. However, the cycle efficiency in this scenario is lower than in the other two scenarios because electricity is generated only via steam Rankine cycle. However, considering the lower power system capital investment, the entire system's levelized cost of electricity can still be competitive when the storage input electricity price is low.

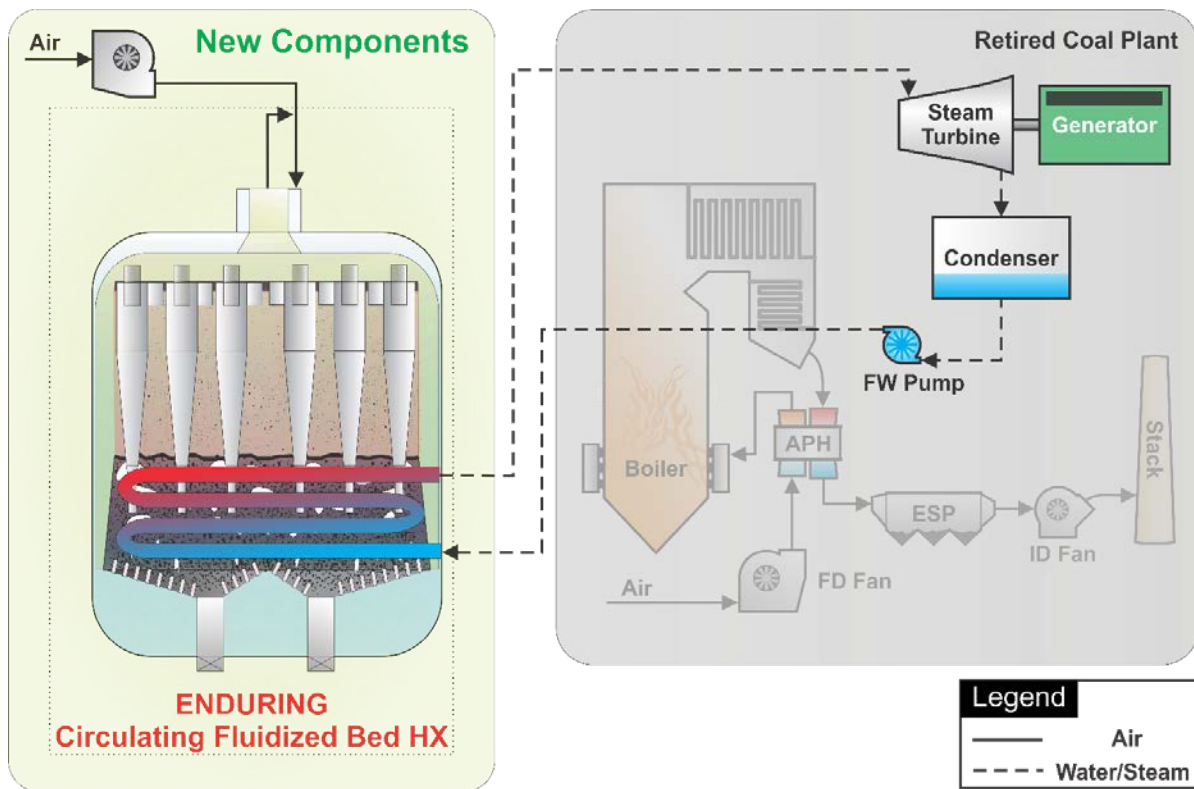


Figure 20. A storage configuration built upon a retrofitted coal plant.

Cost Results of Different Plant Scenarios

Following the DAYS formula for levelized cost of storage (LCOS), the cost breakdown is split into two capital costs: energy storage costs and power system costs [25]. The cost estimates for the energy storage for the retrofitted thermal power plants are assumed to be those calculated for the new-built case and have not be re-calculated for the retrofitted scenarios. After considering uncertainties in cost estimation of TES and skip hoists, we use the same cost of \$2/kWh for different plant scenarios in the TES section. A retrofitted coal-fired thermal plant will likely have a lower turbine temperature, resulting in lower-temperature storage and reduced use of insulation. However, the TES design will be verified only when such a retrofitting case emerges for detailed analysis.

The new-built ENDURING ABCC plant has an estimated capital cost of \$656/kW, which is in the same range as an NGCC plant (shown in Figure 21). For a retrofitted NGCC plant, the cost will be \$292–\$384/kW, depending on whether the HRSG can be modified for reuse. Finally, a retrofitted coal plant can have the lowest capital cost. Table 16 shows the cost breakdown of the major components used in each plant scenario.

However, a more comprehensive analysis that considers round-trip efficiency needs to be conducted to investigate LCOS as well as levelized cost of electricity. Design optimization can then be performed to obtain the optimal design and operating conditions of different ENDURING plant design scenarios.

Table 16. Estimated Capital Costs of Different Storage Configuration Scenarios

ENDURING Plant Capital Costs (Mean Values)	Plant Construction Scenarios		
	New Construction	Retrofitted NGCC	Retrofitted Coal
Components for Building Scenarios			
Power Generation System Capital Costs (\$/kW)	540	177–268	0.00
Gas Turbine Cost (Modified GE 7E.03)	177	177	-
HRSB Capital Cost	92	92	-
Steam Plant Capital Cost	105	-	-
Cooling System Capital Cost	34	-	-
Generator and Electric Plant Capital Cost	52	-	-
BOP, Misc., and Control	81	-	-
Power-Specific Component Capital Costs (\$/kW)	116	116	304
Gas Pipeline Cost	5	5	5
PFB System Cost	72	72	260
Lock Hopper Cost	22	22	22
Particle Heater Cost	17	17	17
Total Plant Component Capital Cost (\$/kW)	656	292–383	304

The ENDURING system based on low-cost particle TES has the advantage of integrating various power cycles. Figure 21 shows the range of power system costs for various integration scenarios, from adapting GTCC or retrofitting coal or gas plants to utilizing advanced pumped thermal energy storage (PTES). The cost scenarios are summarized in Table 17 to evaluate the LCOS results.

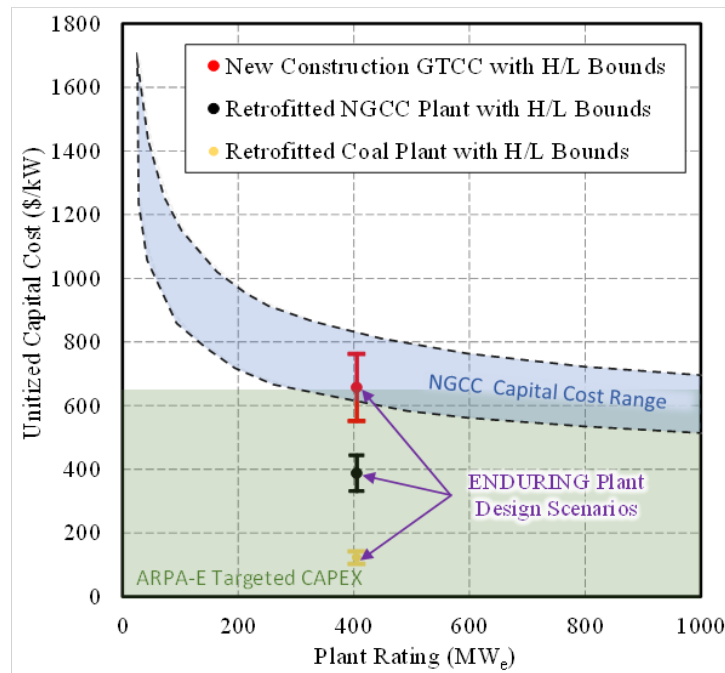


Figure 21. Capital costs of different ENDURING plant scenarios for a capacity of 405 MWe.

2.1.4.5 Results and Discussions of Techno-Economic Analysis on ENDURING Technology

Techno-Economic Analysis (TEA) on ENDURING Technology was focused on storage cost based on component and system analysis. The LCOS was calculated based on the method recommended by the ARPA-E DAYS program (Equation 1, [25]). We assess LCOS sensitivity to the electricity purchase price (P_c), round-trip efficiency (η_{RTE}), cost of power (C_p) and energy storage (C_E) systems, service life (t), and annual cycles ($n_c(t)$).

$$LCOS\left(\frac{\$}{kWh}\right) = \left[\left(\frac{1}{\eta_{RTE}} - 1 \right) P_c \sum_{t=1}^T \frac{n_c(t)}{(1+r)^t} + \sum_{t=1}^T \frac{O\&M(t)}{(1+r)^t} + \left(\frac{C_E}{\eta_D} + \frac{C_P}{d} \right) \right] \cdot \left[\sum_{t=1}^T \frac{n_c(t)}{(1+r)^t} \right]^{-1} \quad (1)$$

Additional cost estimation parameters:

- $C_E = \$2/kWh$ (assumed for all power systems).
- $\eta_D = \eta_{RTE} + 1.5\%$ (to account for thermal energy loss from storage).
- $O\&M(t) = \$2.50/kW\text{-y}$ for fixed operations/maintenance (O&M) costs [25]
- $r = 0.1$ is the discount rate over the project lifetime (20 years of service life).

Table 17 shows the input values for the different power system integration scenarios, including newly built ABCC (high and low), repurposed gas and coal plants, and emerging PTES technology. New-built ABCC power equipment with high and low-cost scenarios reflects uncertainty in price inputs of future equipment supply and a cost to develop the first-of-its-kind ENDURING system.

Table 17. Input Values for Power System Integration Scenarios

Configurations	Power System Cost (\$/kW)	Storage Cycle Efficiency	Power Capacity (MWe)	Storage Capacity hrs (GWht)
New-built ABCC, high	900	50%	50–400	10–100 (0.5–80)
New-built ABCC, low	650	50%	50–400	10–100 (0.5–80)
Retrofitted GTCC plant	350	46%	20–300	6–12
Retrofitted coal plant	304	40%	20–500	6–12
New-built PTES cycle	900	60%	10–200	10–100

Figure 22 shows various deployment scenarios for the ENDURING technology. These scenarios include deploying the newly built system on greenfield plants at high and low power system costs, retrofitting a retired coal plant by reusing its steam generation with a low power generation efficiency, and retrofitting a gas-turbine combined cycle plant by leveraging the generation system and running it at high generation efficiency.

The greenfield plant has the highest cost because it does not leverage existing infrastructure and equipment. In contrast, energy storage built upon existing thermal power plants provides an economic approach to achieving a competitive energy storage cost. The BEC capital cost analysis of the storage system did not include the cost of land, buildings, and permitting, which depend on market conditions beyond the scope of this project. Adding these factors may significantly increase the storage cost; this needs to be analyzed on a case-by-case basis. The

analysis results within the project scope emphasize the pathways to a LCOS target with significant technology and economic iterations for eventual LCOS outcomes.

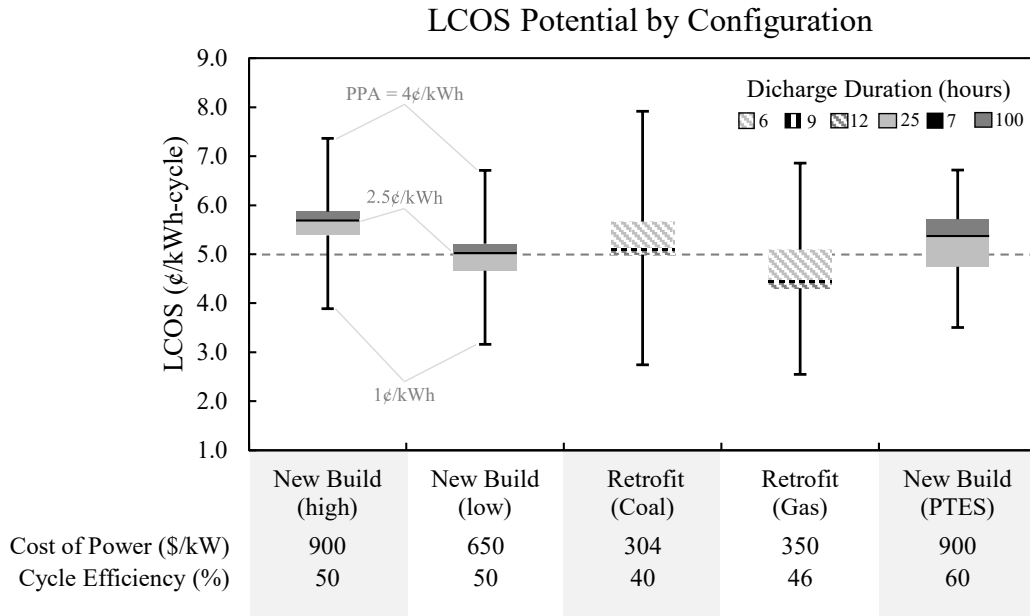


Figure 22. TEA scenarios for achieving the 5¢/kWh LCOS target (20 years life).

In addition to the scenario-specific ENDURING system analysis in Figure 22, Table 18 shows a more general set of baseline, favorable, and unfavorable assumptions for various inputs in Equation 1. These assumptions are used in the sensitivity analysis to identify key factors affecting the LCOS.

Table 18. Sensitivity Analysis Input Values

Value	Favorable	Baseline	Unfavorable	Unit	Notes
P_c	1.0	2.5	4.0	¢/kWh	Input electricity price during charging
η_{RTE}	60	50	40	%	AC system round-trip efficiency
C_P	400	650	900	\$/kW	Capital cost for power-specific components and BOP
t	30	20	10	years	System service lifetime
C_E	1.5	2.0	4.0	\$/kWh	Capital cost for energy-specific components and BOP
$n_c(t)$	162	59	45	cycles	Number of equivalent full charge-discharge cycles per year
d	25	75	100	hours	Storage duration
Additional assumptions: <ul style="list-style-type: none"> • $\eta_D = \eta_{RTE} + 1.5\%$ (to account for thermal energy loss from storage) • $O\&M(t) = \\$0.00171/\text{kWh}$ for fixed/variable operations/maintenance costs and periodic replacements • $r = 0.1$ is the discount rate over the project lifetime. 					

Results from the preliminary sensitivity analysis are shown in Figure 23, revealing a variety of scenarios that achieve the 5¢/kWh LCOS target. The entire ENDURING system needs further study for the conditions and possibilities in achieving the 5¢/kWh LCOS target because current cost analysis only focused on key components before pandemic and supply chain constrains. Price uncertainties would add challenges for cost reduction. Building upon existing thermal power plants would help facilitate a commercial path for the ENDURING system. Additional factors in improving system economic returns should be considered for commercializing the ENDURING system. They may include utility capacity payment, community benefits around retiring thermal power plants, and continuing decline of renewable electricity price. Designing the system for dynamic operation (e.g., faster startup, option for gas addition) is likely to increase revenue by tapping into daily storage operation. Our current component design, modeling, and sizing efforts have indicated that the cost numbers in Table 17 and Table 18 would be reasonably achievable.

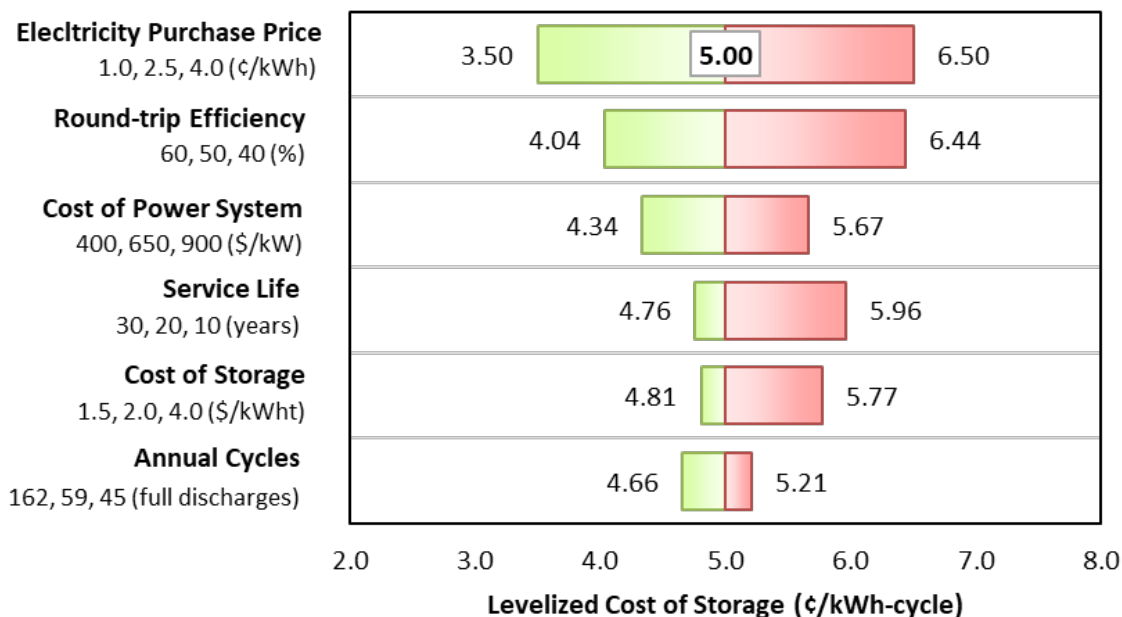


Figure 23. Techno-Economic Analysis sensitivities for a path to achieve the 5¢/kWh LCOS target: charging electricity price and round-trip storage efficiencies are two significant factors besides capital costs.

With low-cost silica sand and containment, particle TES represents an economical energy storage method. The particle TES is designed to operate at a high storage temperature (1,200°C) to support a high-efficiency thermal-power cycle. Such temperatures present unique challenges for developing and deploying TES and PFB HX components; however, the challenges are justified because power conversion efficiency is determined by thermal-cycle efficiency, wherein higher particle temperatures allow for a higher turbine inlet temperature to achieve higher thermal-power conversion efficiencies. The following sections describe our efforts to mitigate component risks by proving the components' feasibility at laboratory scale and conducting high-fidelity product-scale modeling.

PTES technology under development uses a high-temperature heat pump process to charge thermal storage [26,27]. Particle TES based on the ENDURING technology integrated with PTES shows promise for improving cycle performance for a high-storage round-trip efficiency above 55% and up to 70%[28]. The integration of PTES with particle TES and PFB HX can be attractive for long-term technology advancement beyond the ABCC system. The PTES integration is under consideration for evaluating advanced configuration linking with other DAYS developments. However, it stores both hot and cold thermal energy and needs two sets of TES units that incurs high equipment costs.

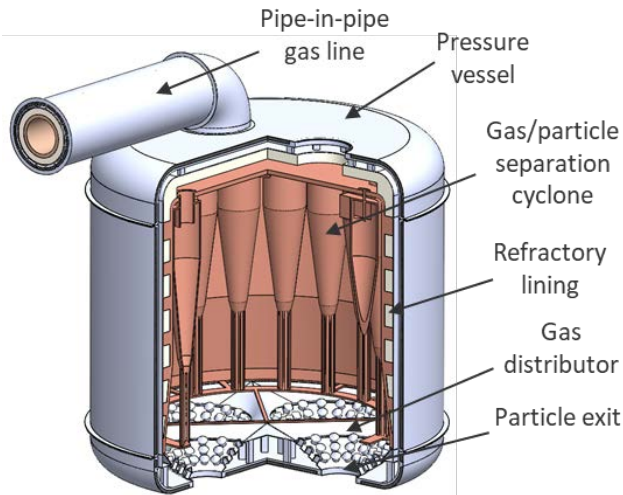
2.2 Task 2. Cold PFB Prototype Development and Testing

(Note: Work contributed by Xingchao Wang and Patrick Davenport.)

Conventional heat exchangers use a heat transfer interface to separate the two heat transfer media, such as shell-tube or plate-plate heat exchangers. Alternative and comparable heat exchanger designs for hot particles with a working fluid can take on one of two types of configurations: a moving packed bed or a fluidized bed. The PFB HX is a unique design that provides direct heat transfer between the hot particles and the pressurized air, as shown in Figure 24(a) [29]. The uniqueness of the PFB HX is the air/particle direct contact counterflow heat transfer. The outer shell holds pressure, whereas the inner shell contains the high-temperature counterflow PFB HX. The airflow is directly integrated with the compressor and turbine through a tube-in-tube connection. The direct air/particle contact eliminates the heat transfer surfaces, thus eliminating the interface materials and their associated temperature limitations and costs.

Figure 24(a) shows the design of a PFB bed for direct air/particle heat transfer. The commercial-scale PFB HX design was derived from a PFB combustion boiler after removing coal combustion and pollution reduction systems [30]. The PFB HX design is configured to directly heat pressurized air using hot particles in a counterflow fluidized bed. Cooler pressurized air from the compressor of the turbomachinery flows through the fluidized bed. In an ideal case, air exits the PFB HX at the hot particle temperature to drive the downstream turbomachinery to produce power. Aspects of the PFB HX and the ABCC loop were derived from a commercial PFB boiler integrated with a GTCC system [5, 25].

Figure 24(b) shows prototype test stations for cold (left) and hot (right) prototype testing. The cold prototype test is for observing fluidization conditions using a transparent vessel. The hot prototype test was developed to investigate the air/particle heat transfer performance and operation of the PFB HX at design conditions of approximately 1 MPa and an air exit temperature of 1,170°C.



(a) Commercial-scale PFB HX conceptual design.



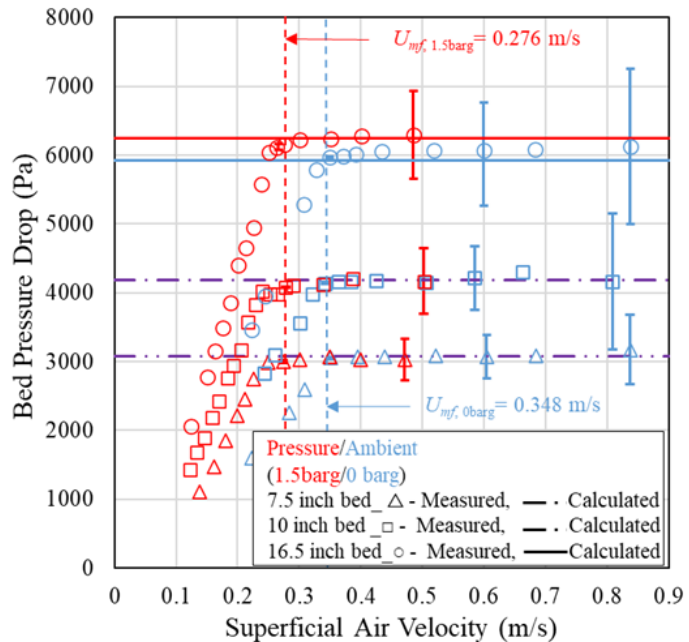
(b) Cold (left) and hot (right) prototype testing stations.

Figure 24. The design of a PFB for direct air/particle heat transfer.

Figure 25 shows the cold prototype PFB bed and the test results obtained by measuring the airflow and pressure drop at ambient temperature and pressurized conditions up to 250 kPa. The cold prototype uses transparent plastic columns for flow visualization. It verifies the fluidization condition and minimum fluidization velocity through pressure measurements and direct observation.



(a) PFB prototype for fluidization test at ambient condition. Photo by NREL.



(b) Fluidization test results for fluidization conditions and pressure drop (theoretical $U_{mf}=0.25\text{m/s}$).

Figure 25. Cold PFB prototype fluidization test at ambient, pressurized conditions.

Minimum fluidization occurs when the bed pressure becomes constant with increasing air velocity, indicating that the fluidizing air is suspending the particle weight. The minimum fluidization velocity for initial bed heights of 0.191 m (7.5 in.), 0.254 m (10 in.), and 0.419 m (16.5 in.) was measured to be 0.276 m/s on average at ambient temperature and an absolute pressure of 250 kPa. Figure 25(b) indicates good agreement between the measured pressure drop and the theoretically calculated pressure drop using Ergun equation. Theoretically the minimum fluidization velocity is around 0.25m/s at ambient condition and shows an adequately consistent minimum fluidization velocity across bed heights.

2.3 Task 3. Particle Heating Demonstration and TES Model Validation

The storage system starts from an electric charging particle heater that is designed and operated using modules. Electric resistive heating is inexpensive and efficient, with a theoretical 100% electric-to-thermal conversion efficiency if the electric heater is perfectly insulated. The heater is designed to be flexible and easily controlled for rapid ramping rates and charging response. The simplicity of charging particle TES using an electric heater provides implementation convenience for ETES usage for electricity storage.

Stable silica sand is used as a storage medium. Silica sand is not corrosive and is compatible with refractory materials, thus providing flexibility in selecting heating element materials, thermal insulation, and element shapes; however, heating particles with an electric heater relies on particle granular flow and heat transfer, which is less effective than heating a liquid medium such as water or molten salts. To deal with the challenge of particle heat transfer, we performed modeling and prototype testing to characterize the particle flow and heat transfer. Here, we present a preliminary design with an optimized heat transfer process and heating element choice for charging the particle ETES system.

2.3.1 Electric Charger Heater Design and Prototype Development

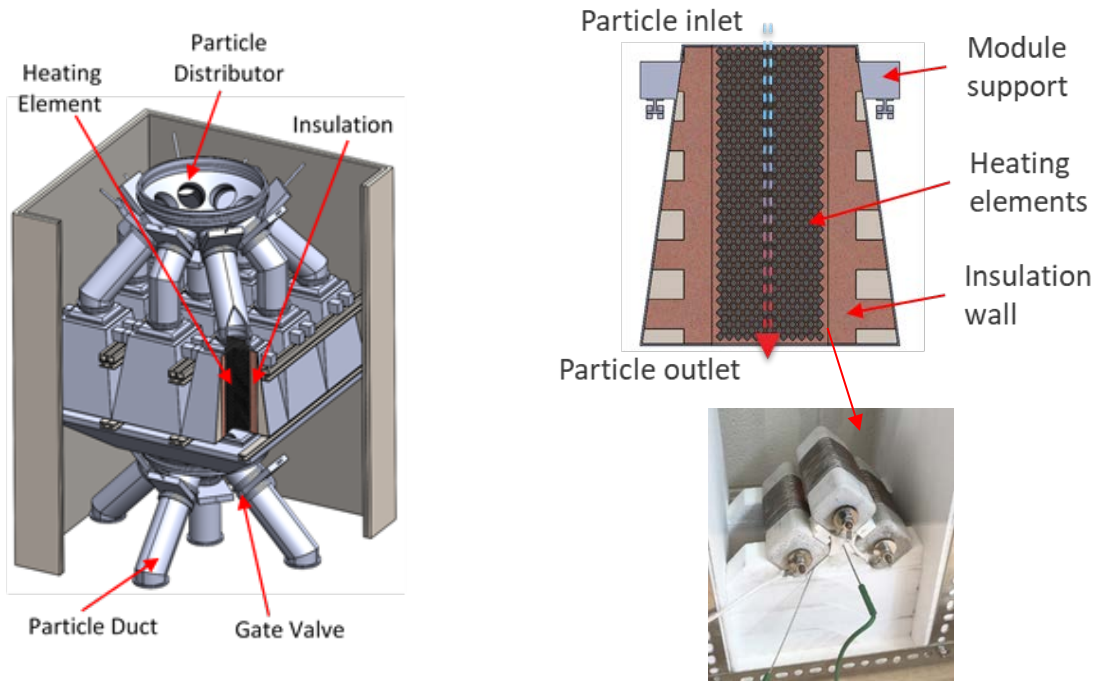
(Note: Work contributed by Jason Schirk and Aaron Morris at Purdue University.)

2.3.1.1 Particle Flow and Heat Transfer Simulations

The electric charging heater is designed in a modular configuration for particle flow and load control [31]. Figure 26 illustrates the charging heater assembly and heater designs. The heater has arrays of hexagonal heating elements to heat particles in granular flow. Each heater module is internally insulated and supported by an external structure. An individual module operates at a fixed heating capacity with a designated particle flow rate designed for the most effective heat transfer rate, and independent on/off control for each module enables stepped control of the overall heater load.

The operation of all nine modules (shown in Figure 26(a)) provides a full charge load, and the operational combinations of modules create nine load steps. Figure 26(b) shows the module design, which consists of arrays of hexagonal heating elements. Particles fall through the heating elements in a gravitation-driven granular flow pattern across the heating elements, and are heated to the desired temperature. The particle flow rate is regulated by the shape of the heating elements and the gaps between them. A strong silica-carbide-based refractory material with high hardness is used for the heating elements to support metal heating wires and to provide erosion resistance to particle flow. Prototypes have been fabricated using an electric resistive heater with

heating wire wrapped on hexagonal refractory supports (Figure 26(b)). Tests were focused on particle flow and heat transfer to validate the heater module design.



(a) Heater assembly.

(b) Charging heater module and heating elements.

Figure 26. Modular design of electric particle heater for charging particle TES. Illustrations and Photo by NREL.

A particle granular flow regime simplifies the charging heater design relative to a fluidized bed and improves particle heat transfer relative to a dense, moving packed bed particle flow regime. Particles drop through staggered hexagonal heating elements, and the periodic mixing and direct contact with the heating surfaces enhance particle heat transfer. The shape, size, and arrangement of the heating elements were optimized to achieve the desired particle flow and heating effectiveness. Improving particle heat transfer increases power density and reduces the size, cost, and heat loss of the heater. We performed both modeling and testing to investigate particle flow through the heating elements and to realize the desired heat transfer.

2.3.1.2 Particle Flow and Heat Transfer Simulations

We initially analyzed the heater design by mathematical modeling of the particle granular flow around the heating elements. The model was developed using the discrete element method (DEM) in the Multiphase Flow with Interphase eXchanges (MFIx) software [32–34]. The modeling methods and simulation parameters are described in reference [35], which lists the conservation equations, modeling approaches, and input parameters.

The primary parameters of interest are those that influence the rate of heat transfer, including (1) heating element geometry, angle, and spacing; (2) inlet hopper angle; (3) particle-particle friction; and (4) particle-wall friction [36]. Shallow hopper angles are ideal for heat transfer because they increase the particle residence time; however, a small slope angle, θ , increases the

risk of particle flow stagnation. Also, high friction coefficients restricts the particle flow, which decreases the heat transfer rate. These effects were simulated using the MFIX heater model, which guided the heater design and performance analysis. Figure 27 shows the computational domain and results for a few select cases from the parametric study detailed in [36].

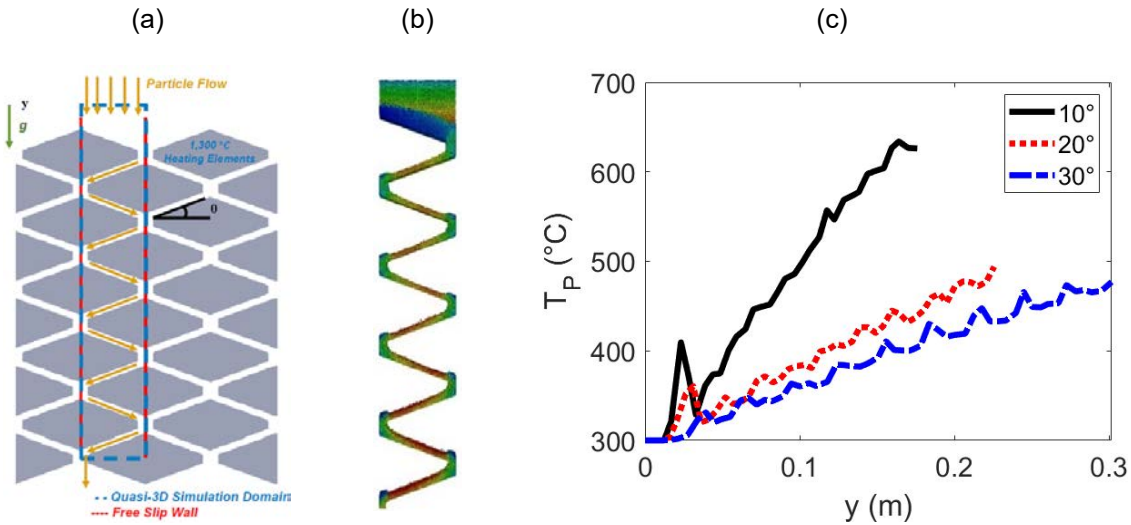


Figure 27. Overview of the MFIX-DEM modeling effort, including (a) definition of the modeling domain, (b) particle velocity contour plot, and (c) average particle temperature profiles for several geometry angles as a function of heater depth over the computational domain.

All the simulations shown in Figure 27(c) were set to control the particle flow rate via the heating element geometry and the gap between elements. Hexagonal heating elements break down the particle flow stream, provide direct contact for particle heating, and blend particles through each flow path, resulting in a high heat transfer rate for charging hot particles. The particle temperature profile and mass flow rate from the DEM simulations are used to determine the effective heat transfer coefficient, which ranges from 500–1,500 W/m²-K, depending on the geometry and the friction coefficient on heater shape and particle heat transfer. This result shows temperature rise with a fixed particle travel depth; lower temperature rise means longer heater height will be needed for a large heater, which would be more costly and increase heat losses in a large-scale heater array. A heat transfer coefficient can reduce the heater size necessary to achieve the design outlet temperature. Figure 27(c) shows the particle temperature along the height of the heater with three different slope angles (θ) of the heating elements.

A section of the modeling results was extrapolated to the full-scale design. Particles often develop flow instabilities, as indicated by the unsmooth curves in the temperature profiles in Figure 27(c). The spike at the top of the simulation is due to stagnant particles on the first row of heaters. Stationary particles are not seen in subsequent rows. Figure 27(c) indicates that a small slope angle or less steep top of the heating elements improves heat transfer because of the slow flow rate and correspondingly longer heating time associated with a flat heater top; however, a small surface angle risks particle flow stagnation. Thus, we applied flow visualization to observe the particle flow patterns and select an optional geometry of the heating elements.

2.3.1.3 Particle Flow Visualization Test

(Note: Work contributed by Xingchao Wang and Patrick Davenport.)

We adapted experimental particle flow test stations to mirror the MFIX-DEM modeling domain for various candidate heating element geometries to determine the mass flux at ambient temperature. Figure 28 shows several flow visualizations and the resulting particle mass accumulation rates. In total, we used four different flow stations to test more than 10 heating element arrangements with varied geometries, angles, and spacing. The measured particle mass accumulation rates shown in Figure 28 indicate steady particle flow rates and therefore good particle flowability for a variety of heating element configurations.

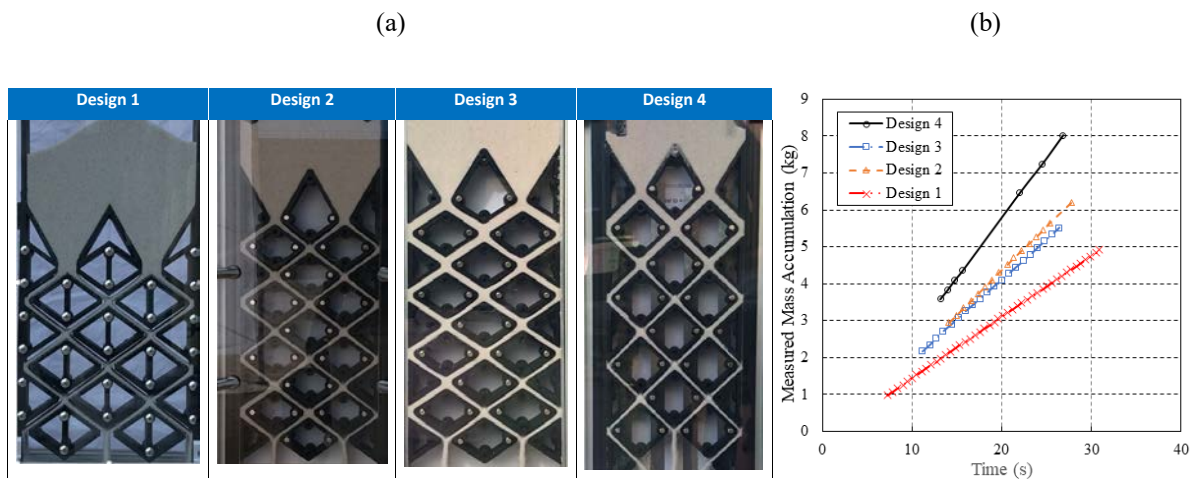


Figure 28. Experimental results, including (a) testing of four different cases from the parametric study described in Section 3.1.2 and (b) determination of the resulting mass flow rates.

Figure 29 shows the second experimental test station that was used to test the heating elements for the electric charge particle heater. The test station was designed to simulate a commercial-scale electric heater, and it operates at temperatures expected in commercial operation. The heating elements were fabricated and wrapped in heating wires. The test station was comprised of three stages, including batch pre- and post-heating and particle flow through the heating elements. This staged setup was necessary because the full temperature range could not be explored in the heating elements alone within the power limitations of the test station. Each stage was fabricated and stacked to test the particle heating process at various temperature ranges.

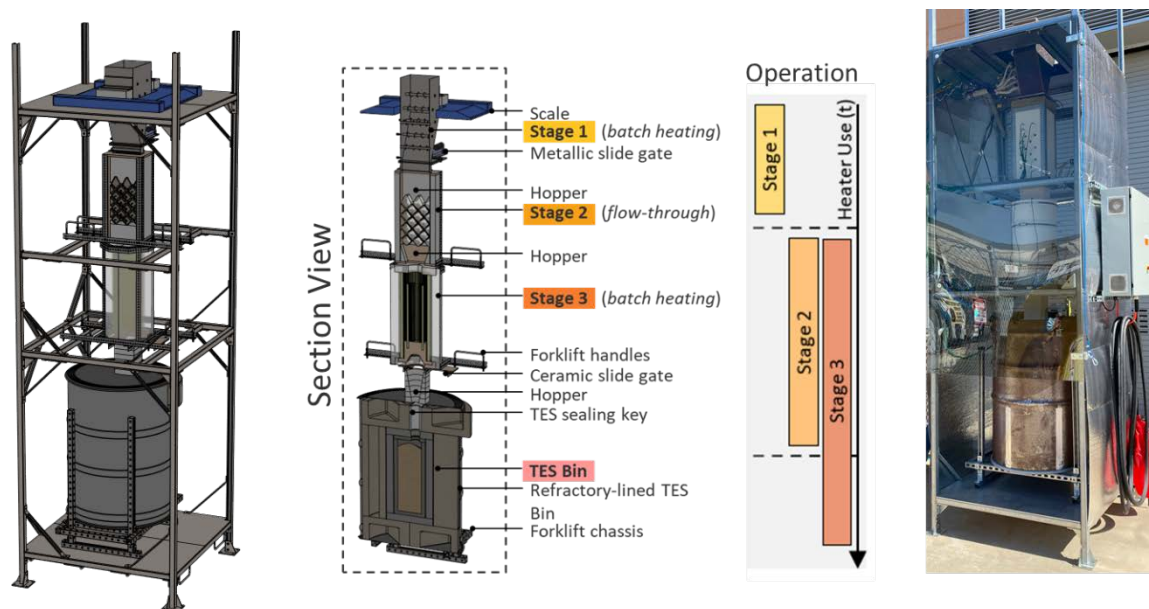


Figure 29. Detailed rendering of the entire assembly (left), a cross section revealing the particle flow path (middle), and an image of the assembled test station (right).

The stage 1 assembly, as shown in Figure 29, includes cartridge heaters to preheat particles to a desired temperature in batch heating. The flow rate through stage 2 was calculated by supporting stage 1 within an industrial Adams scale. The particles are manually poured into the stage 1 hopper, and batch heating then increases the particle temperature up to 500°C. A metallic slide gate can be activated to allow particles to flow from stage 1 through stage 2. Within stage 2, heating elements heat the particles to temperatures as high as 900°C, with complete measurement of particle temperature changes to derive particle heat transfer over the tested heating elements.

After exiting the array of heating elements, the particles flow into stage 3, which again uses batch heaters to increase the temperature to 1,200°C in order to test the storage prototype bin and insulation at the design point temperature. A high-temperature alumina slide gate then opens for particles to drop into the TES bin. The temperature data from the TES bin were used to validate a computational model studying heat loss from insulated storage silos.

Particle heat transfer rates associated with different heating elements affect the heater size, thermal efficiency, and cost. The simulations shown in Figure 27 provide insights into which designs achieve effective heat transfer. Substantial development has taken place to verify the performance of the heating elements and to validate the heat transfer rates predicted by the DEM simulations.

Figure 30 shows simulated heat transfer coefficients for varying surface angles and friction coefficients (μ). A single tested heat transfer coefficient was obtained from the heater test. The measured value is higher than the modeled results, likely due in part to a radiation effect that enhances the heat transfer between the heater surface and the particles. Likely the most significant reason for the discrepancy was that the heating elements were wrapped with heating wires forming semicircle surfaces, which creates a larger surface area than the smooth surface in the MFI DEM particle heat transfer model. A rough estimation on increase in surface by semicircle wire areas indicates that particle heat transfer coefficient measured in experiment could be in the range of simulated results.

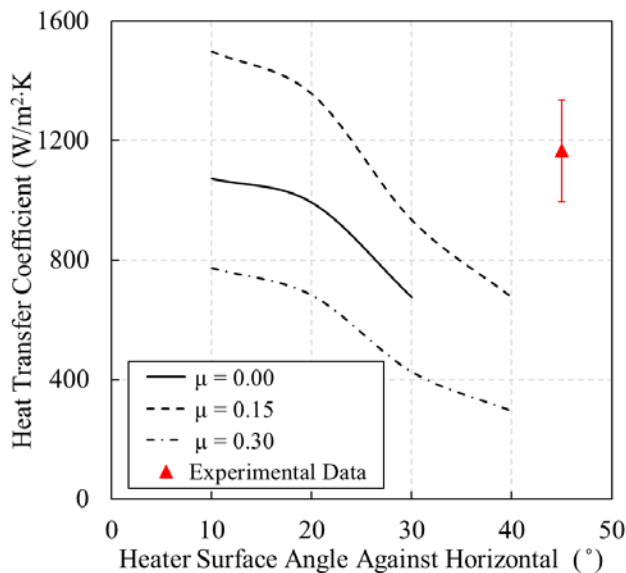


Figure 30. Effects of surface angle and friction on the overall heat transfer coefficient.

The surface angle shows an optimum heat transfer at an angle of 20°. Surface angles larger than 20° have a negative impact on the overall heat transfer coefficient in model prediction. Moderate friction ($\mu=0.15$) increases the heat transfer coefficient, whereas large particle-particle and particle-wall friction values decrease the heat transfer coefficient. Heat transfer coefficients decrease as the surface angle increases, and 20 degrees was selected as a preferred angle by modeling to balance the high heat transfer coefficients observed at low surface angles against the lower risk of particle stagnation at high surface angles.

2.3.2 Particle TES Design and Modeling

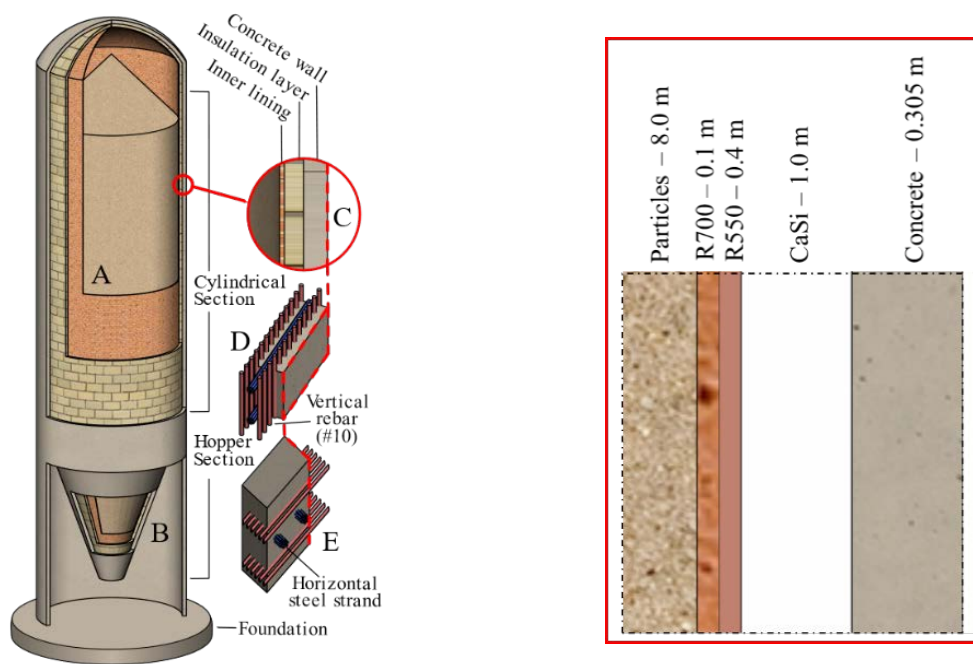
(Note: Work contributed by Xingchao Wang, Patrick Davenport, and Jeffrey Gifford.)

The high-efficiency particle TES is charged by electric heating, and hot particles are stored in well-insulated containment vessels. The TES containment configuration consists of a concrete silo and refractory insulation to hold the hot particles at conditions compatible with materials usable temperature and the thermal loss target. The design was based on earlier NREL work on high-thermal-efficiency TES development for a particle-based concentrating solar power (CSP) system, following codes and standards for concrete structures cited by [9] [37]. Within the project, we considered commercial refractory materials and related industry experience in refractory installation for both the design and associated cost assessment for the TES containment system.

Figure 31(a) shows the containment structure, including the concrete silo and insulation layers. Section views A and B show the cylindrical and hopper section contents, respectively. Detail C shows the wall configuration, which comprises an inner lining with a strong refractory (R700) for erosion resistance, insulation layers, and an outer concrete wall, as illustrated in Figure 31(b). D and E renderings show the rebar and strand layouts within the concrete walls of the cylindrical and hopper sections, respectively. Figure 31(b) shows the TES insulation material selection and layer thickness for the performance results described next.

The silo shown in Figure 31 is internally insulated with refractory lining and insulation layers. The lining and insulation layers are necessary to maintain the temperature of the concrete silo below the concrete allowable use temperatures. The TES capacity, size, and cost were estimated using material data and our earlier particle TES design work [4,9], then adjusted based on the higher energy density in the LDES system due to the larger temperature difference within that system. Silica sand provides a higher particle density and higher heat capacity than the coal ash described in our previous work [37]. Storing large volumes of granular media in silos is well established in industry; however, heating and storing ultrahigh-temperature particles while minimizing heat loss requires an innovative design. Applying insulation inside a tall silo can be challenging and was evaluated by our industry partner who specializes in refractory materials. Large refractory blocks can be fabricated and stacked inside the silo to form a modular insulation layer.

Minimizing thermal loss rates through the TES containment is critical to maintaining high particle temperatures—and thereby high thermal-to-electric efficiency during discharge—for long-duration storage applications.



(a) TES containment design for particle storage. (b) Zoomed-in view of section C: TES insulation materials and dimensions.

Figure 31. Particle TES containment design and insulation layers.

To study the trade-off between insulation design, system performance, and cost, we used a transient, 1D thermal insulation model. Figure 32 shows the thermal resistance model with various insulation layers, concrete walls, and ambient heat transfer. Key variables, such as thermal resistance, energy flows, material properties, and dimensions, are also defined. We analyzed three insulation mechanisms between the bulk particles of the storage silo and the ambient environment. First, a film layer composed of two parallel resistances represents the film conduction of the gas g and particle p phases. This film layer is considered mass-less, with no thermal mass. Second, the primary insulation layers are designed with four insulation layers, as shown in Figure 31(b).

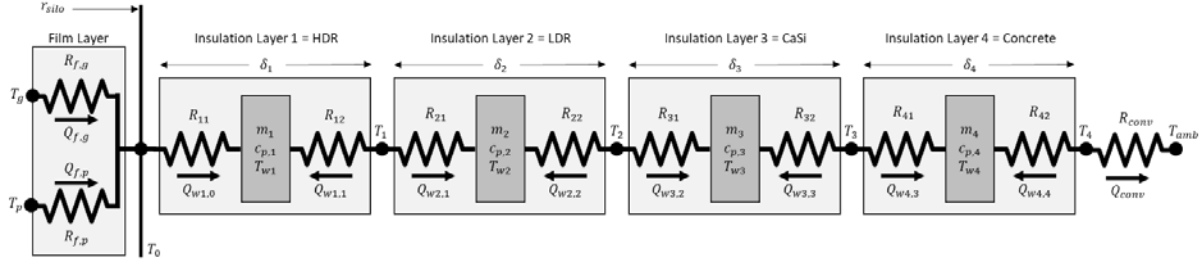


Figure 32. Graphical representation of the mathematical description of both the volume and the insulation model that comprise a single particle storage silo model.

Four layers have significant mass and heat capacities such that they absorb, store, and release thermal energy. Insulation layer j is assumed to have a mean temperature at the center of a given insulation layer T_{wj} . The parameter R_{conv} describes the convective thermal resistance between the exterior wall of the particle storage silo and the ambient. Gas and particle temperatures T_g and T_p , respectively, are the connection points between the insulation and the thermal mass subcomponents of the overall particle storage model. The ambient temperature T_{amb} is considered a fixed parameter. T_g , T_p , and T_{amb} are the boundary conditions for the insulation model. The film layer thermal resistances are defined as follows:

$$R_{f,g} = \frac{\delta_{f,g}}{\pi D_{silo} H_g k_g} \quad (1)$$

$$R_{f,p} = \frac{\delta_{f,p}}{\pi D_{silo} H_p k_p} \quad (2)$$

Here, H_g and H_p are the heights of the gas and particle medium in the storage silo at a given time, respectively; $\delta_{f,g}$ and $\delta_{f,p}$ are the gas and particle medium film thicknesses, respectively; and D_{silo} is the inner diameter of the silo. The thermal resistance between node i and layer j is as follows:

$$R_{i,lj} = \frac{\ln \left[\frac{r_{silo} + \sum_{j=1}^{j-1} \delta_j + \frac{1}{2} [2 - (j - i)] \delta_j}{r_{silo} + \sum_{j=1}^{j-1} \delta_j + \frac{1}{2} [1 - (j - i)] \delta_j} \right]}{2\pi H_{silo} k_j} \quad \forall j \in J, i \in \{j - 1, j\} \quad (3)$$

Each insulation layer has two thermal resistance terms: one for the inner half of the cylindrical layer and one for the outer half of the cylindrical layer. The thermal resistance model was used to study insulation performance and its sensitivity to design and cost.

The simple transient 1D heat equation model was built to analyze initial insulation designs and to conduct a sensitivity study on thicknesses of each insulation layer. The model used a standard commercial partial differential equation solver. This preliminary sizing tool provided a more computationally efficient method to iterate over the insulation design prior to simulation via the computationally expensive FEA methodology.

The simple thermal model yielded a promising insulation design that was in line with the thermal limits of the materials. The insulation design is shown in Figure 31(b) and was applied to a commercial-scale particle storage silo geometry. The commercial-scale model examined a storage silo designed to store 6.5 GWh_{th} of TES capacity.

We have developed transient finite element analysis (FEA) models for both prototype-scale and commercial-scale TES containment analysis. The thermal models used the FEA method and applied different operating conditions and geometries appropriate to each scale. Figure 33 shows the FEA modeling results for the bulk average particle temperature over progressive operating cycles. Initially, each successive cycle has a slightly higher temperature profile, but after the fourth cycle, the bulk average particle temperature does not change significantly.

From Figure 33, we see that the particle temperature at the end of the storage step of the final cycle was 1,181.7°C. This represents a thermal efficiency of 98% after five days (120 hours) of storage, exceeding the original design target of less than 5% efficiency loss after five days of storage (i.e., an average of 1% loss per day of storage). A longer storage duration would offer a similar storage thermal efficiency because the rate of heat loss decreases over time. Half of the temperature decrease between the start and end of the storage duration occurs in the 24 hours of the storage period.

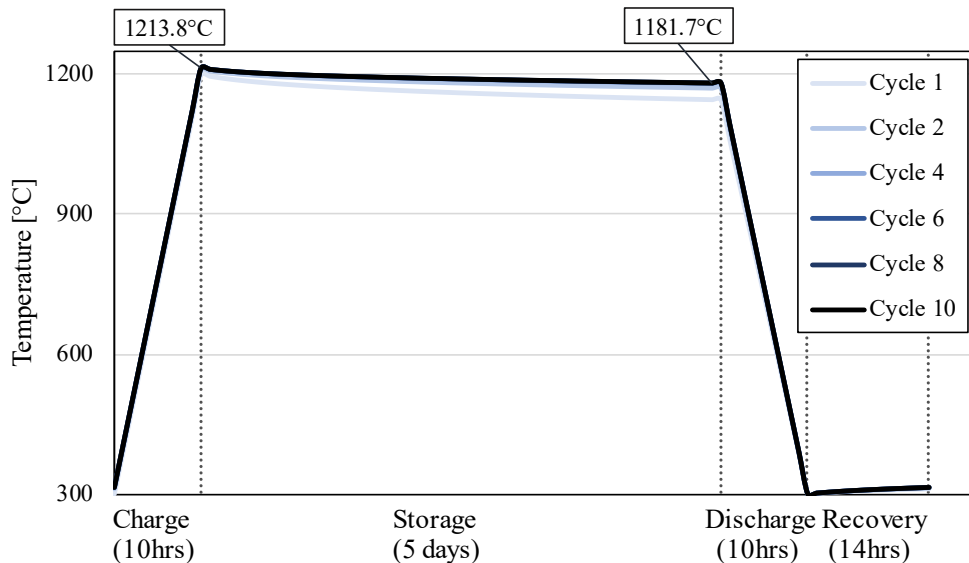
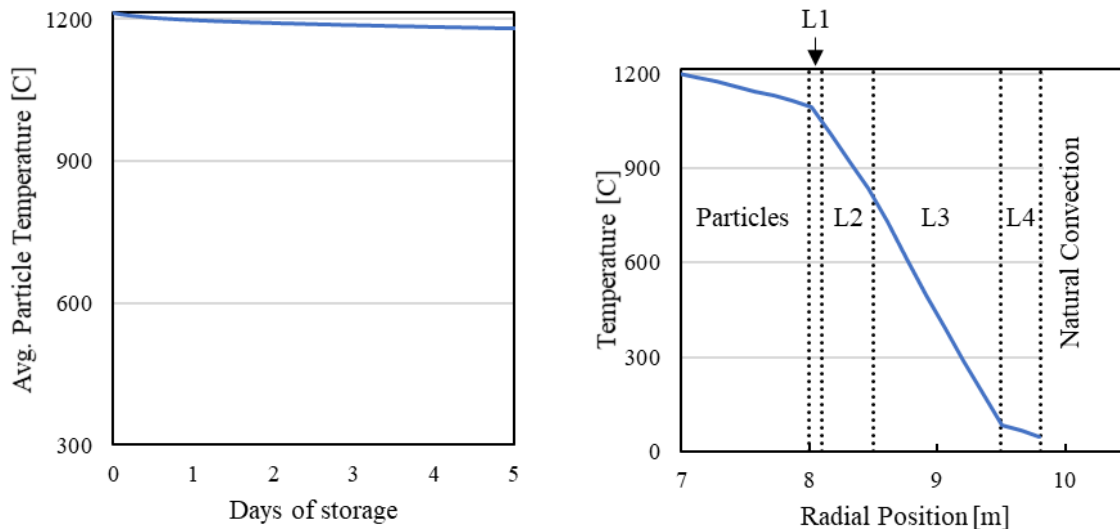


Figure 33. Bulk average particle temperature over selected operational cycles; not all cycles are presented for conciseness. Vertical dotted lines mark changes in operating step; x-axis is not to scale.

To reduce the overall containment cost, either hot or cold particles can be stored in any empty well-insulated silo without mixing hot and cold particles. The development of a low-cost particle TES was reported previously for a 100-MW_e steam Rankine power cycle with a TES capacity of 6.5 GWh_{th} for a single silo and 26 GWh_{th} for four silos for a 100-hour duration [38]. Storing both hot and cold particles in the same silo in stratified layers can reduce the containment cost by nearly half when single containment is feasible, e.g. completely charging or discharging the storage silo. During discharge, hot particles feed into the PFB HX by gravity and heat the fluidizing air, which is then used to drive the turbine to generate electricity. An industrial particle

conveyor is used to transport the cold particles from either the particle exits of the PFB HX to the top of the silo (during discharging) or from the outlet of the silo to the particle heater (during charging). The electricity storage cost depends on the thermal-power conversion efficiency. The basic TES material and assumed constructure cost, including storage media, concrete silos, and insulation, was estimated to be approximately $\$2/\text{kWh}_{\text{th}}$ [38]. For a 50% round-trip efficiency, a simple conversion implies an electricity storage cost of approximately $\$4/\text{kWh}_e$ for the storage media and containment, not including the capital cost of power generation. The cost of energy storage media and containment can be an order of magnitude lower than most storage methods in large storage capacity of LDES applications [39]. Recent developments have further assessed the economics of particle TES and support its potential in LDES [29] and industry process heat.

An FEA model solved the 3D transient heat equations using the ANSYS Mechanical software and used the same simulation software, solution methodology, and refractory materials as the prototype-scale model and experimental setup. The results of the commercial-scale FEA model are shown in Figure 34.



(a) Average particle temperature over five days (120 hours) of storage.

(b) Radial temperature profile after five days of storage.

Figure 34. Temperature profiles from product-scale TES containment model.

The computational results show that the insulation design retains 98% of the thermal energy after five days of storage, with an average particle temperature greater than $1,180^{\circ}\text{C}$, as shown in Figure 34(a). This high efficiency of the storage silo was relatively insensitive to ambient conditions and operating cycles. The 1D temperature profile in Figure 34(b) shows the radial temperature distribution through the particle domain and the various insulation layers. Particles within the 7-m radius core remain very close to $1,200^{\circ}\text{C}$ even after five days of storage. This illustrates the self-insulating effects of the particles due to their solid, static nature (compared to a liquid storage medium, in which free convection can induce mixing).

Layers shown in the temperature profile in Figure 34(b) include L1: high-density refractory lining; L2: low-density refractory layer; L3: calcium silicate; and L4: concrete. The temperatures through insulation layers L2, L3, and L4 drop substantially, and they are lower than 100°C on

the inner face of the concrete silo, which ensures that the concrete structure is within its thermal allowance. The insulation design simulated here achieved the target <1% energy loss per day.

2.3.3 Particle Heating Cycling Demonstration

In addition to the particle stability characterization in section 1.1, particle heating and cyclability were tested by heating particles from 300°C to 1,200°C in the hot prototype PFB HX, as shown in Figure 24(b) (right). Seven heating/cooling cycles were performed, starting at 1,100°C in cycle 1 and ending at 1,250°C in cycle 7. The tests were conducted at one hot/cold cycle per day for seven continuous days. Particle size distributions were measured before the cycling and again after the seven heating cycles were complete. The size distributions were compared with the particle stability test described in section 1.1 and consistent thermal stability was verified.

The focus of these cycling tests was mainly on comparing the particle size distributions before and after the cycling, as well as comparing them with the results from milestone 1.4. However, the heating process inside the hot prototype PFB HX also provides information on the bed temperature profiles without fluidization. The temperature profiles of cycles 1 and 7 are shown in Figure 35(a) and (b), respectively.

The “Air” line corresponds with the temperature of the air above the bed; the “Bed Top” line corresponds with the temperature at the top of the bed, the “Bed Mid” line corresponds with the temperature in the middle of the bed; and the “Bed Bot” line corresponds with the temperature in the bottom of the bed. As can be seen, the bottom of the bed was cooler than the top of the bed. The top temperature of the bed was the set point and followed closely with the air temperature. Because of the temperature differences in the bed, the particles at the top of the bed were specifically selected to be used in the particle size distribution measurements.

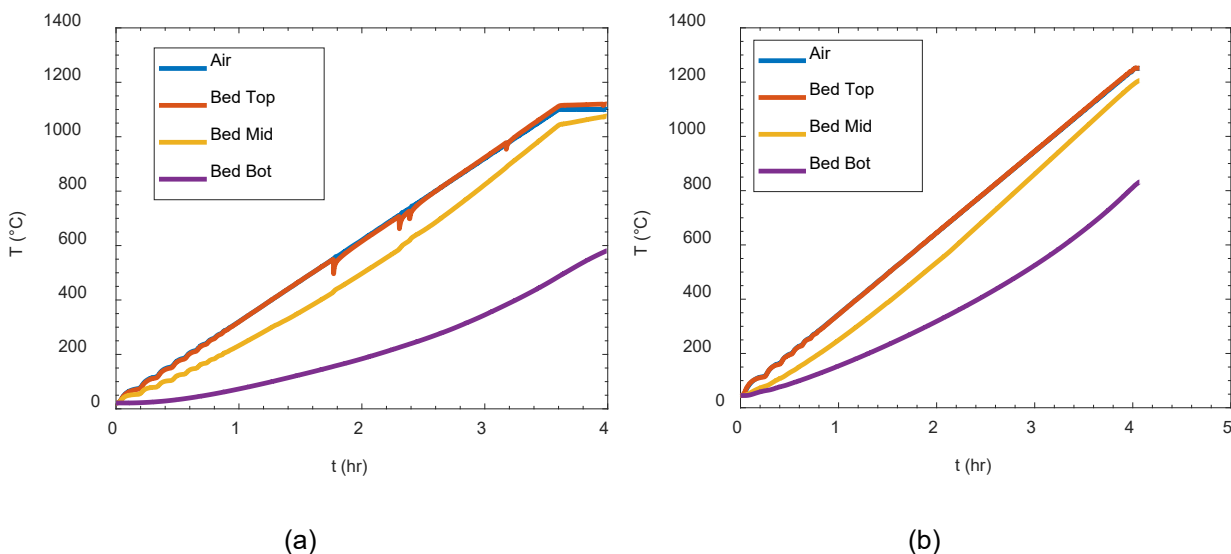


Figure 35. Temperature profiles of (a) cycle 1: 1,100°C and (b) cycle 7: 1,250°C.

The primary focus of the tests was particle stability, which was quantified by the change in the particle size distribution after cycling the particles. Figure 36(a) and (b) show the size distributions for milestones 3.2 and 1.4, respectively. The particle size distributions were

obtained using the Malvern Mastersizer 3000 at Purdue University. The Mastersizer utilizes laser diffraction to measure a volume-based size distribution for a set of particles.

The size distributions in Figure 36(a) are nearly identical before and after the cycling, meaning the particles are very stable. In the particle heating cycle test inside a furnace (Figure 36(b)), the distributions fluctuate slightly back and forth from 25 to 50 cycle and then to 100 cycles. One thing to note is that the size distribution through seven heating cycles inside a fluidized bed (Figure 36(a)) has fewer smaller particles than the furnace cycle test. This occurs because the particles tested in the fluidized bed were sieved before being placed into the hot PFB experimental setup. The sieving of particles less than 375 microns is necessary to keep the pressure tubes (used in fluidization tests, but not in these heating tests) free of fine particles to avoid clogging. Overall, the change in the distribution is very small in both tests.

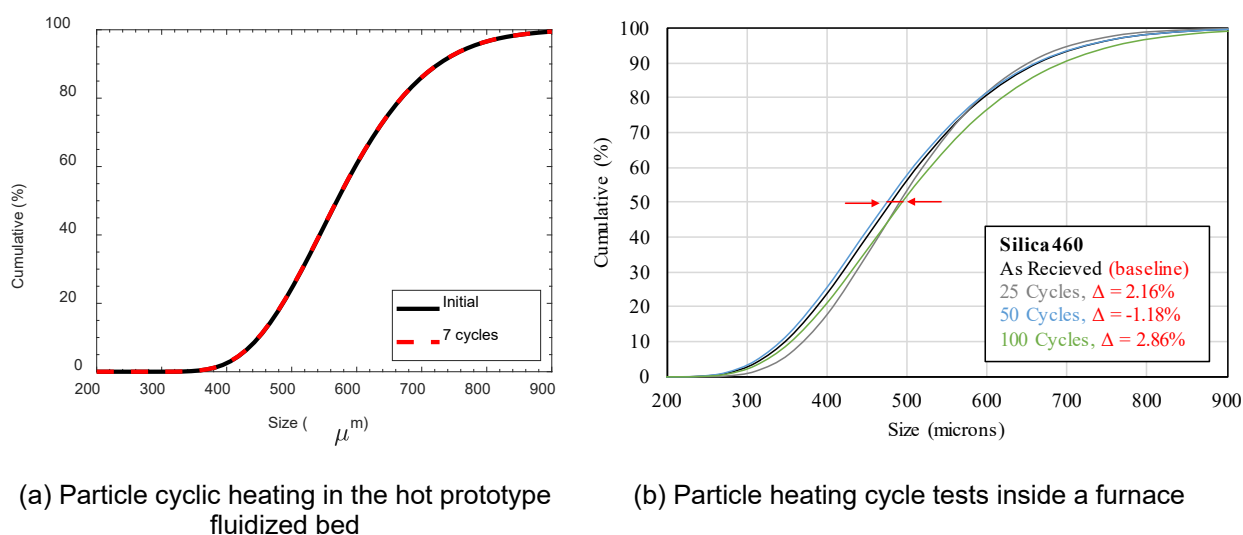


Figure 36. Cumulative particle size distributions before and after particle heating.

2.4 Task 4. Hot PFB Prototype Development and Testing

(Note: Work contributed by Jason Schirk and Aaron Morris at Purdue University.)

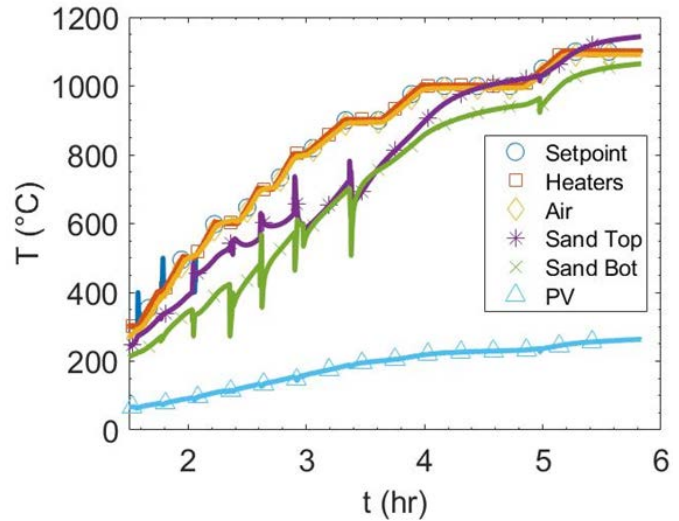
Hot prototype test results are shown in Figure 37. Temperature measurements are shown at two locations within the fluidized bed, denoted as “Sand Top” and “Sand Bot” in the legend, alongside the heater set point temperature and air temperature above the fluidized bed. Figure 37(b) indicates that the internal fluidized bed can reach high temperatures while maintaining relatively low temperatures in the surrounding pressure vessel (denoted as “PV”).

Prototype-scale and product-scale models of the PFB HX using the computational fluid dynamic (CFD) software ANSYS/Fluent were subsequently developed based on the hot PFB prototype test results. The aim was to use the prototype-scale model to validate the CFD methodology and framework against the prototype testing results shown in Figure 37. Then, the validated approach can be applied to the study of the commercial-scale performance of the PFB HX. The Eulerian-Lagrangian DEM approach is feasible for the prototype scale but is intractable for a commercial-scale PFB HX. The CFD models use a Eulerian-Eulerian (two-fluid) method to reduce

computational expense compared to a Eulerian-Lagrangian approach. The mathematical method of the Eulerian-Eulerian two-fluid model was applied. Both prototype-scale and commercial-scale models operate at on-design, commercial conditions ($P = 1 \text{ MPa}$, $T = 1,200^\circ\text{C}$). The prototype-scale model matches the geometry of the hot prototype test, whereas the commercial-scale model matches the geometry of a conceptual 300-MW_{th} PFB HX.



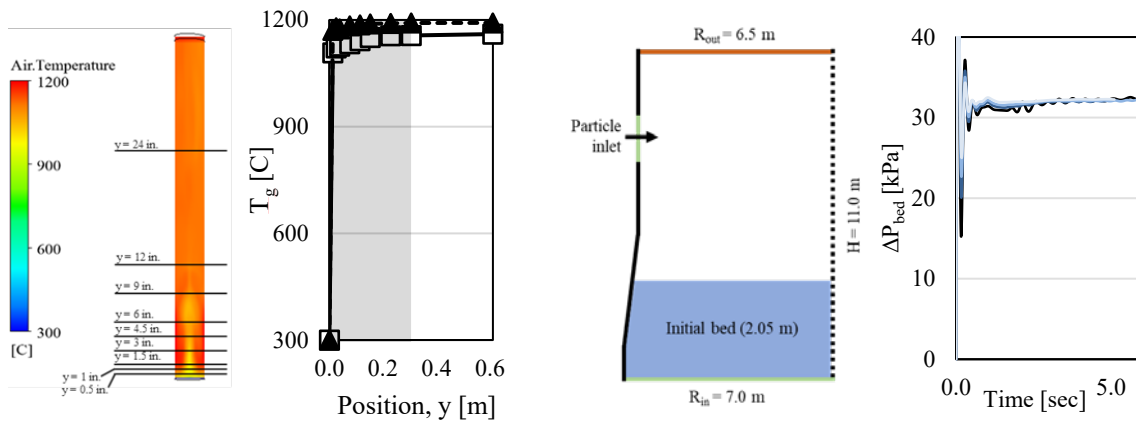
(a) Hot PFB prototype for air/particle heat transfer and fluidization.



(b) Hot prototype test results of air heated by hot particles.

Figure 37. The design of a PFB in batch operation for direct air/particle heat transfer.

Figure 38 shows a sample result from the CFD models of a prototype-scale and a commercial-scale PFB HX. Figure 38(a) shows how effectively the inlet air is heated from an initial temperature (300°C) to the bed temperature ($1,200^\circ\text{C}$). In both cases, the air temperature exceeds $1,180^\circ\text{C}$. The relatively flat temperature profile through the bed region (the shaded grey area) is consistent with the high particle surface area and, correspondingly, the high particle-to-air heat transfer surface area.



(a) Prototype-scale temperature profile.

(b) Commercial-scale transient bed pressure drop.

Figure 38. Sample results from both scales of CFD models of PFB HX.

Figure 38(b) shows the transient air pressure drop across the bed at startup conditions for the commercial-scale PFB HX. Initial transient spikes in the bed pressure drop dissipate in less than 5 seconds and stabilize in normal PFB HX bed operation. Any additional fluctuations are minor and are associated with small bubbles that continue to rise through the bed. The steady-state bed pressure drop is approximately 34 kPa (or less than 4% of the turbine inlet pressure). Some additional pressure drop is expected to occur across the air distributor, cyclone separator array, and piping.

The heated exit air from the PFB HX then flows through an array of air/particle separation cyclones inside the pressure vessel to remove the entrained particles from the airstream. Air/particle cyclones are devices that are proven to clean particles from an air stream and can be very effective in removing fine particles from air flow using well-established design practices [40]. Cyclones have successfully been used in fluidized bed boilers in connection with gas turbines [41]. The cyclone design in this PFB HX used the design method in [40] and achieved a particle separation cutoff size of $<10\ \mu\text{m}$ in particle diameter at a 2.8 kPa pressure drop, meeting the turbine and system performance requirements specified for ABCC integration.

Preliminary results from the commercial-scale PFB HX model indicate that the commercial-scale PFB HX will have the same high heat transfer effectiveness as the prototype-scale PFB HX. These CFD models were validated using prototype testing results and will serve as design tools to examine on- and off-design performance, future design decisions (e.g., distributor design, internal baffling), ramp rates, and performance at different operating conditions of a commercial-scale PFB HX for particle TES applications.

2.5 Task 5. Full-Scale System Modeling

(Note: Work contributed by Jeffrey Gifford, NREL.)

Modelon Impact, a Modelica-based system modeling software, was used to develop a full-scale model of the ENDURING system. Modelica is an equations-based, multi-physics, acausal, object-based modeling language. The language enables the construction of a library of reusable component models that can be connected in a system model. Each component model contains its own set of governing equations (e.g., mass balance, energy balance, momentum balance) and parameters. These models are transient by default. The code is compiled to generate a system of equations before those equations are solved. Figure 39 presents the final form of the ENDURING system model.

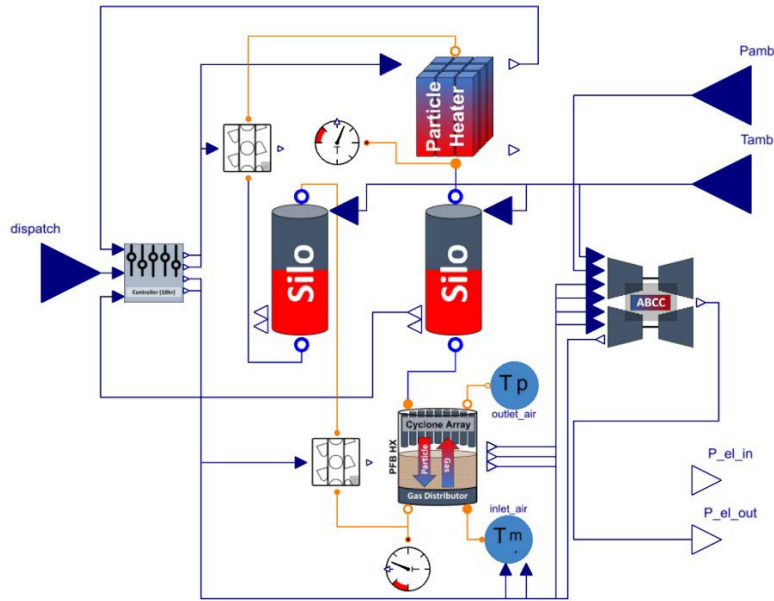


Figure 39. Integrated system model for a 10-hour ENDURING system with inputs for dispatch signal, ambient temperatures, and ambient pressure.

The key inputs are the time series of the dispatch signal, ambient temperature, and ambient pressure. The system model consists of reduced-order models (ROMs) for various components that are described and validated below. A library of key components of the ENDURING system was built and validated by work performed in other tasks in the ENDURING project.

2.5.1 Component Model Development and Validation

The key component models developed were: (1) the particle electric heater, (2) the particle storage silo, (3) the PFB HX, and (4) the ABCC power cycle. Table 19 presents a brief description of each model with their component module in Modelon.

Table 19. Summary of Component Model Development

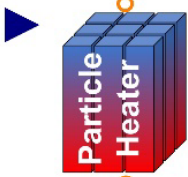
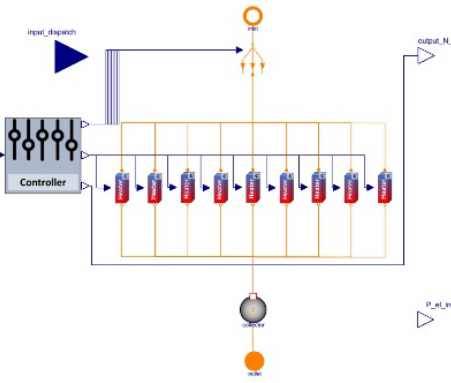
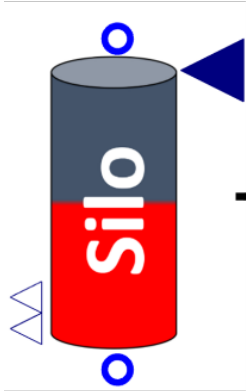
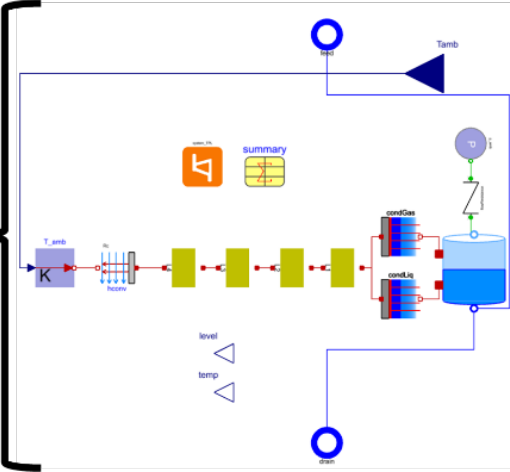
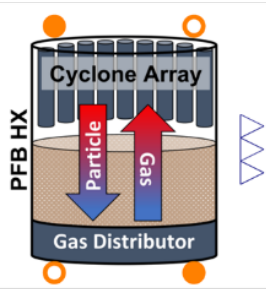
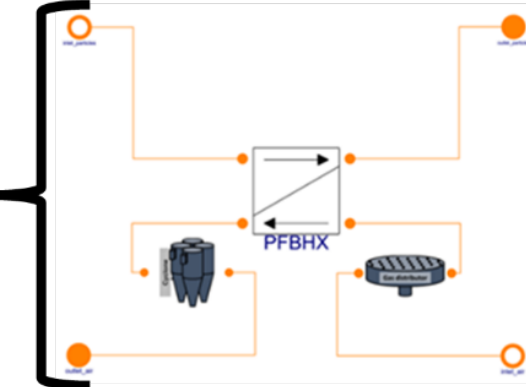
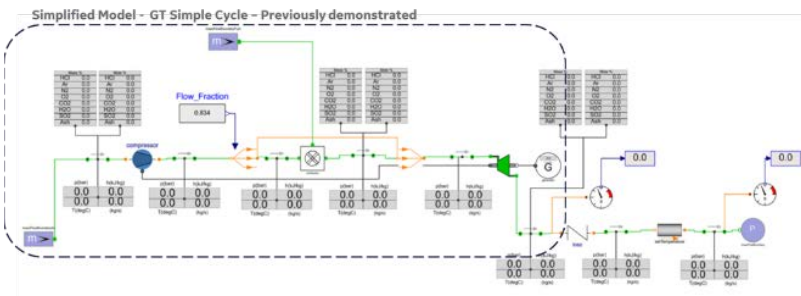
Component	Component Model	Brief Description
<p>Electric Particle Heater</p> 		<p>A transient, 1D discretized heater model with a controlled wall temperature by the heater design, and power supplied from any electric source.</p>
<p>Particle Storage Silo</p> 		<p>A tank model connected to an insulation network, where each insulation layer has its own thermal mass. Convection to the ambient is included the ambient temperature signal.</p>
<p>PFB HX</p> 		<p>A counterflow heat exchanger using the effectiveness number of transfer units (NTU) algorithm, where conductance, UA was calibrated by the CFD results. Pressure drop correlations across the bed, gas distributor, and cyclone array are included.</p>
<p>ABCC Power Cycle</p>		<p>A GE-developed power cycle model with an integrated PFB HX component. The gas cycle was explicitly modeled; the bottom cycle was modeled using second law analysis.</p>

Figure 40 shows the testing and modeling that were used to validate the three most novel components (electric particle heater, particle storage silo, and PFB HX). The model development on key components were started from physical models including both heat/mass balanced calculation and high-fidelity of the physical processes, and also described in reduced-order models in the Modelon-Modelica modeling tool. The model descriptions and validation procedures are detailed in this section, as the model can simulate an ENDURING energy storage system for design and operation.

The three components were modeled using reduced-order models (ROMs). The ENDURING project, as described in previous sections of this report, included experimental tests of all three of these components as well as high-fidelity modeling. The high-fidelity models were validated by the experimental tests. However, it is computationally impractical to run entire CFD, FEA, or DEM models in a system-level modeling tool. Therefore, ROMs are necessary. The ROMs were validated by the high-fidelity models using results from commercial-scale simulations. This ensured that the system model reflected the knowledge generated about each of the components during the ENDURING project.

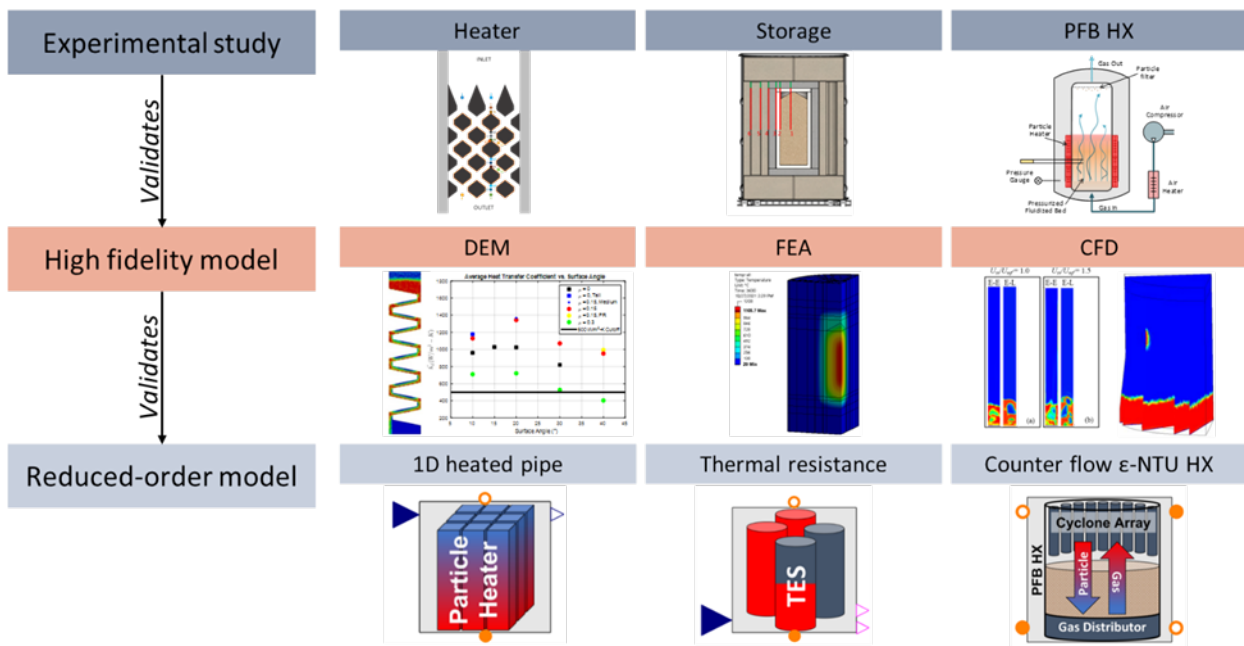


Figure 40. Validation pathways for the three key Modelon-based ROMs.

2.5.1.1 Electric Particle Heater

The particle heater model consists of an array of nine individual, 1D, transient heating channels. The heater array mirrors the design of the proposed commercial-scale particle heater for the ENDURING system. The individual heating channels are henceforth referred to as “heaters” and the collection of heating channels is henceforth referred to as the “heater array.” Each heater is identical in terms of its dimensions and physics. This design enables each individual heater to operate at fixed, on-design conditions, whereas the heater array can load follow at nine discrete levels between fully “off” (zero heaters on) and fully “on” (nine heaters on). The heater array model includes a controller that processes an input dispatch signal and determines the state points of individual components.

Control

The particle heater array has a controller that receives inputs from the upper supervisory controller and outputs signals to each individual heater as well as back to the supervisory controller. Figure 41 shows the heater input/output signals for operational control. The dispatch signal can be any time-varying signal with a range $[-1, 1]$. Signal values of -1 , 0 , and 1 mean that the system is discharging at full load, holding, or charging at full load, respectively. Anything between these values indicates partial load. For any dispatch signal less than or equal to zero, the heater array controller closes the split valve, sends an “off” signal to all heaters, and tells the supervisory controller that zero heaters are on. For any dispatch signal greater than zero, a few calculations occur. First, the controller determines how many heaters can be turned on (an integer value) based on the dispatch signal (a continuous value). For example, if the dispatch signal is 0.500 , then the heater array controller will determine that only four heaters can be turned on. Four heaters use only 0.444 of the total capacity of the heater array (which has nine total heaters in this design), whereas five heaters would use 0.555 of the total capacity, exceeding the value of the dispatch signal (see Figure 42). Figure 42 shows an exemplary result of heater array controller processing dispatch signal.

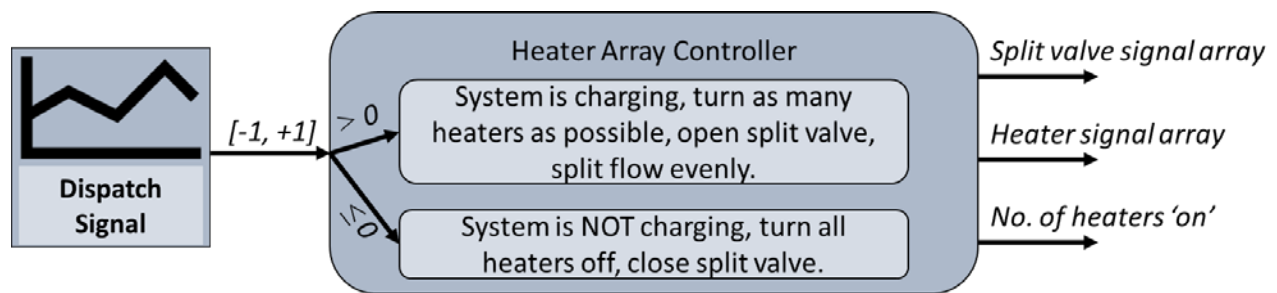


Figure 41. Heater array control logic based on dispatch signal.

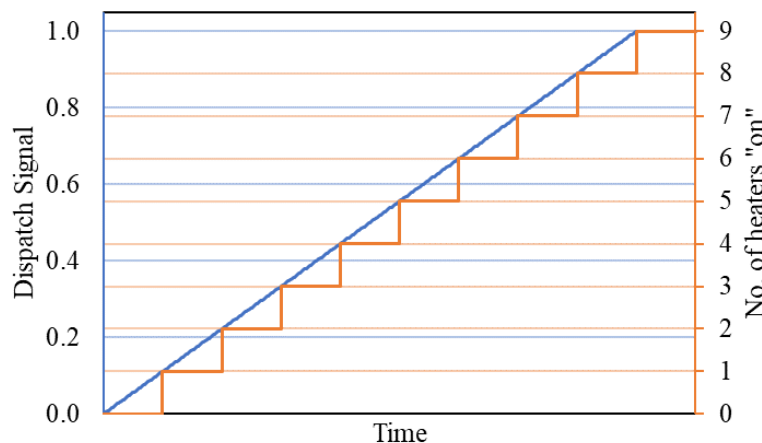


Figure 42. Example result of heater array controller processing dispatch signal.

Thus, the heater array controller will split the flow into four equal streams and send each individual stream to one of the four heaters that is turned on. Additionally, the heater array controller will feed back to a higher system-level controller that only four heaters were turned

on, and thus only four-ninths of the maximum mass flow rate of particles will be sent through the heater array. This ensures that the individual heaters always operate at design conditions, as intended.

Validation

The reduced-order model (ROM) of an individual electric particle heater was validated by the DEM model built in MFIX which used actual particle heater geometries. The DEM model discerned the heat transfer coefficient as a function of heat element surface angle and friction coefficient. The electric particle heater ROM was a transient, one-dimensional heated square pipe model. The heater's wall temperature was defined (within material limits) by a feedback controller based on the outlet particle temperature. The heat transfer coefficient was taken from the results of the DEM model. The heat transfer area term was defined based on a heat transfer area per unit volume that was related to the hexagonal shape of the heating elements. The heat transfer area per unit volume parameter was calibrated based on one set of results from the DEM model, and then the predicted temperature profiles through the particle heater were compared between the two models on another set of DEM results (with the same geometry) to validate the Modelon-based ROM. Therefore, the electric particle heater model is calibrated to the hexagonal electric particle heater design proposed for the commercial-scale ENDURING system. The DEM results ranged from heating element angles of 10° to 30° and surface friction coefficients of 0.0 to 0.3.

The temperature profiles were compared for two surface angles and two friction coefficients (for a total of four cases). The results are shown in Figure 43.

For all four cases examined, the Modelon-based ROM was within 10% of the MFIX results. This validates that the ROM sufficiently predicts the performance of the particle heater. Note that the results shown in Figure 43 do not cover the entire length of the commercial heater; ; therefore, the particles do not reach the design exit temperature of near $1,200^\circ\text{C}$. This was due to the computational limitations of the DEM model. A 1D model was developed and extended the MFIX model to simulate particle heating process in the whole heater.

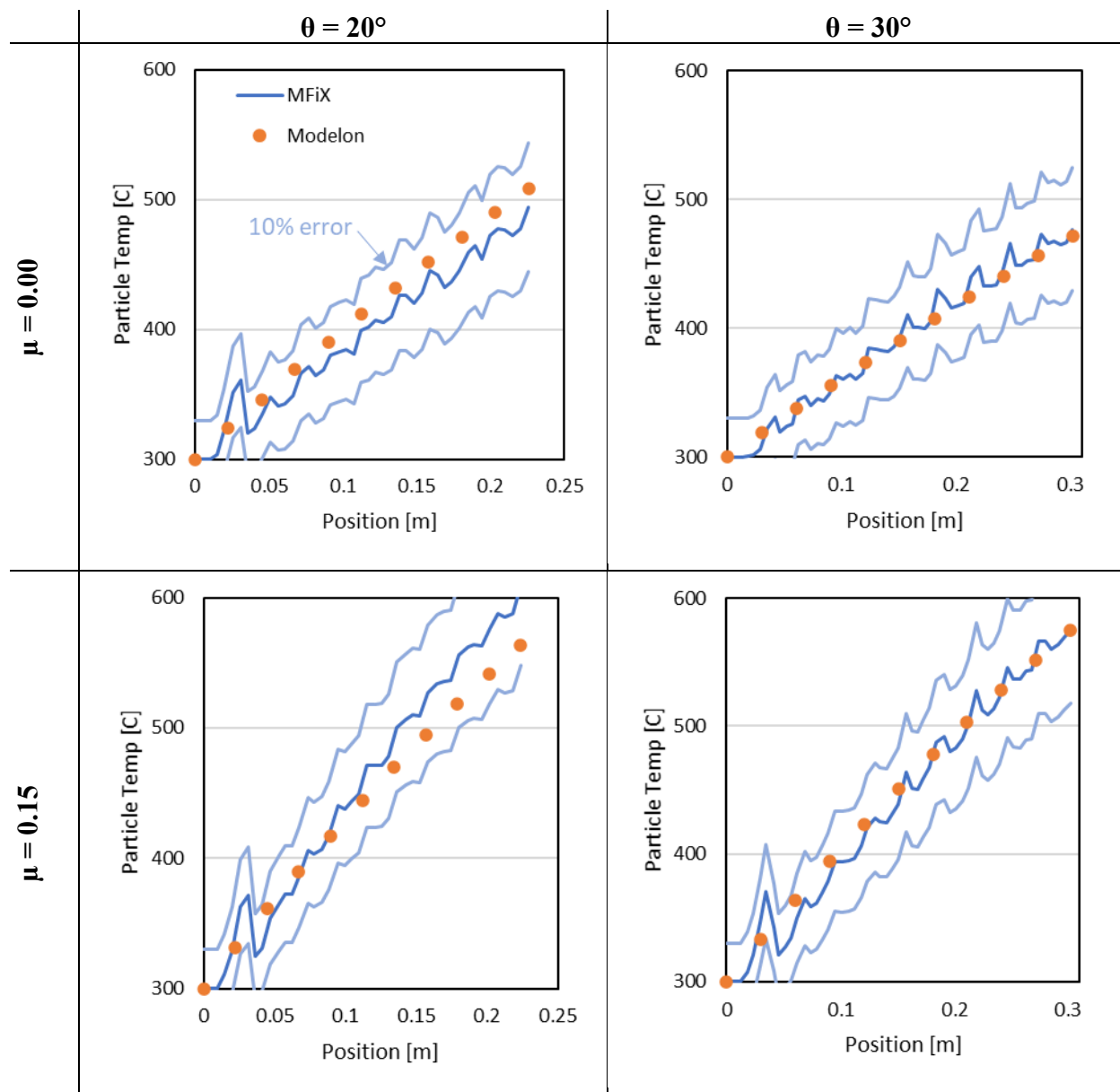


Figure 43. Comparison of 1D temperature profiles predicted by the high-fidelity MFiX and Modelon-based ROM of the electric particle heater at two different surface angles (θ) and friction coefficients (μ).

2.5.1.2 Particle Storage Silo

The particle storage array model is composed of five individual particle storage silos, valves for charging and discharging, a skip hoist, and a storage array-specific controller (see Figure 44). Each individual silo model has the same mathematical description, as described in Table 19. The storage array model also includes connection ports for the particle medium to the other components and three signal connections: (1) the input dispatch signal from the supervisory controller, (2) the output electric power consumed by the skip hoist, and (3) the output Boolean signal that tells the supervisory controller whether the storage is empty, full, nor neither.

storage volume. The top, side, and bottom natural convection heat transfer coefficients were the same for both models (7, 5, and 2 W/m²-K, respectively), in accordance with established natural convection correlations. Both models then simulated seven days of cooling.

The two models were compared based on their prediction of the key metric: the state of charge (SOC) over time. SOC was defined as:

$$SOC(t) = \frac{T_p(t) - 300}{T_p^0 - 300} \quad (1)$$

The results of this validation study are shown in Figure 45; the SOC predicted by the Modelon TES model and the FEA model, as well as ±10% and ±2% error bands (based on the FEA model), are shown. The Modelon TES model is within 2% of the FEA model over the entire seven-day simulation.

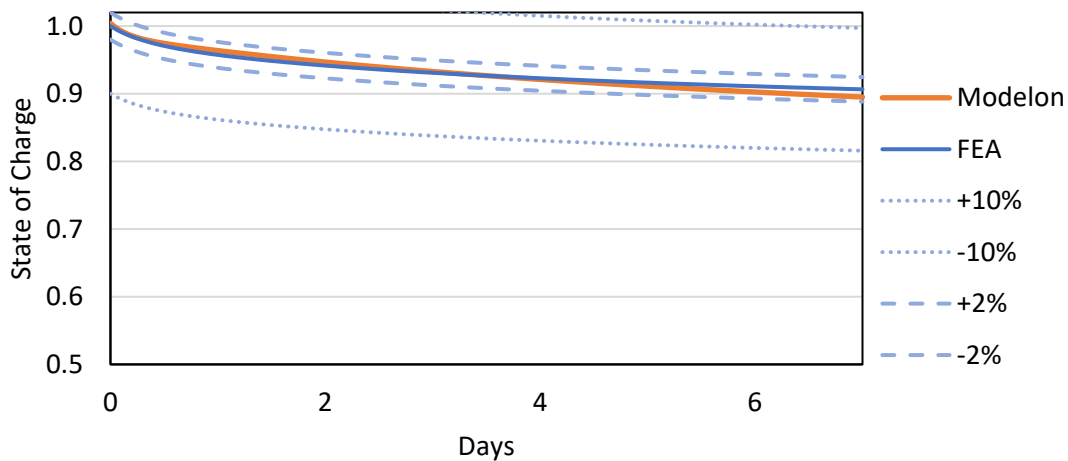


Figure 45. SOC of the particle storage silo over a seven-day cooling process.

It is important to note that the SOC results shown in Figure 45 are not representative of the particle storage efficiency during normal operation. During normal operation, the insulation materials have a higher initial temperature (e.g., the first refractory layer will not be starting at 20°C every time the storage silo charges; instead, it will heat up over several operating cycles). However, this study still validates the Modelon-based ROM of the particle storage silo by showing that the thermal performance predicted by the ROM and the high-fidelity FEA model are less than 2% apart.

2.5.1.3 PFB HX model

The PFB HX is modeled as a counterflow heat exchanger. Heated particles enter from the hot storage silo and exit to a skip hoist, which brings the cooled particles to the top of the cold storage silo. Ambient air ($P = 1$ atm, $T = 293$ K) is compressed to near 10 bar and 573 K prior to entering the PFB HX. The specific inlet pressure and temperature are determined by the compressor in the power cycle model. The PFB HX heats the air to near the particle inlet temperature due to the effective counterflow design. The heated, compressed gas exits the PFB HX, goes through a cyclone separator array, and then is sent back to the power cycle.

The heat transfer is modeled using a steady-state effectiveness NTU algorithm, a ubiquitous correlation for counterflow heat exchangers. The UA parameter in the algorithm was calibrated against the results of the commercial-scale CFD model and was assumed to be constant for all gas inlet velocities; future work could focus on more closely calibrating the relationship between the UA and the approach temperatures of both phases, as well as incorporating more CFD simulations (e.g., over a range of conditions) and experimental results.

The other key aspect of the model is the gas-phase pressure drop. The gas-phase pressure drop through the heat exchanger is comprised of four parts: (1) the bed, (2) the gas distributor, (3) the cyclone array, and (4) minor losses.

The bed pressure drop is calculated using the Ergun equation for minimum fluidization velocity and the prescribed bed dimensions (height and diameter). The bed pressure drop is equal to the hydrostatic pressure of the bed if the gas velocity through the heat exchanger is above minimum fluidization velocity at the inlet conditions. If the gas velocity is below this value, there is a linear relationship between bed pressure drop and gas velocity from zero up to the point of minimum fluidization velocity.

The gas distributor pressure drop is modeled using a simple friction factor, with pressure drop having a quadratic relationship with gas velocity. The cyclone array uses industry-based correlations to calculate a net friction factor based on the physical dimensions. The array assumes that the gas flows uniformly through each cyclone. The minor losses are computed as a percentage of the bed pressure drop based on detailed design calculations.

Validation

The ROM PFB HX model was validated for two key metrics: (1) bed pressure drop and (2) heat exchanger effectiveness. These two metrics were chosen because they are the two most important metrics that impact overall system performance. Figure 46 shows the results of this comparison for both metrics over a range of inlet velocities. The Modelon-based ROM model is well within 10% of the high-fidelity CFD model for all inlet velocities tested.

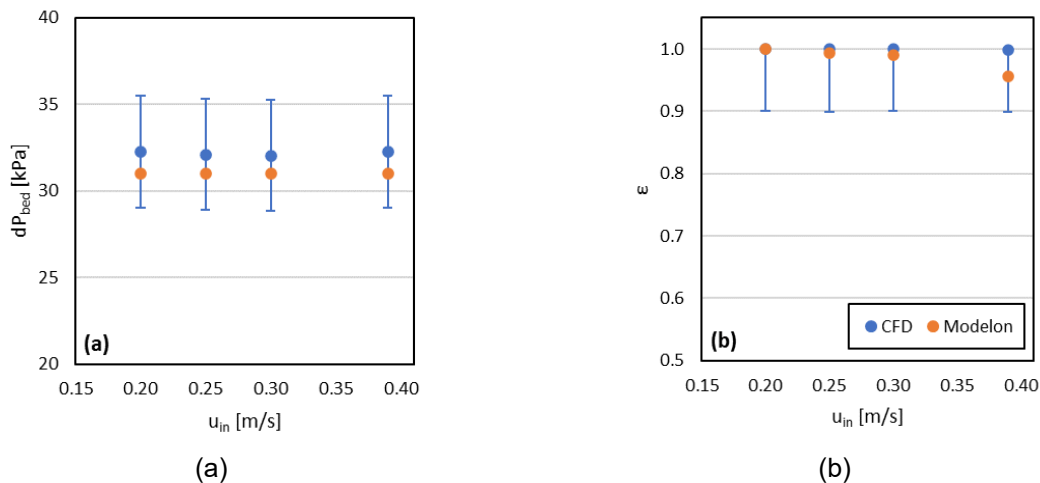


Figure 46. Comparison of the (a) gas-phase bed pressure drop and (b) effectiveness predicted by high-fidelity CFD and Modelon-based ROM models of the PFB HX with 10% error bars.

The Modelon-based ROM PFB HX model was validated using the results from the commercial-scale CFD model built during the ENDURING project. The commercial-scale CFD model of the PFB HX used the Eulerian-Eulerian methodology that was validated in Milestone 1.7.

2.5.1.4 Power Cycle Model

(Note: Work contributed by General Electric Global Research Center’s Dr. James Tallman and Dr. Naveenan Thiagarajan.)

GE Research developed a power cycle model in Modelon Impact. The gas cycle portion of the model used the GE 7E.03 as a reference and validated it against their internal models in HYSYS software. The gas cycle was connected to a bottoming cycle model to predict combined cycle performance. Additionally, the gas cycle was modified to include the PFB HX model, which acted as an additional or replacement heat source to the combustor.

Figure 47 shows the combined cycle model developed in Modelon. The model used a simple turbine cycle model with a parametric steam-Rankine cycle to represent the combined cycle that was validated with the HYSYS modeling results. The power system model was then coupled with PFB HX and particle TES to simulate integrated system performance.

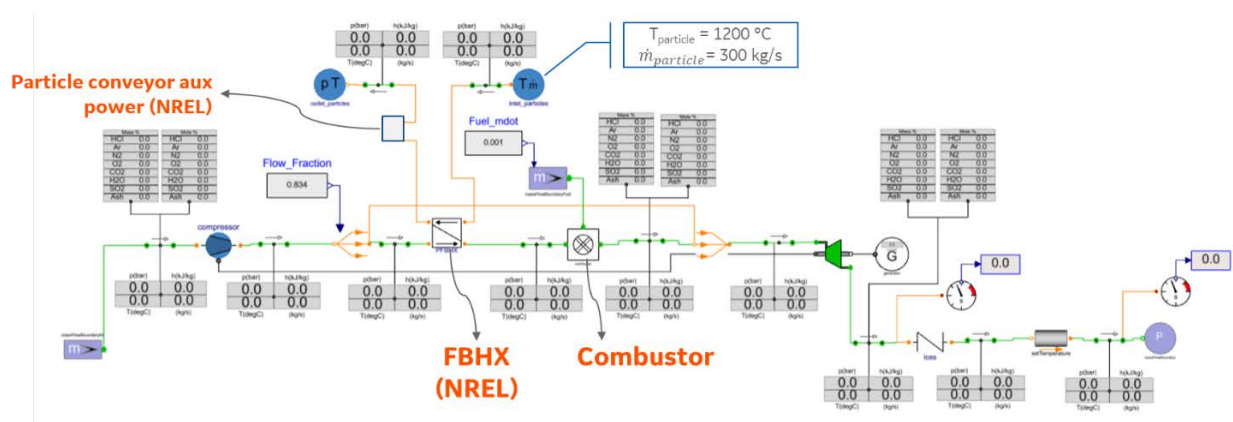


Figure 47. Simplified combined cycle gas turbine model for 7E.03 developed in Modelon Impact.

Note that in the combined cycle (CC) model, the bottoming cycle (BC) is not explicitly modeled with all the physical components of the cycle. Instead, a lumped model analysis is utilized to calculate the exergetic efficiency and the BC power generation. The calculation used outputs from the simple cycle, such as the exhaust temperature, flow conditions at the exhaust and reference states, and mass flow rate, among operation parameters. The extended section of the model shown in Figure 47 is specifically aimed at fluid property estimation at the reference state. The motivation for this simplification is to avoid the complexity involved in modeling all the physical components of the coupling or input parameters while achieving performance estimates that agree well with the 7E.03 performance estimates available in the literature.

Table 20 summarizes the performance estimates of the simplified CC model shown in Figure 47. Note that the simplified CC model developed in Modelon is within 2% of the HYSYS model. In the estimates shown in Table 20, the main source of error in the Modelon and HYSYS models is the estimated generator power in Modelon. This arises due to differences in modeled generator

losses. The generator losses will be updated to match the HYSYS model and that of published data in a future revised version.

Table 20. Combined Cycle Performance Estimates Comparison: Modelon vs. HYSYS

Parameter	Modelon	HYSYS	Delta [%]
Generator Power [MW]	91.6	90.2	1.6
Combustor Power [MW]	266.8	266.0	0.3
Simple Cycle Efficiency [%]	34.3	33.9	1.3
BC Exergetic Efficiency [%]	73.1	72.9	0.3
BC Gross Power [MW]	53.2	53.1	0.2
BC Auxiliary Power [MW]	2.6	2.6	0.0
Net Power* [MW]	141.6	140.2	1.0
Net Efficiency [%]	53.2	52.7	0.9

Figure 48 compares key performance estimates between the simplified 7E.03 CC model and the modified CC model with PFB HX. The net power produced by the modified CC with PFB HX is 18.1% lower than the baseline, which is mainly due to the lower heat input from the PFB HX (14.2%) relative to the combustor. The lower PFB HX capacity is potentially due to the assumed air flow rate in 7E.03 GTCC used to size the PFB HX and the selection of silica sand boundary conditions, which may not have included the required cooling air extracted from the compressor into the turbine.

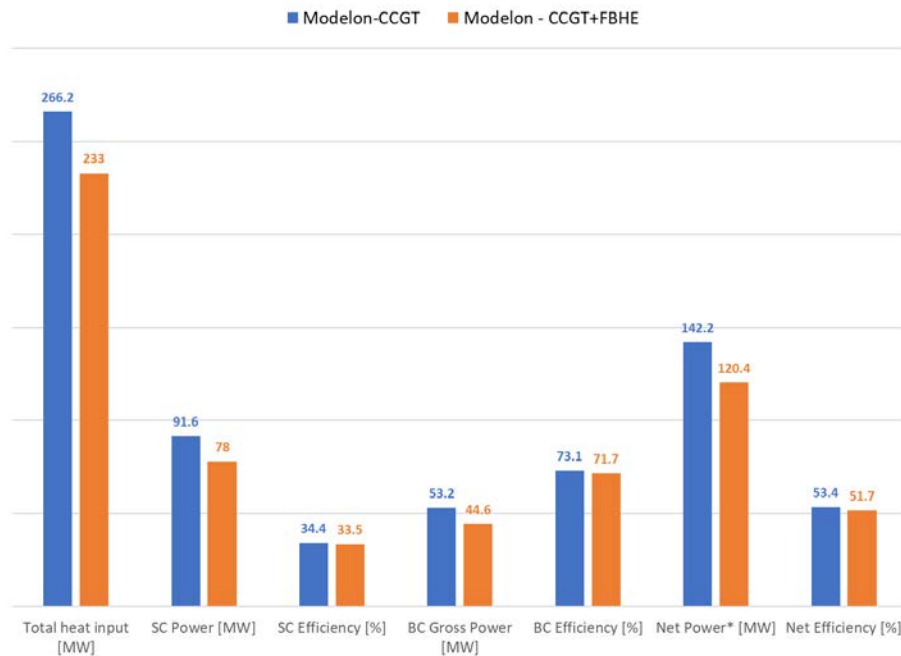


Figure 48. Comparison of performance of baseline 7E.03 CC model vs. modified CC with PFB HX
BC efficiency refers to second law exergetic efficiency.

Without altering the 7E.03 air flow rate in the modified CC model to improve the net power, other key parameters that could impact the PFB HX duty are particle storage temperature (assumed to be the same as the PFB HX inlet) and particle mass flow rate. The modified CC model was used to study the effect of these two parameters on net power, and the results are shown in Figure 49.

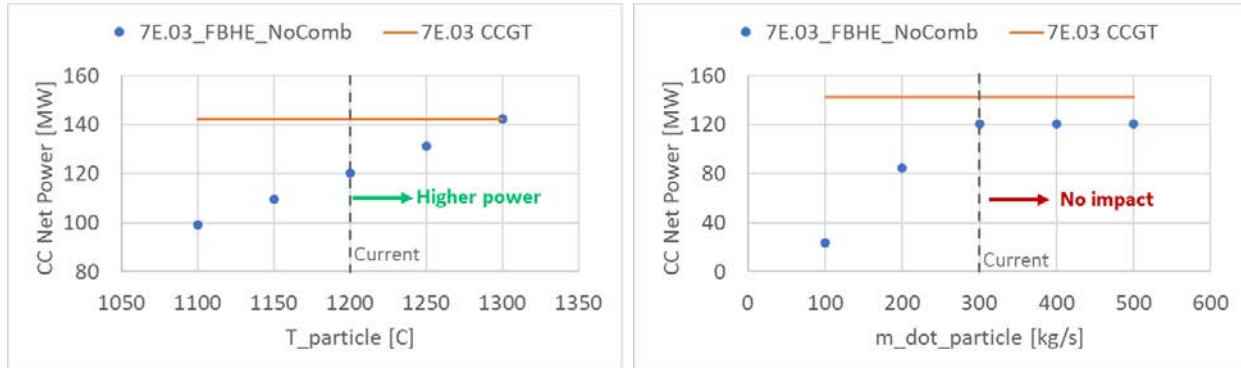


Figure 49. Effect of particle temperature and mass flow rate on net power produced in the modified CC cycle with PFB HX.

As shown in Figure 49, a 100°C increase in the particle storage (or PFB HX inlet) temperature increases the net power produced to the same value as the baseline. Conversely, the power produced can be reduced if the designed particle temperature is lowered. Any increase in particle temperature to improve the net power may also increase insulation requirements and hence capital costs associated with the storage system or any design changes required in the PFB HX.

Figure 49 also shows that increasing the mass flow rate beyond the current value of 300 kg/s at a fixed particle temperature of 1,200°C does not impact the net power, as the heat exchanger effectiveness is already high (>98%). However, decreasing the mass flow rate significantly impacts the net power produced.

For steady-state system performance modeling of the gas turbine unit within a GTCC + TES system, the GTCC thermodynamic performance (output, efficiency, etc.) should be close to that of a fuel-fed combustion system. This assumes that the TES heat exchanger adds the same net heat into the same GT flow rate and has the same pressure drop as that of the baseline combustor. Flow rates and heat transfer by the HX are expected to be controllable via operational settings of a properly designed HX device. However, the pressure drop across the HX device is expected to deviate from that of the baseline fuel combustor, and the performance response of the GTCC associated with a change in that pressure drop is necessary for assessing the GTCC + TES system performance. Hence, we have created GTCC performance response curves as function of the pressure drop across the HX device. These performance response curves may be substituted into the Modelon model in place of the GTCC simulation blocks for convenience of TES and HX innovation communities like those partnering on this ENDURING project.

As the HX pressure drop increases, an increase in shaft work between the turbine and compressor will be required to maintain the same flow rate through the device. In this model, it is assumed that that any increase in the HX pressure drop will be compensated for by a

corresponding increase in the compressor pressure ratio, such that the fluid pressure at the inlet of the turbine will remain the same (though the turbine inlet temperature will change). Normally, an operational change to the compressor pressure ratio (for a fixed rotational speed) would also result in a change in the compressor flow rate. For this study, a “rubber compressor” is assumed, meaning that for each change in pressure ratio, the compressor geometry is assumed to scale in size such that the new geometry produces the same flow rate at the updated pressure ratio and the original rotational speed. In simulating the impact of a combustor pressure drop, the inlet mass flow rate of air (286.1 kg/s) in the compressor and inlet pressure in the turbine are maintained to be the same as the baseline.

Figure 50(a) shows the simulated impact of a combustor (or heat exchanger) pressure drop on cycle power and efficiency. As the pressure drop increases from the baseline (0.43 bar), the compressor pressure ratio also increases, which leads to higher compressor work, thereby reducing the simple cycle and combined cycle power. However, the higher compressor pressure ratio also results in higher temperatures at the turbine inlet (Figure 50(b)), with combustor properties remaining the same, leading to a higher power produced in the bottoming cycle. Thus, the combined cycle power, which is the sum power of net simple cycle and bottoming cycle, does not decrease at the same rate as the simple cycle power (see the different slope values in Figure 50(a)). Note that a higher turbine inlet temperature at higher combustor (or heat exchanger) pressure drops would also require an elevated particle temperature, leading to higher charging energy requirements in a thermal energy storage application.

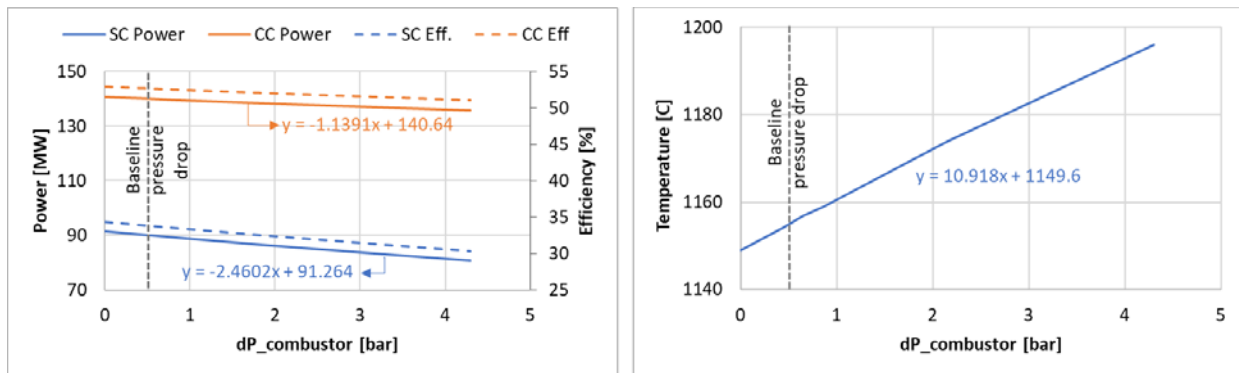


Figure 50. Effect of combustor (or heat exchanger in storage operation) pressure drop on (a) simple and combined cycle power and efficiency and (b) turbine inlet temperature.

The relationship between combustor (or heat exchanger, etc.) pressure drop and power produced can be used in system models including heat exchangers and energy storage devices that are integrated with a 7E.03 combined cycle model, without modeling the cycle explicitly. To save computational expense, a turbomachinery performance map was incorporated in the turbine-compressor model. The performance map component is shown in Figure 51.

The model is designed to accept several inputs to create flexibility with different performance maps. In this case, the pressure drop across the PFB HX, the heat duty of the PFB HX, and the ambient conditions for the compressor inlet are some of the inputs. Using the data provided by GE, the model converts the thermal power added to the gas flow to electric power out of the system.

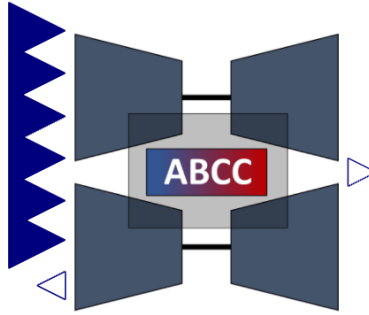


Figure 51. Performance map component of the power cycle, built in Modelon Impact.

2.5.2 System Modeling and Results

The system model's main result is the round-trip efficiency (RTE) of the ENDURING system, based on design parameters and a given operating schedule (i.e., dispatch signal). The dispatch signal can be a simple diurnal signal or grid demand projection. The system RTE is defined as:

$$RTE = \frac{\int_0^t P_{out}^e dt}{\int_0^t P_{in}^e dt}$$

This model tracks the RTE over time as a cumulative integration of the total electricity produced over the total electricity consumed. The model is always initialized as empty in these simulations. The first result, presented in Figure 52, demonstrates the impact of simulation time on the predicted RTE. The RTE evolves over the length of the simulation, with different RTEs predicted depending on the simulation time.

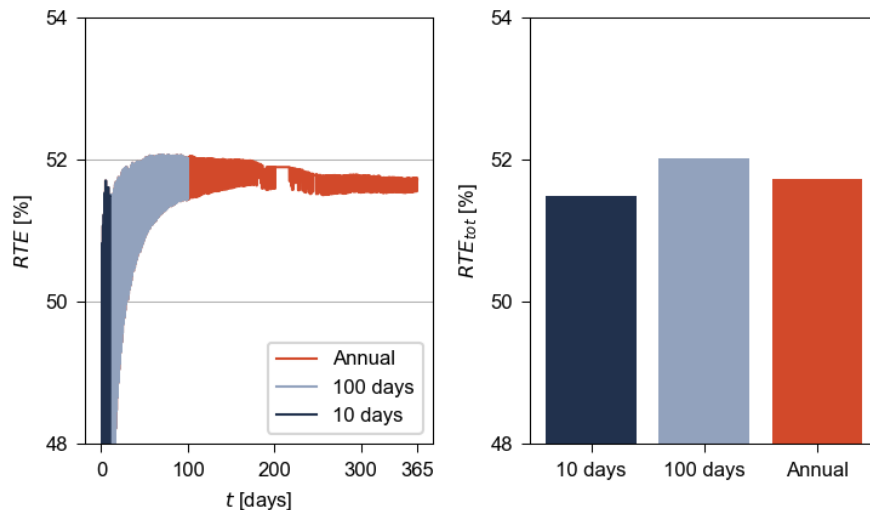


Figure 52. The impact of simulation time on predicted RTE. Dispatch signal for this simulation contained a pause in the operation of the storage system during the summer due to grid price signals, therefore, the RTE is constant in this region until operation is resumed.

The RTE improves over the first 100 days as the thermal mass of the insulation layer increases, and then it decreases slightly as higher ambient temperatures lower the heat duty of the PFB HX and the power cycle efficiency. This result shows the importance of the transient model, as the performance of TES systems can vary depending on transient assumptions, and the importance of being able to simulate annual operations to get a more holistic understanding of performance.

The system model can evaluate the impact of design parameters, such as insulation thickness, on performance and how those changes depend on operating schedules, as shown in Figure 53. The nominal RTE can improve with thicker insulation, as expected, but the model quantifies the level of improvement and how it varies depending on operation. In Figure 53, the curves represent the lengths of time between full charge and discharge cycles, which are different than the dispatch signal evaluated in Figure 52. These performance improvements come at the expense of higher capital costs for the additional insulation material. Design optimization with TEA could quantify this trade-off in terms of an economic metric such as LCOS. The system model developed here is a detailed performance analysis tool, but design optimization and TEA can be added in Modelon Impact or by wrapping the Modelon-based model in Python or another modeling language through Modelon functional mock-up units (FMUs).

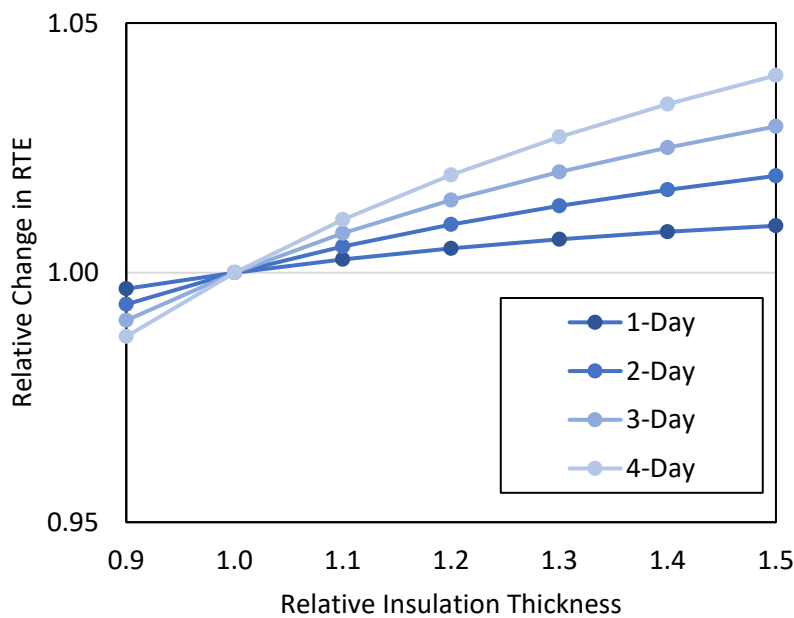


Figure 53. The relative change in RTE to base case (relative insulation thickness equal to 1) for different relative insulation thicknesses for different assumed operating schedules (i.e., days between charge and discharge cycles).

References

- [1] Almendros-Ibáñez, J. A., Fernández-Torrijos, M., Díaz-Heras, M., Belmonte, J. F., and Sobrino, C., 2018, “A Review of Solar Thermal Energy Storage in Beds of Particles: Packed and Fluidized Beds,” *Sol. Energy*, (January), pp. 0–1.
- [2] Davenport, P., Ma, Z., Nation, W., Schirck, J., and Lambert, M., 2020, “Thermal Stability of Silica for Application in Thermal Energy Storage, 26th International SolarPACES Conference, September 28 - October 2, 2020.”
- [3] Covia, 2021, “Technical Data Sheet, Granusil Mineral Filler, Wedron, IL,” pp. 1–2.
- [4] Gifford, J., Ma, Z., and Davenport, P., 2020, “Thermal Analysis of Insulation Design for a Thermal Energy Storage Silo Containment for Long-Duration Electricity Storage,” *Front. Energy Res.*, **8**(June), pp. 1–12.
- [5] PFBC Environmental Energy Technology Inc., 2018, “How a PFBC System Works” [Online]. Available: <http://www.pfbceet.com/our-technology/how-a-pfbc-system-works/>.
- [6] Vandervort, C., Leach, D., and Scholz, M., 2016, “Advancements in H Class Gas Turbines for Combined Cycle Power Plants for High Efficiency, Enhanced Operational Capability, and Broad Fuel Flexibility,” *The Future of Gas Turbine Technology 8th International Gas Turbine Conference*, pp. 1–9.
- [7] Newsom, G., 2019, “Estimated Cost of New Utility-Scale Generation in California: 2018 Update California Energy Commission,” (May).
- [8] Gerdes, K., Summers, W. M., and Wimer, J., 2011, “Cost Estimation Methodology for NETL Assessments of Power Plant Performance DOE/NETL-2011/1455,” (March 2010), p. 26.
- [9] Ma, Z., Davenport, P., and Zhang, R., 2020, “Design Analysis of a Particle-Based Thermal Energy Storage System for Concentrating Solar Power or Grid Energy Storage,” *J. Energy Storage*, **29**(June), p. 101382.
- [10] Repole, K. K., 2019, “The Development and Application of Design and Optimization Methods for Energy Intensive Mechanical Systems for Challenging Environments as Applied to a Concentrated Solar Power Particle Lift System.”
- [11] Towler, G., and Sinnott, R., 2012, *Chemical Engineering Design: Principles, Practice and Economics of Plant and Process Design*, Elsevier.
- [12] Feng, Z., Wang, J. J.-A., and Zhang, W., 2011, “Vessel Design and Fabrication Technology for Stationary High-Pressure Hydrogen Storage.” Presentation to 2011 DOE Hydrogen and Fuel Cells Program Review.
- [13] Moskowitz, S., Cole, R., and Defeo, A., 1977, *Engineer, Design, Construct, Test and Evaluate a Pressurized Fluidized Bed Pilot Plant Using High Sulfur Coal for Production of Electric Power. Phase I. Preliminary Engineering. Topical Report, 1 March 1976-1 June 1977*, Curtiss-Wright Corp., Wood-Ridge, NJ (USA). Power Systems Div.

- [14] ASME Boiler and Pressure Vessel Code, 2010, “Section VIII Division 1,” Rules Constr. Press. Vessel. Append., **1**, p. 1.
- [15] Schaefer, R., 1979, *Cost Estimate of Fluidized Bed Combustor Air Heater for Gas Turbines. Final Report*, Curtiss-Wright Corp., Wood-Ridge, NJ (USA).
- [16] Tribe, M. A., and Alpine, R. L. W., 1986, “Scale Economies and the ‘0.6 Rule,’” Eng. Costs Prod. Econ., **10**(4), pp. 271–278.
- [17] IndustrialMartUSA, “Gate Valve Cost.”
- [18] Gas Turbine World (2019), “2019 GTW Handbook.”, Volume 34, A Pequot Publication.
- [19] NETL, D. O. E., 2010, “Cost and Performance Baseline for Fossil Energy Plants Volume 1: Bituminous Coal and Natural Gas to Electricity Rev. 2,” Pittsburgh, PA, US.
- [20] Haslback, J., Kuehn, N., Lewis, E., Pinkerton, L. L., Simpson, J., Turner, M. J., Varghese, E., and Woods, M., 2013, *Cost and Performance Baseline for Fossil Energy Plants, Volume 1: Bituminous Coal and Natural Gas to Electricity, Revision 2a*, National Energy Technology Laboratory (NETL), Pittsburgh, PA, Morgantown, WV
- [21] Zoelle, A., Keairns, D., Pinkerton, L. L., Turner, M. J., Woods, M., Kuehn, N., Shah, V., and Chou, V., 2015, *Cost and Performance Baseline for Fossil Energy Plants Volume 1a: Bituminous Coal (PC) and Natural Gas to Electricity Revision 3*, NETL.
- [22] Fout, T., Shultz, T., Woods, M., Turner, M. J., Zoelle, A. J., and James III, R. E., 2018, *Cost and Performance Baseline for Fossil Energy Plants, Volume 1: Bituminous Coal and Natural Gas to Electricity, Revision 4*, NETL.
- [23] Newell, S. A., Hagerty, J. M., Spees, K., Pfeifenberger, J. P., Liao, Q., Ungate, C. D., and Wroble, J., 2014, “Cost of New Entry Estimates for Combustion Turbine and Combined Cycle Plants in PJM,” Cambridge Brattle Gr.
- [24] Silla, H., 2003, *Chemical Process Engineering: Design and Economics*, CRC Press.
- [25] Advanced Research Projects Agency – Energy, 2018, *Funding Opportunity Announcement Advanced Research Projects Agency – Energy (ARPA-E) DURATION ADDITION TO ELECTRICITY STORAGE (DAYS)*.
- [26] McTigue, J. D., Farres-Antunez, P., Markides, C. N., and White, A. J., 2021, “Integration of Heat Pumps with Solar Thermal Systems for Energy Storage,” *Encyclopedia of Energy Storage*, Elsevier.
- [27] Laughlin, R. B., 2017, “Pumped Thermal Grid Storage with Heat Exchange,” J. Renew. Sustain. Energy, **9**(4), pp. 044103–1.
- [28] Mctigue, J. D., and Ma, Z., 2022, “Pumped Thermal Energy Storage with Particle Silos and Fluidized Bed Heat Exchangers,” *SolarPACES 2022*, Albuquerque, NM.
- [29] Ma, Z., Wang, X., Davenport, P., Gifford, J., and Martinek, J., 2022, “Preliminary Component Design and Cost Estimation of a Novel Electric-Thermal Energy Storage System Using Solid Particles,” J. Sol. Energy Eng., **144**(June), pp. 031001-1–12.

- [30] U.S. Department of Energy National Energy Technology Laboratory, 2001, *Tidd PFBC Demonstration Project A DOE Assessment*.
- [31] Ma, Z., Gifford, J., Davenport, P., Jia, D., Schirck, J., and Morris, A., 2021, “Electric Charging Particle Heater for Electric Energy Storage, U.S. Patent Application Number 17/375,105.”
- [32] Garg, R., Li, T., Pannala, S., and Galvin, J., 2012, *Documentation of Open-Source MFI-X-DEM Software for Gas-Solids Flows*, National Energy Technology Laboratory, Morgantown, West Virginia.
- [33] Benyahia, S., Syamlal, M., and O’Brien, T. J., 2012, *Summary of MFI-X Equations 2012-1*, National Energy Technology Laboratory, Morgantown, West Virginia.
- [34] Syamlal, M., Rogers, W., and O’Brien, T. J., 1993, *MFI-X Documentation Theory Guide Technical Note (DE94000087)*, National Energy Technology Laboratory, Morgantown, West Virginia.
- [35] Ma, Z., Wang, X., Davenport, P., Gifford, J., Cook, K., Martinek, J., Schirck, J., Morris, A., Lambert, M., and Zhang, R., 2022, “System and Component Development for Long-Duration Energy Storage Using Particle Thermal Energy Storage,” *Appl. Therm. Eng.*, **216**, p. 119078.
- [36] Schirck, J., Ma, Z., and Morris, A., 2021, “Simulations of Heat Transfer to Flowing Particles Used for Long Duration Thermal Energy Storage,” *Submitt. to J. Appl. Therm. Eng.*
- [37] Ma, Z., 2017, “Design of Particle-Based Thermal Energy Storage for a Concentrating Solar Power System,” *ASME Power and Energy*, Charlotte, NC, pp. 1–8.
- [38] Ma, Z., Wang, X., Davenport, P., Gifford, J., and Martinek, J., 2021, “Economic Analysis of an Electric Thermal Energy Storage System Using Solid Particles for Grid Electricity Storage,” *Proceedings of the ASME 2021 15th International Conference on Energy Sustainability ES2021 June 16-18, 2021, Virtual, Online*, pp. ES2021-61729 1–10.
- [39] Schmidt, O., Melchior, S., Hawkes, A., and Staffell, I., 2019, “Projecting the Future Levelized Cost of Electricity Storage Technologies,” *Joule*, **3**(1), pp. 81–100.
- [40] Yang, W.-C., 2003, *Handbook of Fluidization and Fluid-Particle Systems*, Marcel Dekker, Inc., New York, NY.
- [41] PFBC Environmental Energy Technology Inc., 2018, *PFBC Competitive Clean Coal Power Utilizing Pressurized Fluidized Bed Combined Cycle Technology*.

Project Outputs

Summary of Technology Achievements

- Developed ultrahigh-temperature thermal energy storage (1,200°C) to drive high-efficiency (>53%) power cycle.
 - Demonstrated the thermal stability of storage media and insulation materials.
 - Proved key component designs, including electric charging heater, particle thermal storage containment, discharging heat exchanger, and power cycle integration.
- Low cost, grid-scale ENDURING storage supports renewable integration:
 - Adapting a GE turbine provides an expedited commercialization path to market.
 - The system can achieve large power and storage capacities.
- Particle TES has the potential to achieve **grid-scale energy storage** at a fraction of the cost of conventional chemical battery technologies.
- The ability to provide **base-load power for several days** allows for continued grid integration of intermittent renewable sources.
- Particle TES has siting flexibility and the potential to leverage the infrastructure of coal- and gas-fired power plants for reduced capital cost.

Journal Articles

1. Gifford, J., Wang, X., Wang, J., Ma, Z., and Braun, R., “A System Modeling Platform for Particle-based Thermal Energy Storage Systems for Long-duration Energy Storage Applications,” SolarPACES 2022 Conference. (Accepted).
2. Xingchao Wang, Zhiwen Ma, Patrick Davenport, Korey Cook, Riley Lawson, Jeffrey Gifford, and Jason Schirck, “Gas Distributor Design of a Pressurized Fluidized Bed Heat Exchanger in a Particle Thermal Energy Storage System,” SolarPACES 2022 Conference. (Accepted).
3. Zhiwen Ma, Xingchao Wang, Patrick Davenport, Jeffrey Gifford, Korey Cook, Janna Martinek, Jason Schirck, Aaron Morris, Matthew Lambert, and Ruichong Zhang, “System and Component Development for Long-Duration Energy Storage Using Particle Thermal Energy Storage,” *Journal of Applied Thermal Engineering*, vol. 216, 2022, 10.1016/j.applthermaleng.2022.119078.
4. Ma, Z., Wang, X., Davenport, P., Gifford, J., and Martinek, J., “Preliminary Component Design and Cost Estimation of a Novel Electric-Thermal Energy Storage System Using Solid Particles,” *J. Sol. Energy Eng.* 144, 031001-1–12 (2022).

5. Ma, Z., Davenport, P., and Zhang, R., “Design analysis of a particle-based thermal energy storage system for concentrating solar power or grid energy storage,” *J. Energy Storage* 29, 101382 (2020).
6. Gifford, J., Ma, Z., and Davenport, P., “Thermal Analysis of Insulation Design for a Thermal Energy Storage Silo Containment for Long-Duration Electricity Storage,” *Front. Energy Res.* 8, 1–12 (2020).

Papers (Manuscripts in Preparation)

1. Invited paper to a Joule future energy article: “Electric-Thermal Energy Storage Using Solid Particles.” Invited by Joule editor-in-chief.
2. Submitted a book chapter, “Thermal Energy Storage for Energy Decarbonization,” to *Annual Heat Transfer Review*, edited by Prof. Zhuomin Zhang, Begell House.
3. Gifford, J., Ma, Z., Wang, X., and Braun, R., “A modular particle-based electrical thermal energy storage system modeling library and its application to a long-duration energy storage system for grid electricity.”
4. Gifford, J., Hamilton, W., Martinek, J., Ma, Z., and Braun, R., “Design and dispatch optimization of a particle thermal energy storage system for the retirement of natural gas combined cycles in the United States.”
5. Gifford, J. Ma, Z., Wang, X., and Braun, R., “A computational fluid dynamic analysis of a novel particle-to-air fluidized bed heat exchanger for particle-based thermal energy storage applications.”
6. Schirck, J., Ma, Z., and Morris, A., “Discrete element modeling of a particle heater for energy storage systems,” *Powder Technology*, responding to reviewers (2022).
7. Schirck, J., Ma, Z., and Morris, A., “Temperature stratification and the impact on mixing dynamics and energy transfer in high temperature fluidized beds,” to be submitted to *Energy*, in preparation (2022).

Status Reports (Conference and Workshop Presentations)

1. Ma, Z., “System and Component Development of a Thermal Battery Using Low-Cost Stable Solid Particles,” International Workshop on Carnot Batteries, German Aerospace Center (DLR), September 28, 2022.
2. Ma, Z., Wang, X., Davenport, P., Gifford, J., and Martinek, J., “Economic Analysis of an Electric Thermal Energy Storage System Using Solid Particles for Grid Electricity Storage,” in *Proceedings of the ASME 2021 15th International Conference on Energy Sustainability ES2021 June 16-18, 2021, Virtual, Online ES2021-61729 1–10* (2021).
3. Davenport, P., Ma, Z., Nation, W., Schirck, J., and Lambert, M., “Thermal Stability of Silica for Application in Thermal Energy Storage,” 26th International SolarPACES Conference, September 28 - October 2, 2020.
4. Ma, Z., Davenport, P., and Martinek, J., “Thermal energy storage using solid particles for long-duration energy storage,” in *ASME 2020 14th International Conference on Energy Sustainability, ES 2020 1–9* (2020). doi:10.1115/ES2020-1693.

5. Gifford J., Wang X., Wang, J., Ma Z., and Braun, R., “A System Modeling Platform for Particle-based Thermal Energy Storage Systems for Long-duration Energy Storage Applications,” SolarPACES Conference 2022 (Oral Presentation Accepted).
6. Gifford J., Ma Z., Davenport P., Wang X., and Martinek J., “Design and performance of a novel direct particle-gas fluidized bed heat exchanger for advanced concentrated solar power systems,” SolarPACES Conference 2021 (Oral Presentation).
7. Morris, A., “Using Discrete Element Simulations to Bridge Particle and Continuum Flow Scales,” 2021 Frontiers in Mechanical Engineering and Sciences: Fluid Mechanics, Virtual (Feb 2021).
8. Appaswamy, K., Schirck, J., Ma, Z., and Morris, A., “A numerical and experimental investigation of a high temperature fluidized bed for thermal energy transfer,” to be presented at AIChE 2022 Annual Conference, Phoenix, AZ, United States (2022).
9. Schirck, J., Morris, A., Cook, K., and Ma, Z., “DEM and experimental comparison of particle heat transfer and geometry driven particle flow patterns,” to be presented at AIChE 2022 Annual Conference, Phoenix, AZ, United States (2022).
10. Schirck, J., Appaswamy, K., and Morris, A., “Stratification in a mildly fluidized bed due to thermal inhomogeneities,” World Congress of Particle Technology, Madrid, Spain, Sep. 2022.
11. Schirck, J., Ma, Z., and Morris, A., “An experimental investigation of ultra-high temperature and pressure fluidized bed for thermal energy storage and transfer,” AIChE 2021 Annual Conference, Boston, MA, United States (2021).
12. Schirck, J., Ma, Z., and Morris, A., “Simulations of heat transfer to flowing particles used for long duration thermal energy storage,” AIChE 2020 Virtual Conference, Nov. 2020.

Media Reports

1. <https://www.solarpaces.org/nrel-results-support-cheap-long-duration-energy-storage-in-hot-sand/>
2. <https://www.solarpaces.org/nrel-awarded-2-8-million-to-develop-a-long-duration-thermal-energy-storage-technology/>
3. <https://www.nrel.gov/news/program/2021/nrel-options-a-modular-cost-effective-build-anywhere-particle-thermal-energy-storage-technology.html>
4. <https://www.popsci.com/energy/new-silica-sand-energy-storage/>
5. <https://interestingengineering.com/surprise-hot-sand-can-save-extra-energy-from-wind-and-solar-power>
6. <https://cleantechnica.com/2021/08/31/using-hot-sand-to-store-energy/>

Patent Applications/Issued Patents

1. Zhiwen Ma, Patrick Davenport, Janna Martinek, Particle Thermal Energy Storage System Integrated with Pumped Thermal Energy Storage, USPTO Patent No. 11,181,326 B2. November 23, 2021.
2. Ma, Z., Gifford, J. C., Davenport, P. G., Schirck, J., and Morris, A., 2023, “Electric Charging Particle Heater for Thermal Energy Storage, Issued Patent - U.S. 11,631,992 B2.”

3. Ma, Z., 2022, “Methods and Systems for Thermal Energy Storage and Their Use in Building Applications; US Patent No. 11,480,395 B2.”
4. Ma, Z., Gifford, J. C., Davenport, X. Wang, 2023, “Fluidized-bed heat exchanger for conversion of thermal energy to electricity”, US Patent No. 11,740,025, B2.”

Licensed Technologies

We established an IP option agreement with Babcock & Wilcox Company to commercialize the ENDURING technology for market acceptance.

Awards, Prizes, and Recognition

- First-place of the Best Paper Award in the 2021 ASME Energy Sustainability conference.

Follow-On Funding

Additional funding committed or received from other sources after effective date of ARPA-E Award. Table 21 lists the relevant follow-on funding received to support advanced technology development.

Table 21. Follow-On Funding Received

Source	Funds Committed or Received
DOE Solar Energy Technologies Office (SETO)	\$2M SETO FY22–24 lab call award to develop Pumped Thermal Energy Storage with industry partners B&W and Brayton Energy.
DOE SETO	SETO \$3M (+\$750K cost share) FOA award to develop particle solar receiver.
DOE Office of Technology Transitions (OTT)	\$250K Technology Commercialization Fund award from OTT-SETO of modeling particle TES of the system and components using Modelon tool for industry process heat; industry partners are Alumina Energy and Babcock & Wilcox.
DOE Advanced Manufacturing Office (AMO)	Partnered with ELEMENT 16 Technology Inc. and awarded \$300K High-Performance Computing (HPC) for Energy Innovation (HPC4ei) on sulfur thermal energy storage for industry process heat.
DOE Small Business Innovative Fund (SBIR)	Supported Advanced Materials Scientia on SBIR Phase 1 award for developing low-cost solar particles.
New York Power Authority	New York Power Authority (NYPA) \$75K Phase 1 award to study storage materials and grid service potentials.
DOE Office of Clean Energy Demonstration	\$75K scoping study of the long-duration energy storage on NREL’s Flatirons campus to develop a proposal on scaling up the ENDURING technology. The proposal will lead to a multimillion-dollar demonstration of the ENDURING key components and system integration in a real-operation condition for technology to market.